Technical University of Denmark

DTU

Studies on the Bombardment of Condensed Molecular Gases at Liquid-He Temperatures by keV Electrons and Light Ions

Noauthor, Risø

Publication date:
1982

Document Version
Publisher's PDF, also known as Version of record

Link back to DTU Orbit

DTU Library
Technical Information Center of Denmark

Studies on the Bombardment of condensed Molecular Gases at Liquid-He Temperatures by keV Electrons and Light Ions

Peter Børgesen

RISØ-R-457

STUDIES ON THE BOMBARDMENT OF CONDENSED MOLECULAR GASES AT
LIQUID-He TEMPERATURES BY keV ELECTRONS AND LIGHT IONS

Peter Børgesen

Abstract. Films of solid H_2, D_2 and N_2 were irradiated with keV
electrons and ions. Stopping cross sections and ranges of 0.3-
10 keV/amu light ions in solid H_2 and D_2 are in good agreement
with experimental and theoretical data on gaseous targets. In
contrast, both stopping cross section and range measurements
in solid N_2 suggest that the stopping here is only about half
of that in N_2-gas. This "phaseeffect" is further supported by
secondary electron emission measurements.

Secondary electron emission coefficients for 2-10 keV H_1^+, H_2^+,
H_3^+, D_3^+, D_2H^+, $^4He^+$, $^{14}N^+$ and $^{20}Ne^+$ incident on solids H_2, D_2
and N_2 are in reasonable agreement with previous results for
electron-incidence.

The rather large erosion yields for 1-3 keV electrons incident
on solid D_2 depend strongly on target thickness (for thin films),
but weakly on energy. Bulk yields for 2 keV electrons were
~ 8 H_2/electron, ~ 4 D_2/electron and ~ 0.5 N_2/electron.

Secondary ion emission during ion bombardment seems to be pre-
dominantly reflected projectiles in the case of N_2-targets,
while it may be explained as sputtered particles from H_2- and
D_2-targets.

Preliminary results cn the erosion of solid H_2 and D_2 by keV
light ions indicate very large erosion yields ($\sim$ 400 H_2/atom for
2 keV protons) increasing strongly with energy.

Most of the applied methods were new in the present context and
therefore carefylly investigated.

Submitted to the Faculty of Science of the University of Aarhus
in partial fulfillment of the requirements for the degree of
lic.scient. (Ph.D).

"He who measures the same point
twice is asking for trouble".

CONTENTS

1. INTRODUCTION

When an energetic particle penetrates the surface of a solid a
number of emission phenomena may occur: backscattering, sputter-
ing, sublimation, secondary electron emission, emission of
characteristic X-rays, photon emission, etc.

All of these phenomena are closely related to the rather general
question: What happens to the incident energy?

From the point of view of the incident particle this is a ques-
tion of energy loss. It would, therefore, be impossible to under-
stand any of the above emission phenomena without considering
the energy loss of the incident particle.

The present work is concerned with the energy losses of keV light
ions and electrons in condensed molecular gases, and the result-
ing secondary electron emission and erosion of the target. In
the case of electrons, frequent reference will be made to the
thesis of J. Schou[1], and the terminology of this work will there-
fore be used as far as possible. The present results and related
data have been or will be published in Refs. 2-10 also.

In this introduction the physical processes are described in a
cursory manner, with emphasis on aspects relevant to condensed
molecular gases. In this and later chapters, theories, models,
etc., are presented for the sake of reference, and not necess-
arily because they are ascribed any particular credibility by
the author.

In Chapter 2, the experimental apparatus and its testing, as
well as the techniques of measurement, are described. Special
consideration is given to the question of charge-up of the
target.

Stopping cross sections and ranges of 0.3 - 10 keV/amu light
ions in solid H_2, D_2, and N_2 were determined (Chapter 3) by two
independent methods. The applicability of each method was inves-
tigated, and the results of both were found to agree. The results
are compared to experimental and theoretical data on gases, and
good agreement is found[2] for H_2 and D_2. For solid N_2 the stopping
cross section[3,4] is only ~ 50% of that for gaseous N_2. This dis-
crepancy is further supported by results derived[4] from the ob-
served secondary electron emission (Chapter 4), i.e. by a totally
independent method. Chapter 3 also contains a short discussion
of the stopping of electrons on the basis of existing range
data[11,12].

In Chapter 4 are presented the secondary electron emission co-
efficients for 2 - 10 keV H^+, H_2^+, H_3^+, D_3^+, D_2H^+, $^4He^+$, $^{14}N^+$
and $^{20}Ne^+$ incident on solid H_2, D_2[5], and N_2[4]. The results are re-
lated to the corresponding stopping cross sections; they support
the observed "phase effect" in the stopping in N_2. Included in
the discussion are existing data[12,13] for incidence of electrons.

In Chapter 5 the erosion of solid D_2[7,8], H_2[8], and N_2[9] by 1 - 3
keV electrons is studied: The rather large erosion yields are
found to depend strongly on target thickness for these films, but
weakly on energy. On the basis of the present results, we are
unable to relate this behaviour to stopping theory in a convinc-
ing manner. However, there are indications[8,9,14] that this may
soon become possible.

The emission of positive particles from solid H_2 and D_2 during
ion bombardment may be explained[5] by ordinary sputtering theory
under reasonable assumptions (Chapter 6). This is not the case
for solid N_2[4], where reflection might become important. The
erosion of solid hydrogens by keV light ions is far from being
understood, but preliminary measurements[10] suggest that it is
related to both electronic and nuclear energy loss. Certainly
the very large erosion yields may not be explained by ordinary
sputtering theory.

Finally, a short resumé is given in Chapter 7 of the most im-
portant conclusions.

1.1. Energy loss and scattering

A charged particle slowing down in a solid may transfer energy
to the solid in various ways:

1) by nuclear reaction,
2) by elastic scattering on nuclei,
3) by excitation and ionization of projectile and/or target, or
4) photonemission - socalled Bremsstrahlung or Cerenkov-
   radiation.

The latter may become dominant at relativistic energies, but is
negligible in the present energy range, as are nuclear reactions.

The **atomic** stopping cross section

$$S_p (E) = - \frac{1}{N} \frac{dE}{dX}$$ (1.1)

for a particle p of energy E is usually expressed as a sum of
an **electronic** and a **nuclear** stopping cross section:

$$S_p(E) = S_{p,e}(E) + S_{p,n}(E)$$ (1.2)

according to mechanisms 2 and 3 above. N is the **atomic** density
of the solid.

The term stopping power will be used for the quantity

$$- \frac{dE}{dX} = NS_p(E)$$ (1.3)

Of course, stopping is directly correlated to scattering, but
simplifications may be made.

i) Fast electrons:

The elastic energy loss in an electron-nucleus collision is more than three orders of magnitude smaller than the corresponding energy loss in an electron-electron collision, and may thus be ignored for fast electrons[1].

Independent of the detailed types of interaction with the electrons of the solid, the total electronic stopping cross section for keV electrons should be quite accurately determined by Bethe's formula[15]

$$S_{e,e}(E) = \frac{2\pi Z_2 e^4}{E} \ln \frac{aE}{I} \qquad (1.4)$$

Z_2 is the atomic number of the solid and $-e$ the electron charge. I is the mean ionization potential and the constant $a \approx 1.1658$ is independent of the target material.

The probability of scattering through appreciable angles is small at high energies, and for most targets scattering on nuclei is dominant. The total cross section for elastic scattering on nuclei (light elements) in the non-relativistic regime may be expressed as[1]

$$\sigma_{el} = \frac{\pi}{4} \frac{z_2^2 e^4}{n_s(1+n_s)E^2} \qquad (1.5)$$

where the screening parameter n_s is determined by[16,1]

$$n_s = \frac{1.7 \cdot 10^{-5} z_2^{2/3}}{\tau(\tau+2)} \qquad (1.6)$$

and τ is the kinetic energy in units of the electron rest mass. In the cases of interest here n_s varies between $1.5 \cdot 10^{-3}$ and $3.2 \cdot 10^{-3}$.

ii) Slow electrons:

The following mechanisms for energy loss of slow electrons may play a role in the interior of a solid:

1) interaction with conduction or bound electrons,
2) electron-plasmon interaction,
3) electron-phonon interaction, and
4) interaction with lattice defects.

Usually the first two processes dominate down to energies comparable ɔ the threshold for plasmon excitation. In the specific case of molecular gases the excitation of vibrational and rotational states is substantial for the slowing-down of very slow electrons[17]. It has here been suggested[18] that higher molecular excitation energies result in smaller "ranges" of secondary electrons in solid H_2 than in D_2.

The question of electron range is slightly complicated. Since in our case the low energy electrons are frequently scattered into larger angles by the nuclei, they are expected to move almost like diffusing particles.

iii) Slow ions:

For any ion at low energies the stopping cross sections are usually estimated using the Thomas-Fermi statistical model of the target-atom. According to this model all atoms have the same shape, electronic velocities scaling with $Z^{2/3}$, characteristic lengths with $Z^{-1/3}$, and the ionization potential I with Z. The limitations of the model are illustrated by a plot[19] of the ratio I/Z vs. Z: Oscillations at high Z suggest that only "average" values may be derived, and at Z << 20 the assumptions break down clearly.

Within the Thomas-Fermi picture the electronic stopping is found to be proportional to projective velocity, the specific dependence given by[20]

$$S_{i,e} = \zeta_{\epsilon} \cdot 8\pi e^2 a_0 \frac{z_1 z_2}{z} \frac{v}{v_0} \qquad (1.7)$$

with $z = (z_1^{2/3} + z_2^{2/3})^{3/2}$

Here, z_1 and v are atomic number and velocity of the projectile, while a_0 and v_0 are Bohr radius and velocity of the hydrogen atom. The factor $\zeta_{\epsilon} = z_1^{1/6}$. Eq. 1.7 is supposed to be an average estimate for $v << v_0 z_1^{2/3}$, but the validity for our targets is not obvious, and for a particular projectile-target combination it may be off by as much as a factor of 2!

Experimentally $S_{i,e}$ has been observed to oscillate strongly[19,21,22] with z_1, and z_2-oscillations are also expected[21].

The scattering of ions on electrons is negligible, so we consider only scattering on nuclei:

For screened Coulomb interaction between an ion and an atom Lindhard et al.[23] derived an approximation of the differential scattering cross section

$$d\sigma = \pi a^2 \frac{dt^{1/2}}{t} f(t^{1/2}) \qquad (1.8)$$

where $t^{1/2} = \epsilon \cdot \sin\theta/2$. θ is the CMS scattering angle and $\epsilon = a/b$ is the ratio of the screening parameter a to the collision diameter b. The function $f(t^{1/2})$ was calculated for the collision of neutral Thomas-Fermi atoms, and may be approximated by the analytical expression[24]

$$f(t^{1/2}) = 1.309 \cdot t^{1/6} \cdot [1 + 1.9 \cdot t^{4/9}]^{-3/2} \qquad (1.9)$$

The nuclear stopping cross section is determined by numerical integration:

$$s_{i,n} = \int_0^{T_{max}} T d\sigma \tag{1.10}$$

where T is the energy loss corresponding to the scattering angle θ. A comparison of Sigmund's analytic fit[25]

$$s_{i,n} = \frac{9}{8\epsilon} \{ \ln(X+r) - X/r \} \tag{1.11}$$

where

$$X = 1.378 \ \epsilon^{4/9}$$
$$r = (1+X^2)^{1/2}$$

to numerical results shows very good agreement for the ε-range of interest in the present work. It should here be noted, that more rigorous computations[26] than those of Lindhard et al.[23], also based on Thomas-Fermi potentials, show deviations from Lindhard's stopping cross section of over 10% in the same ε-range, so Eq. 1.11 is just as good as numerical values.

The $s_{i,n}$ of Eq. 1.11 is in socalled dimensionless units[23],

$$s_{i,n} = - \frac{d\epsilon}{d\rho} \tag{1.12}$$

where

$$\rho = xN\pi a^2 \frac{M_1 M_2}{(M_1 + M_2)^2} \tag{1.13}$$

and M_1 and M_2 are the masses of ion and targetatom. With lengths x in units corresponding to those of the target density N and the Thomas-Fermi screening parameter $a = 0.8853 \cdot a_0 \cdot^{-1/3}$ we may convert $s_{i,n}$ to $(10^{-15}$ eV cm^2/atom) by means of

$$S_{i,n} = 8.471 \cdot \frac{Z_1 Z_2}{(Z_1^{2/3} + Z_2^{2/3})^{1/2}} \cdot s_{i,n} \tag{1.14}$$

Although all our stopping cross section measurements are con-
cerned with reasonably high reduced energies ($\epsilon > 1$) calcu-
lations[27] made with more realistic interatomic potentials suggest
that Lindhard's nuclear stopping cross section may be in error by
up to 25%.

1.2. Phase effects

Whereas experiments on gaseous targets may give useful infor-
mation on basic processes/interactions there are bound to be
many effects which depend on the phase of the target material.
Most obviously the phenomenon of sputtering is directly related
to the phase, but also other effects of phase or density should
be expected.

In a solid many atoms will interact simultaneously with the inci-
dent particle and with another. The positions of electrons are
generally correlated over several atoms/molecules, whereas in
low density gases they are correlated only over distances of the
order of molecular diameters.

It was believed until the 1950's that the stopping in molecular
solids could be treated on the same basis as gases, but this
proved to be uncertain because of the possible influence of
electric interaction between densely packed molecules[28].

Still, for all materials with Van der Waals binding the inter-
action between molecules is small in comparison with the inter-
action between the atoms inside the molecule, so the electron
levels in the molecule are only slightly perturbed by conden-
sation.

One rather obvious feature of the condensed phases, which has
many important effects, is the presence of a surface. For in-
stance, the effect hereof on the charge state of an ion may be
very important for the considerations of Chapter 3.

1.3. Sputtering

We shall define sputtering as the emission of atomic particles from surfaces under energetic particle bombardment.

We are primarily concerned with the erosion of the bombarded surface, measured in terms of the sputtering yield Y which is the average number of emitted target atoms per incident particle.

Obviously sputtering is simply a particular type of radiation-induced displacement of target atoms, i.e. it may occur when an energy larger than some minimum, U_o, has been transferred to an atom close to the surface.

This may happen directly or indirectly:

i) Energetic particles may transfer sufficient energy in binary collision events to set target atoms in motion. This is clearly correlated to nuclear stopping (Sect. 1.1), and is simplest to describe if we may assume that any moving particle (projectile or recoil) collides only with target atoms at rest. In that case only collisions with an energy transfer larger than the surface binding energy U_o may lead to sputtering. The linear collision cascade theory of Sigmund[29] has been quite successful in explaining the sputtering of metals by heavy ions:

For normal beam incidence on a planar surface

$$Y = \frac{\Delta x}{\pi^2 U_o} \, F_D(0) \qquad\qquad (1.15)$$

where $F_D(o)$ is the energy deposition rate (per unit length) at the surface ($x \approx 0$), and Δx is a depth over which the deposited energy contributes to Y. Determining Δx from low-energy stopping theory and allowing for non-normal incidence we obtain the famous formula[29]

$$Y \approx \frac{0.042}{U_o \, [\text{Å}^2]} \cdot \alpha \cdot S_{p,n}(E) \qquad\qquad (1.16)$$

where α is a numerical factor depending on angle,energy and the projectile-target mass ratio, and is calculated by transport theory[29-32]. Because of the simplicity of Eq. 1.16 this is used as reference in most determinations of sputtering yields, also for cases clearly outside the range of applicability. Thus, most recent experimental results on non-linear effects are reported in terms of their deviation from Eq. 1.16. It may be important, however, to distinguish between truly non-linear effects, and deviations due simply to high-yield sputtering[33].

For very high yields it is not plausible that all the atoms emitted by a single collision cascade originate from near the initial surface, and Eq. 1.15 should be modified to

$$Y_N = \frac{h}{\gamma^2 U_o} \int_0^h F_D(x)dx \tag{1.17}$$

where h is the depth over which the deposited energy contributes to Y_N. This may easily enhance the calculated yield by half an order of magnitude[33]. Furthermore, crater formation may increase the exposed surface area, and perhaps reduce the surface binding energy[34-36]. It is also suggested[37], that fast sputtering itself leads to an effective reductioin of the surface binding. Thus, high yields by themselves are not proof of non-linear effects.

In a "spike" two moving particles may collide, so that even a smaller energy transfer may lead to sputtering. This situation occurs for a sufficiently short mean free path between collisions with a significant energy transfer ($> E_{min}$). The minimum energy is some energy negligible compared to displacement energies and surface binding energy ($E_{min} << U_o$). We then have spikes for high density of deposited energy, or low E_{min}. The theory of spikes[38-40] is somewhat less complete than that of collision cascades.

ii) Both excitation and ionisation may indirectly lead to sputtering of some target materials. This may become important in our experiments, where the major part of the projectile energy is dissipated via electronic interactions. However, it is diffi-

cult to generalize existing experimental data[41-51] since the processes are explicit for the individual types of target material. The possibility of combined effects of nuclear and ionisation events on the sputtering[42] contributes to the confusion.

Independent of the mechanism, the sputtering yield must depend somehow on the average surface binding energy per atom, U_O, but this is not an easily accessible quantity[29,33]. Usually the sublimation energy is used for estimates, but we shall return to this question in Section 5.2.

1.4. Secondary electron emission

When an incident beam penetrates the target material, it loses energy by ionizing and exciting the atoms of the target material. The electrons thus released lose energy through various processes, and some of them may reach the surface and escape from it. These then constitute the secondary electron emission.

It is obvious that the yield of emitted electrons is closely connected with the deposition of electronic excitation energy near the target surface, i.e. with the electronic stopping cross section $S_{p,e}$ (Sect. 1.1).

The secondary electron yield may be expressed as[1]

$$\delta = \Lambda \cdot D(0,E) \tag{1.18}$$

where Λ is a material parameter, and $D(0,E)$ is the mean energy per unit depth, deposited in electronic excitation at the surface $(x = 0)$ by a projectile. Thus the secondary electron emission is formally[52] similar to the phenomenon of sputtering (Sect. 1.3.1).

By a dimensional argument we can express[52]

$$D(0,E) = \beta \cdot N \, S_{p,e}(E) \tag{1.19}$$

where β is a dimensionless function depending on angle of incidence, energy E, and projectile and target masses. This equation is quite analogous to Eq. (1.16).

The energy transport by energetic secondary electrons as well as recoiling atoms is included in the factor β. Generally β and Λ should be evaluated by means of transport theory[52], but for our target materials the large ionization energies limit the number of cascades.

1.5. Some properties of the targets

Caution must be exercised in applying theories, models and general experiences from other areas to the present targets, particularly to the solid hydrogens. One example hereof is given in Sect. 5.2. Many of the rather extreme properties of the solid hydrogens are listed in ref. 53.

The target materials used in this work (H_2, D_2 and N_2) are all homonuclear diatomic molecules with closed-shell structures, bound together by Van der Waals forces. There is a wide variation in sublimation energy (see Table 1.1) even from one hydrogen isotope to another, leading also to about four orders of magnitude difference between vapour pressures at 4.2 K. The Van der Waals attraction is almost the same for both H_2 and D_2, but the zero-point kinetic energies of the molecules in the solid are quite different. Correspondingly, also the thresholds for molecular excitations vary considerably.

The solid hydrogens are poor heat conductors[54]. The thermal conductivity and the heat capacity are both highly dependent on ortho-para composition, as well as on crystal structure. Normal hydrogen gas cooled rapidly from room temperature will have a slow ortho-para conversion, and can usually be taken as unchanged in our experiments.

Table 1.1. Some properties of solid H_2, D_2, and N_2.

Property	Units	H_2	D_2	N_2	Temperature [K]
Heat of sublimation	meV/molecule	7.9	12.0	70.2	0
Density	10^{22} molec./cm^2	2.68	3.05	2.21	
Triple point	°K	13.9	18.7	63.14	
V.d.Waals' binding energy	meV/molec.	~26	~26		0
Zero-point kin. energy	meV/molec.	~18.5			0
Thermal conductivity	W/cm·K	0.0025	0.0046		4
Heat capacity	J/mol·K	2.1	0.95		4
C_p		2.9	2.8	5.7	10.4
Vapour pressure	Torr	$1 \cdot 10^{-6}$	$7 \cdot 10^{-11}$	$\ll 10^{-13}$	4.2
Thermal diffusivity	cm^2/sec	0.0268	0.09551		4
Lowest rotational excitation energy	meV	44	22	1.5	
Lowest vibrational excitation energy	meV	516	360	289	

Supposedly, hydrogen or deuterium condensed from vapour in thin films have a tendency to establish a face centered cubic structure[55]. The quality of our films is considered in Sect. 2.1.i.

1.6. Applications of results

i) Astrophysics: It has been suggested[56,57] that condensation of hydrogen on graphite grains at ~ 3 K might promote the formation of galaxies and stars. The destruction and growth of dust grains in space is influenced not only by heat loads and gas densities[58], but also possibly by effects like sputtering[59-61] by electrons and ions.

ii) Atmospheric physics: The presence of N_2 in the atmosphere makes data on this of interest in connection with phenomena like auroral and airglow emissions[16,62].

Some of the heavy planets[63], notably Jupiter[64], have considerable contents of hydrogen in their atmospheres, which are exposed to large fluxes of low (keV) energy charged particles[65].

iii) Health physics: Data on radiation effects in hydrogen and nitrogen are of obvious interest in health physics[66]. The possibility of a large phase effect in the energy loss of charged particles is of importance in dosimetry and, in particular, in cavity chamber theory and practice[67,68].

iv) Cryopumping: The use of superconducting magnets in connection with a vacuum chamber may cause condensation of large amounts of gas on various surfaces. One may also choose to exploit the cryopumping directly for the contamination-free pumping of vacuum chambers[58,69].

Both in the case of storage rings[70] and certain types of plasma physics experiments the condensed gas layers may be exposed to energetic particle bombardment, leading to desorption or sputtering.

v) Pellets: Independently of the above possible applications the present research was sponsored solely with the aim of injecting frozen pellets into plasmas and perhaps even into a future fusion reactor[71-75].

For economic operation of a fusion reactor it will be necessary
to maintain the reactions much longer than the particle confine-
ment time. One will therefore need to add fuel particles during
the burn in order to replace particles lost through diffusion
and fusion.

One possible fueling technique is the injection of pellets of
frozen deuterium and tritium[75]. Furthermore, such pellet in-
jection might be exploited for plasma profile shaping, improving
particle confinement time and reducing power requirements for
ignition[76].

However, injecting a fuel pellet of D-T ice at ~ 4 K into a
thermonuclear plasma at ~ $2 \cdot 10^8$ K a very high pellet velocity
is needed. How high a velocity is required must depend, among
other factors, on the physical processes occurring in or near
the pellet when exposed to the plasma.

This explains our interest in the behaviour of the solid hydro-
gens, but also other materials might be injected into a plasma:
There appears to be an increasing interest in the possibility
of depositing a known amount of an impurity locally in a plasma,
both for the purpose of plasma diagnostics and perhaps for
otherwise modifying the plasma properties. Solid nitrogen is
here an unlikely candidate, but several other possibilities
have been mentioned, notably Ne, Ar, and Xe. The study of con-
densed gasmixtures[6,14], however, requires some knowledge of the
individual components.

vi) Applicability: One should exercise great care in applying
the present results to any of the above, complex, problems. For
instance, a major difference between our experiments and the
injection of a pellet into a plasma is the presence of a sub-
strate under our films. This substrate is an electrical and
thermal conductor and is seen to influence the charge-up, and
sometimes the erosion and reflection properties of our targets.

Furthermore, particle fluxes are typically very different in the
two cases, and most of the present experiments are confined to

perpendicular incidence. Finally, in our experiments we exclude
the possibility of simultaneous bombardment by electrons of
several energies.

Still, the behaviour of the condensed gases under charged par-
ticle bombardment is apparently rather complex and little under-
stood, so empirical extrapolations of observations are bound to
be guesswork. Instead theoretical models might perhaps be tested
on the present results, if these are interpreted with sufficient
caution:

"Complex problems have simple, easy-to-understand wrong answers".
(Grossman)

2. EXPERIMENTAL APPARATUS, ETC.

The basic experimental set-up has been described in detail else-
where[12,77] and for most parts only a short description will be
given here. Special attention will, however, be given to features
which are new, or of special importance to the present work.

Schematically, the set-up (Fig. 2.1) consists of a cryostat with
a target chamber (Sect. 2.1), an ion accelerator with beamhand-
ling system (Sect. 2.2), and an electron gun on the side of the
target chamber (Sect. 2.3). Sometimes the electron gun is re-
placed by an electrostatic analyser (Sect. 2.5).

Of special concern were topics like the quality and precision of
target films, the effect of substrates, the quality of primary
beams, etc.

When a beam hits a solid target both reflected projectiles and
secondary particles are emitted in all directions. These are
detected either as total emission coefficients (Sect. 2.4) or
as relative energy distributions at a given angle (Sect. 2.5).
The methods of data accumulation, of course, depended on the
type of measurement (Sect. 2.6), and furthermore were developed
and improved during the course of experiments.

A problem of particular concern is the possible charge-up of
target films during irradiation, and the question remained to
ascertain whether or not this would affect the results
(Sect. 2.7).

THE EXPERIMENTAL SET-UP

Fig. 2.1. The experimental set-up.

2.1. The target chamber

A liquid-helium cryostat is mounted on top of a vacuum chamber which is pumped by a 10 cm diffusion pump trapped by a liquid nitrogen trap. The vacuum was normally below $2 \cdot 10^{-8}$ Torr with a cold cryostat.

The interior of the chamber is shown in Fig. 2.2: A metal substrate (see also below) is suspended below the cryostat in thermal contact with this but electrically insulated from it. Thus
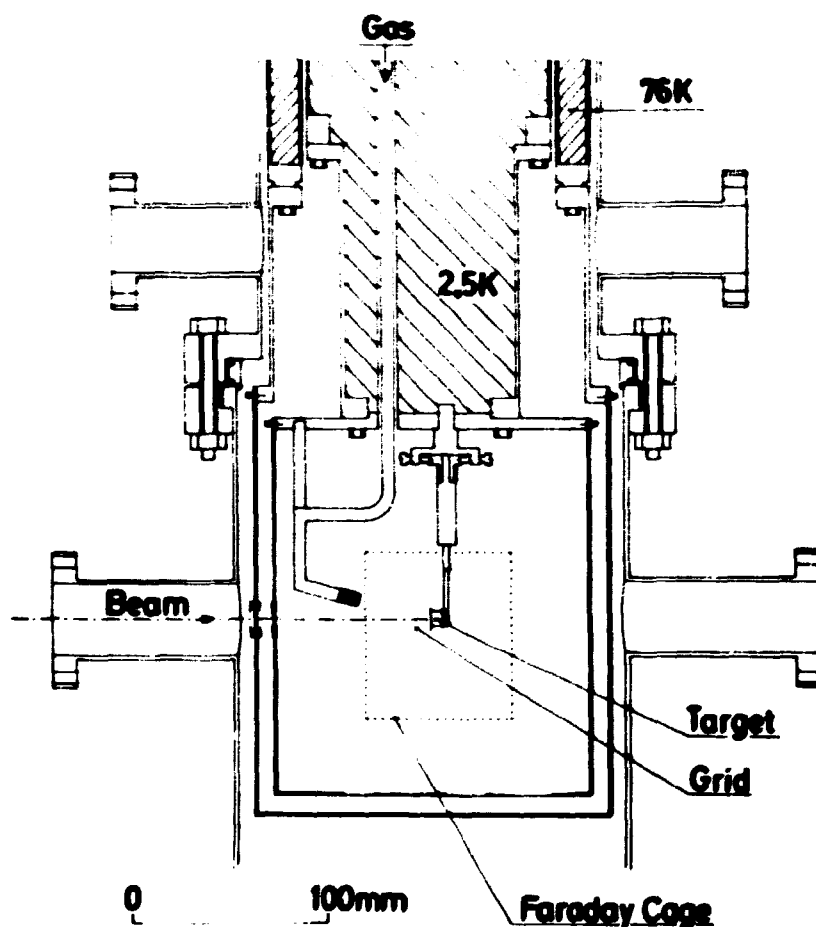

Fig. 2.2. Schematic drawing of target chamber, in the configuration used for charged emission measurements.

we may measure current collected on the substrate (see Sect.
2.4). Sometimes a very open grid is placed in front of the sub-
strate (see Sect. 2.4), also electrically insulated from the sur-
roundings.

A Faraday cup is placed below the target (substrate). The opening
of this has a diameter of 6 mm, but for erosion experiments with
electron beams both the cup and the target were covered by
smaller apertures (see Sect. 2.3).

The substrate, the cup and the grid (when used) are protected
against disturbing fields by an electrically grounded Faraday
cage, and two shields protect the target region against thermal
radiation from the surroundings.

The temperature of the substrate is usually kept low enough to
prevent significant evaporation of gases condensed on it, while
grid, cage and cup are heated by means of electrical heaters to
temperatures sufficiently high to prevent most condensation (see
Sect. 2.1.i).

A "beam-shutter" is mounted on the wall of the target chamber.
When the target is not being irradiated we may thus cover the
hole in the radiation shield towards the beamline. In the case
of the electron gun this prevents unnecessary thermal radiation
from the filament to the target. When using ions, the "shutter"
prevents gas from the beamline and the ion source from condensing
on the target between irradiations. Furthermore, the beam is
turned "off" by deflecting it in the beamline (Sect. 2.2); this
operation, of course, does not affect all the neutral particles
in the beam (Sect. 2.2.ii.d).

i) Films: A target film is produced by letting a jet of cooled
gas impinge on the substrate, which is kept at a temperature low
enough to ensure condensation. For N_2-targets the liquid-helium
temperature of 4.2 K is quite sufficient. For H_2 and D_2 the
helium bath was cooled to ~ 2.2 K by pumping.

The films are removed again by heating the substrate by means of an electrical heater.

Gas from a 5 l container held at a constant pressure is led into the vacuum chamber through a needle valve and a cooled gas tube (Fig. 2.2), the gas flow being started and stopped by means of electromagnetic valves. The gas flow rate, and thus the film growth rate, depends on the feeding pressure and the needle valve setting. For various combinations of these parameters the system is calibrated with a quartz-crystal film thickness monitor (resonance frequency ~ 5 Mc/s) placed at the position of the target plate. Calibrations were repeated from time to time, and normally a reproducibility of 5-10% was obtained over a period of years.

The quartz-crystal yields the film thickness directly in units of (g/cm^2). We, therefore, generally express thicknesses in atoms/cm^2, whenever the absolute value is important. However, in some cases it seems more illustrative to express a film thickness in Å, when only a qualitative picture is needed. In that case the thickness is estimated assuming bulk densities of the solids (see Table 1.1).

Particular consideration was given to the question of the reliability of the thickness measurements at the present temperatures (see below).

Only a small central fraction (4-8%)[77] of the gas would hit the target plate, ensuring a very uniform film thickness. The initial quality of the films has been carefully considered previously[77], and it is believed to be good. Still, a microcrystalline structure cannot be excluded (see Sect. 1.5).

ii) Quartz crystal oscillator: The quartz resonator basically consists of a quartz plate having a mechanical resonance frequency f inversely proportional to its thickness, i.e. f = K/t. The resonant frequency is measured electrically through the

piezo-electric effect. An added mass in the form of a thin film
has an effect on frequency very nearly that of an equivalent
mass of quartz.

The temperature coefficient of such a quartz plate is a function
of orientation with respect to its crystallographic axes, but at
temperatures below ~ 12°K it should generally be negligible[78].
This was confirmed by monitoring the resonance frequency during
cooling.

One might still expect f to be sensitive to temperature gradi-
ents[78]. The crystal is not well coupled to its holder thermally,
and the surface is heated by the gas durir.r deposition. Further-
more, although the thermal boundary resistance between a hydrogen
film and a metal substrate may be anomalously low[79], we may, in
general, expect a temperature gradient over the interface. As
our target materials are rather poor heat conductors (Table 1.1)
there will therefore probably be a (small) temperature difference
between the surface and the center of the plate. However, such a
temperature gradient must decrease with time as equilibrium is
approached after the deposition, and the frequency f was seen to
reach a constant level after a few seconds.

Besenbacher et al.[46] measured the thicknesses of Ar-films at
~ 6 K both with a quartz crystal and by Rutherford backscattering
(RBS), finding a difference of ~ 20%. They suggest that the cali-
bration constant of the crystal is changed due to beam-induced
damage or temperature dependence.

Beam effects might have been identified by measuring the same
film thickness first with a new (undamaged) crystal and then
with RBS. Apparently this was not done.

Our crystal is never bombarded with energetic ions, but tempera-
ture effects, should they occur, would of course be of concern.
Although such effects seem unlikely at these temperatures (see
above) we therefore compared the calibration constant of the
crystal below ~ 12 K with that at room temperature: First the
resonance frequency f was determined at both temperatures

($\sim$ 4.2 K and $\sim$ 293 K) several times during a week, heating/
cooling in between. During this period $f_{4.2}$ varied within
4969561 $\pm$ 33 c/s and f_{293} within 4975662 $\pm$ 9 c/s, demonstrating
the reproducibilities in the same set-up and mounting.

Then the crystal was removed and mounted instead in a vacuum
evaporation chamber, giving f_{293} = 4975665 c/s! Thus, remounting
of the crystal apparently causes little change in f (see also
ref. 77).

Now a layer of Ag was deposited on the crystal, reducing f_{293} by
5055 c/s in the evaporation chamber. Remounting the crystal again
under the cryostat the corresponding change in f_{293} was found to
be 5060 c/s. Finally, when cooling again we found that $f_{4.2}$ was
reduced by 5054 c/s since last. Thus, any temperature effect
seems to be within the reproducibility of crystal measurements,
and apparently causes less than 1% error in the film thickness.

iii) Substrates: As substrate we usually use a 12-mm diameter
polished gold plate (in Sect. 3.4.iii also a carbon plate), but
it was very difficult to maintain a clean metal substrate at
these low temperatures. In particular, the reflection of low-
energy ions ($\sim$ 1 keV/amu) was very sensitive to surface purity.
Frequently, measurements had to be terminated and the set-up
opened, due to contamination of the substrate-surface.

During the backscattering measurements (Sect. 3.4.v) this problem
was avoided by first covering the metal plate with a very thin
($\sim$ 1.5 μm) Xe-film. This was deposited in situ on the cold target
plate by means of an independent, warmer gas tube (not shown in
Fig. 2.2). By renewing the Xe-film frequently we maintain a very
clean substrate surface. Working only with much more volatile
target materials (H_2, D_2, and N_2) we may remove these by heating,
without disturbing the Xe-"substrate".

Unfortunately, Xe would also tend to condense on the grid in front
of the target and charge up during irradiation. It was therefore
not possible to use a Xe-substrate for measurements where this
grid was used to suppress secondary emission (see Sect. 2.4).

2.2. Ion beams

i) Beams of 1-10 keV H_1^+-, H_2^+-, H_3^+-, D_3^+-, $^4He^+$-, $^{14}N_1^+$, and $^{20}Ne^+$-ions are extracted from a duoplasmatron ion source and selected by a $45°$ magnet. D_1^+- and D_2^+-ions unfortunately may not be distinguished from H_2^+- and H_2D^+-ions, respectively. There is little doubt that the latter are indeed present even when we have worked with only D_2-gas in the ion source for several weeks, because we also observe substantial amounts of ions with mass 5 (D_2H^+). Also we were not able to use N_2^+-beams, because such beams would be contaminated with ions from cracked oil from the diffusion pumps.

The energy of an ion beam is defined by the extraction voltage, and believed to be quite accurate.

The beam current i_b is determined by deflecting the beam into the Faraday cup (Fig. 2.2) by means of the last set of deflection plates in the beamline (Fig. 2.1). The intensity profile of the beam may be estimated by sweeping the beam across the 6 mm circular opening in the cup: It seems reasonable to assume that the beamhandling system produces an oval beam, and due to the horizontal deflection in the magnet we might expect the horizontal axis to be the larger[80]. Sweeping such a beam first horizontally and then vertically across the Faraday cup we obtain two curves of collected current versus deflection voltage rising from zero (outside the opening) to a constant level (when the whole beam enters the cup) and then falling to zero again. These curves may be interpreted, by simple geometrical arguments, to yield the horizontal and vertical widths of the beam, as well as an indication of the homogeneity. Typically a well-focused 8 keV D_3^+-beam would have a horizontal width of ~ 2 mm and a vertical width of ~ 3 mm.

Both beamhomogeneity and -intensity would deteriorate at lower energies, and for a 1 keV H_1^+-beam only a current of a few nA could be obtained. Whenever acceptable (see Sect. 3.4.ii) we would therefore use molecular ions to achieve higher current densities at lower incident energies per proton.

Beams may be pulsed by deflecting and releasing them by means
of the deflection plates after the magnet. Typical rise times
for the beam pulse are ~ 1 μs.

ii) Investigation of beam quality

During testing of the analyzer (Sect. 2.5.2) the energy distri-
butions of various low-energy ion beams were measured after
optimization of the intensity profile. The resulting average
energies agreed with the nominal acceleration voltages to better
than ± 5 eV, for energies between 2.5 and 2.8 keV.

a) Energy spread: In the spectrum of a 2.5 keV H_1^+-beam the peak
    had a FWHM equal to the minimum energy window of the analyzer
    (Fig. 2.3), namely 18 eV. From this we estimate an energy-
    spread in the detected beam of the order of 10 eV or less,
    i.e. probably less than the energy spread from the ion
    source.

b) Slit scattering, etc.: Secondary peaks of energies typically
    15–150 eV below the primary energies were interpreted as
    caused by inelastic scattering in the beamline. In some cases
    this could be avoided by adjusting the beam. Beam limiting
    apertures were introduced at several points of the beamline
    until secondary peaks could no longer be produced even on
    purpose.

c) Dissociation: In the energy spectrum of a 2.5 keV H_3^+-beam
    two smaller peaks were observed around 840 and 1660 eV.
    Correspondingly for a 2.5 keV H_2^+-beam also a small peak at
    1250 eV was found. The magnitude of the smaller peaks varied
    with the pressure in beamline and target chamber and became
    negligible under good vacuum conditions. This phenomenon was
    interpreted as dissociation of the H_3^+-ions caused by
    collisions with restgas after the magnet (compare Sect.
    3.4.ii).

d) Neutrals: Measuring with channeltron No. 2 (see Sect. 2.5.1)
    in direct continuation of the beamline, all beam particles are
    detected, independent of charge state. Since neutral particles
    must have been neutralized in the beamline after the magnet
    (Fig. 2.1), these must have essentially the same energy (and
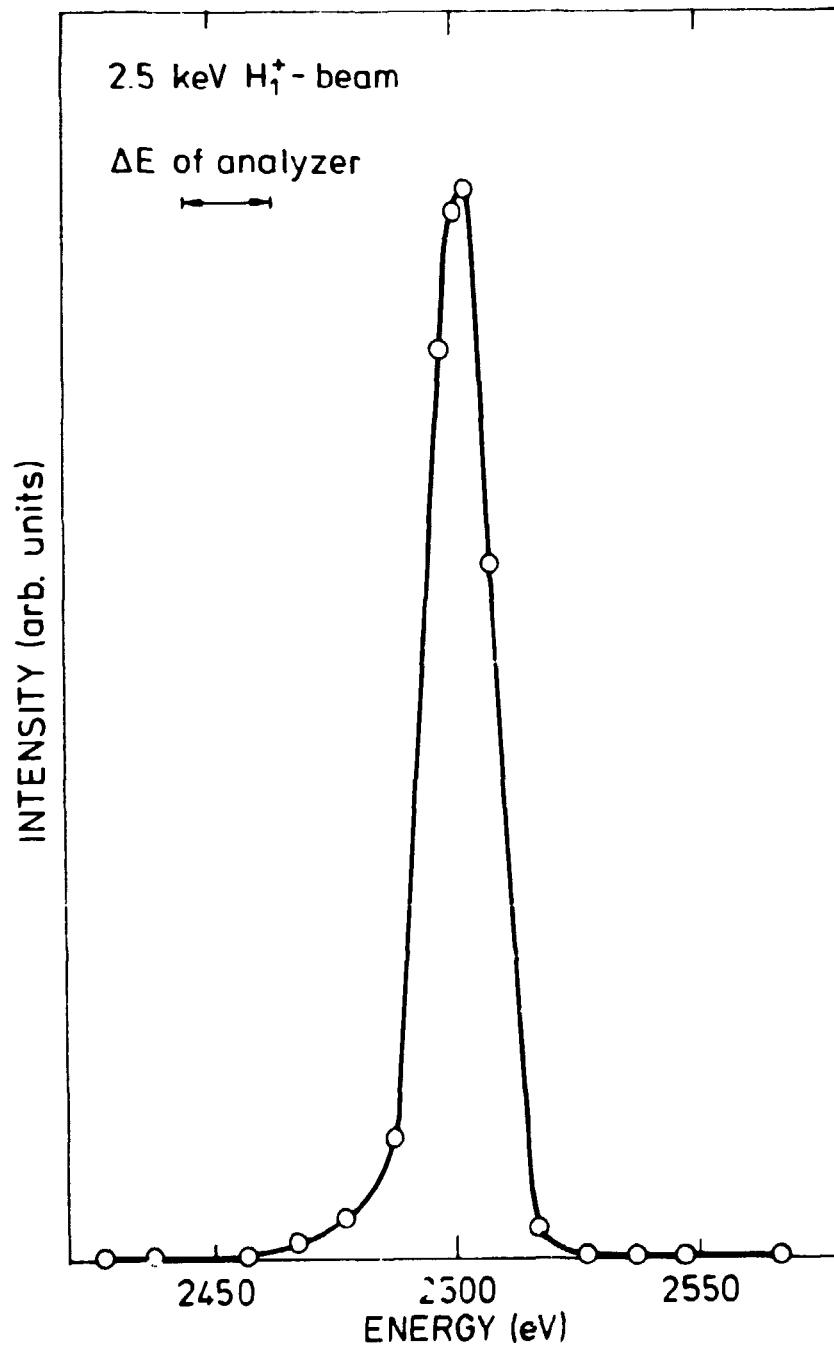   thus counting efficiency) as the charged particles. On apply-

Fig. 2.3. Energy distribution of 2.5 keV H_1^+-beam in target chamber. Energy window of analyzer ~ 18 eV.

ing a large positive bias to the analyzer, only neutral and
negative particles were detected. In this manner it was
checked that under good vacuum conditions ~ 99% of the beam
was positive.

However, it should be noted that even a small contribution of
neutrals may be important, since these are not all deflected by
electrostatic deflection (Sect. 2.1).

2.3. Electron beams

Beams of 1-3 keV electrons are obtained from a small electron
gun placed directly on a side tube to the target chamber (Fig.
2.1). The beam energy is defined by the acceleration voltage.

The beam current i_b is determined by deflecting the beam into the
Faraday cup (Fig. 2.2) by means of a set of deflection plates
(Fig. 2.1). The intensity profile of the beam may be estimated
by sweeping the beam across the Faraday cup (see Sect. 2.2).
Typically, a well-focused 3 keV beam would have a diameter of
$\lesssim$ 0.5 mm and a current of up to ~ 2 μA. At lower energies the
minimum diameter would be larger and the maximum i_b smaller.

Beams may be pulsed by deflecting and releasing them by means of
one of the sets of deflection plates on the gun used also to
adjust the beam position.

During erosion measurements the electron beam was focused as
much as possible and then swept horizontally and vertically by
two independent sawtooth voltages over a 2 mm aperture in front
of the target. The sweep frequencies were chosen so that the
beam spot would follow a Lissajou curve of high order. As dis-
cussed by Andersen et al.[81] this ensures a homogenous ir-
radiation of the target area if only the sweep system is ideal
and the amplitudes sufficiently large to deflect the beam totally
outside the aperture. The latter was easily checked by measuring
the target current i_t as a function of sweep voltage. The sweep
voltages were applied to the two sets of deflection plates on

the gun, i.e. it was possible to deflect the swept beam by means of the last deflection plates before the target chamber, so that it was swept over the Faraday cup instead. The opening of this cup was also covered by a 2 mm aperture, so that the average values of i_b and i_t may be compared directly. Both apertures were made in the same metal plate, which was mounted outside the Faraday cage just behind the opening of the gas tube (Fig. 2.2), so that it did not interfere with the deposition of gas on the target. During a vacuum failure this plate became so dirty that afterwards the electron beam caused a visible discoloration where it impinged. Thus, we could observe the traces of beams swept in one or both directions, and saw that on applying both sweep voltages we obtain a systematic irradiation of a rectangular area around each aperture.

2.4. Charged emission measurements

2.4.1. Measurements

The target plate is electrically insulated from the cryostat (Sect. 2.1), so the resulting current i_t to the target during bombardment may be measured. When a beam hits a solid surface, secondary electrons and ions as well as reflected projectiles are emitted, so i_t will generally differ from the true beam current i_b (Sect. 2.2.i). Applying bias voltages to the grid (Fig. 2.2) various parts of the charged emission may be suppressed, and thus i_t will be altered. As mentioned in Sect. 2.1.iii it was not possible to use a Xe-substrate during this type of measurement, because any Xe condensing on the grid might charge up during irradiation and disturb the charged emission.

i) Ion incidence: With a bias of -45 V most of the secondary electron emission is suppressed[82], and the measured target current i_t^- is lower than i_b. We define a "positive emission coefficient" γ by

$$i_t^- = (1-\gamma) \cdot i_b \tag{2.1a}$$

and determine

$$\gamma = 1 - i_t^-/i_b \qquad (2.1b)$$

As we shall see in Sect. 3.4.i, this positive emission consists primarily of particles with energies above ~ 50 eV. Thus a bias of +45 V is not expected to suppress this, and furthermore permits secondary electron emission. The target current i_t^+ is usually higher than i_b; we define a secondary electron emission coefficient δ by

$$i_t^+ = (1-\gamma+\delta) \cdot i_b \qquad (2.2a)$$

and determine

$$\delta = (i_t^+-i_t^-)/i_b \qquad (2.2b)$$

It was found that any bias between -30 V and -90 V gives essentially the same value for γ, i.e. almost all secondary electrons do indeed have energies below 30 eV.

ii) Electron incidence: Most secondary electrons have energies of a few eV[82]. For incidence of keV electrons we may not directly distinguish secondary from reflected electrons, but a considerable part of the reflected electrons will usually have much higher energies. As discussed in ref. 1, it is therefore an experimental convention to simply define electrons with low energies as "true" secondaries.

Such secondaries are suppressed by a bias of -45 V, and we define now the electron reflection coefficient η by

$$i_t^- = (1-\eta) \cdot i_b \qquad (2.3a)$$

and determine

$$\eta = 1 - i_t^-/i_b \qquad (2.3b)$$

Clearly then, for electrons

$$i_t^+ = (1-n-\delta) \cdot i_b \qquad\qquad (2.4a)$$

and

$$\delta = (i_t^+ - i_t^-)/i_b \qquad\qquad (2.4b)$$

In the above it is assumed that electrons do not induce any positive emission.

iii) **Measurements:** During continuous irradiation the films may deteriorate and thick films may charge up. Whenever possible this is avoided by using pulsed beams of ~ 0.5 mS duration on fresh films. However, during erosion measurements this was, of course, not possible, and the question of charge-up had to be considered (Sect. 2.7).

2.4.2. Negative ion emission

i) In Sect. 2.4.1.i it was implicitly assumed that the emission of negative ions may be neglected. If this is not so, one of our charged emission coefficients (γ or δ) is wrong. This would be unimportant for those experiments (notably erosion) where only an experimental relation between emission coefficient and target thickness is exploited (see later).

Unfortunately, no energy spectra are as yet available for negative ion emission (compare Sect. 3.4.i for positives), but if these behave like positive ions (i.e. all have energies above 50 eV) they do not influence our δ-values, contributing equally to i_t^+ and i_t^- (see Eq. 2.2b). In that case they simply constitute a correction of the measured γ-values (Eq. 2.1b).

The possible influence of low energy negative ions was investigated: A magnetic field was applied parallel to the target surface by means of a coil placed around the vacuum chamber (see Fig. 2.2). In the beam-spot region the B-field is perpendicular to the E-field between the surface and the grid, and an emitted

charged particle will tend to rotate around a guiding centre G.
During such a rotation G will ideally move in the plane of the
target surface, due both to the initial particle velocity along
the B-field and to the E/B-drift perpendicular to this. For a
sufficiently large B-field a given particle will complete a
"half rotation" and return to the target before the guiding
centre has drifted appreciably. Since the Larmor frequency is
inversely proportional to the particle mass it is then, in prin-
ciple, possible to choose a combination of B- and E-fields so
that nearly all electrons are returned to the target while all
the secondary ions still escape.

These considerations, of course, are somewhat simplified. In
reality the fields were quite inhomogeneous, and furthermore the
magnetic field had a rather large extension so that also the
incident beam was affected. The latter meant that there was, in
fact, a limitation to the field that could be applied, and we
could not be certain that all secondary electrons were sup-
pressed. Instead we therefore studied how δ was gradually re-
duced for increasing B-fields for both H_2- and D_2-targets. For
the various fields that were applied, the relative reductions
were the same for H_2 and D_2, i.e. δ for H_2 remained 0.65-0.70
times that for D_2 (see Sect. 4.2.i). If an essential part of the
negative particles were ions (not suppressed by B-fields) this
ratio would have varied somewhat, since one would not have ex-
pected the same ratio between the ion yields. As a matter of
fact negative ions would probably rather have behaved like posi-
tive ones (Sect. 6.1) in the sense that H_2 is likely to have the
largest yield. It is thus reasonable to assume that the nega-
tive particles are predominantly electrons. It appeared that the
secondary electron energies were relatively high (but see also
Sect. 2.4.1.i).

ii) In Sect. 2.4.1.ii the electron induced emission of both
positive and negative ions was neglected. This is not inves-
tigated further, because in the present work only experimental
relations between emission coefficients and target thickness
are used.

2.5. Electrostatic analyzer

2.5.1. Description

The principle of the electrostatic analyzer is shown in Fig. 2.4.
The spectrometer is a cylindrical condenser with a radius of
curvature of 30 mm, a deflection angle of 90° and 10 mm between
the plates. It is followed by a channel electron multiplier
(channeltron), and we may thus select to count the charged par-
ticles of a given energy. To minimize scattering inside the ana-
lyzer the two curved deflector plates are formed by a series of
razor blades[83]. The limiting apertures are No. 1 and No. 4 (Fig.
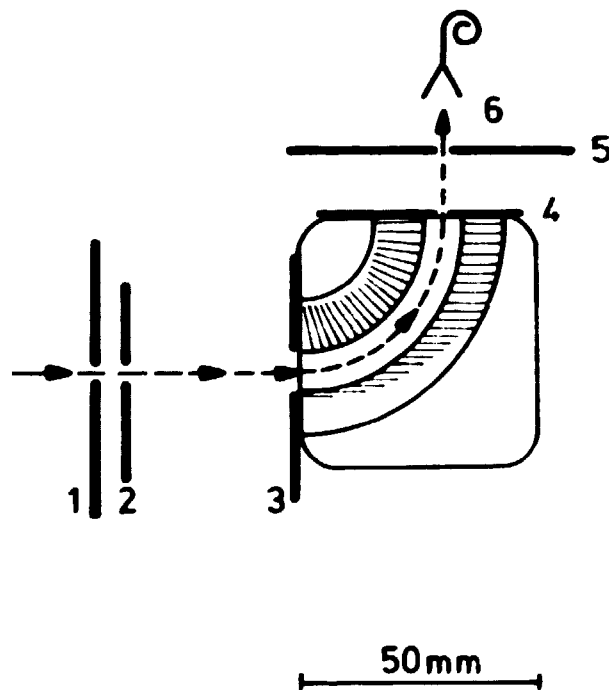2.4), and the energy window is estimated to be ~ 15% of the
energy selected.

50mm

Fig. 2.4. Electrostatic analyzer. Retarding voltage V_r.
Analyzing voltages V_r ± $\Delta V/2$ on plates. 1: 2 mm, V = 0.
2: 3.5 mm, V = 0.6 V_r. 3: 11 mm, V = V_r , grid 82% trans-
mission. 4: 3.5 mm, V = V_r. 5: 7 mm, V = 0, grid with 1 mm
holes. 6: 10 mm, V = -2.5 kV.

The energy resolution is improved by applying a retarding voltage V_r to the analyzer itself, i.e. raising everything between apertures 3 and 4 (incl.) to the voltage V_r. The analysing voltage difference ΔV between the deflector plates is then symmetric around V_r. In the actual experiments (Sect. 3.4) the analyzed energy E_a is then reduced by a factor of 5 between apertures 1 and 3, i.e. before the analysis itself. In this manner we obtain an energy window of $\sim$ 3% of E_a.

Although aperture 3 is covered with a fine grid ($\sim$ 0.25 mm holes) the effect of the retarding field is to produce a strong focusing into the analyzer (through aperture 3) of an initially divergent beam. This focusing greatly affected the transmission of the analyzer.

Applying a retarding voltage of $V_2 \sim 0.6\ V_r$ to aperture 2 (close to aperture 1) the retarding field is divided into two, with by far the stronger field between the first two apertures. Since the focusing is largest for the strongest fields and lowest energies we may thus reduce the focusing by applying the strongest field early in the deceleration (where the particle energy is highest). The optimum values for V_2 and aperture-distances were estimated by simple numerical calculations, ignoring energy dispersion.

Tests (Sect. 2.5.2) seem to prove that with the use of aperture 2 the resulting focusing is substantially reduced, and the transmission of the analyzer does not vary significantly with energy.

After analysis the positive particles are accelerated into the entrance of the channeltron by a voltage of - 2.5 keV, thus ensuring a nearly constant counting efficiency[84].

For use in tests and by alignment of the analyzer, a second channeltron (channeltron No. 2) was sometimes mounted in line with apertures 1, 2, and 3 (Fig. 2.4) so that particles passing undeflected through the analyzer would continue out between the razor blades and hit this channeltron. Thus, with the analyzer turned off all particles entering the analyzer would be detected here; otherwise only neutrals would.

Measurements of energy spectra were made independently of
emission coefficient measurements, i.e. without using the elec-
tron suppression (Sect. 2.4). During this type of measurement
the grid (Fig. 2.2) was therefore removed, and a substrate of
solid Xe could be used (Sect. 2.1.iii).

2.5.2. Testing of analyzer

The electrostatic analyzer described above was carefully tested,
both with respect to energy calibration and to transmission.

First the analyzer (Fig. 2.4) was mounted on the target chamber
directly opposite the beamline (see Fig. 2.1). The primary beam
was centered on the analyzer by means of an aperture just in
front of it: Sweeping the beam over the aperture and measuring
the current to this, a minimum was observed when part of the
beam passed through to the analyzer.

Immediately below the aperture, inside the target chamber, a
Faraday cup was placed, resembling the one mounted under the
cryostat (Fig. 2.2). Sweeping the beam over this cup, the inten-
sity profile could be measured, as described in Sect. 2.2.i.

In the present geometry, it is particularly important that the
analyzer is very accurately aligned with the primary beam. This
is ensured by maximizing the beam intensity transmitted to
channeltron No. 2 before analysis (see Sect. 2.5.1).

As many of the tests as possible were performed with the analyzer
in the operational configuration, i.e. with the channeltrons (see
also below).

i)   Energy measurement: The precision of the energy measurement
was now tested by means of the primary beams. Although only a
fraction of the beam would enter the analyzer, the channeltrons
still reached saturation for beam currents much below those
necessary to measure the intensity profile in the Faraday cup.
Therefore the beam was first optimized with respect to intensity
profile, centered on the aperture, and then strongly defocused

in the ion source to reduce the intensity before switching on
the analyzer. It was hoped that this procedure would maintain a
nice, constant but strongly reduced beam.

With constant voltages of $\pm$ 22.5V on the deflection plates, the
energy distributions of various low-energy beams were now
measured by varying the retarding potential of the analyzer.

Reducing thus the beam energy typically by a factor of 30 or
more, without a focusing voltage on aperture No. 2 (see Sect.
2.5.1), the beam was strongly defocused in the analyzer. This
contributed to the desired reduction of the detected intensity
(see above), but in a strongly energy dependent way. Simple
estimates indicated an E^{-2}-dependence of the detection efficiency
at keV energies, i.e. a prohibitive distortion of wide energy
distributions. Thus focusing and weaker retardation were applied
in the actual experiment (Sect. 2.5.1).

For the measurement of very narrow energy distributions, though,
the distortion will not affect the mean energy. As an example,
consider the energy distribution of a 2.5 keV H_1^+-beam (Fig.
2.3): The peak is centered at 2502 $\pm$ 3 eV, which is more precise
than even expected from the accelerating voltage. The width of
the peak equals the theoretically predicted energy window, i.e.
the retarding potential does not influence the energy resolution
significantly.

Several other beams with energies between 2.5 and 2.8 keV were
also analyzed, and it was concluded that in this configuration
the analyzer measures energies with a precision of $\pm$5 eV and a
resolution of better than 20 eV.

ii) Energy distribution measurement: For the measurement of
energy distributions it is essential, that the detection ef-
ficiency is independent of energy. This means, that a) the trans-
mission of the analyzer and b) the counting-efficiency of the
channeltron must both be independent of energy.

As for the latter the entrance voltage of -2.5 kV on the chan-
neltron ensures that all positive particles impinge on this with
effective energies above 2.5 keV, where the sensitivity of the
channeltron does not vary strongly with energy.

It remains to test the transmission of the analyzer, which in
the configuration above was certainly energy dependent. The
retarding voltage V_r was now chosen so as to always reduce the
selected energy with a certain factor, and the focus voltage on
aperture No. 2 was optimized and fixed to be a certain fraction
of V_r (see Sect. 2.5.1). The transmission was then tested over
the whole energy range, which was not a trivial task.

a. For keV energies we may still use the primary beams. The two
    channeltrons were both replaced by Faraday cups, enabling
    us to work with larger beam intensities and better defined
    beams (compare above). Since these cups are not on a voltage
    of -2.5 kV (as the channeltrons) this changes the "optics"
    of the analyzer, but the change is assumed to be unimport-
    ant at keV energies. However, as the intensities used now are
    many orders of magnitude larger than those observed in the
    actual experiments (Sect. 3.4), also eventual space-charge
    effects in the decelerated beams (inside the analyzer) are
    likely to be enhanced. Thus the situation may actually be
    better than the tests indicate.

    The transmission factor was defined as the ratio between
    the detected intensity I_{det} and the incident intensity I_{in}
    through aperture No. 1. Since we are interested only in
    testing whether I_{det}/I_{in} is independent of energy, we are
    satisfied with a relative measure for I_{in}:

    The intensity through aperture No. 1 was assumed proportional
    to the current I_2 measured in Faraday cup No. 2, when the
    analyzer is switched off ($V_r = 0$). This is a reasonable
    assumption for a diffuse, scattered beam entering the analy-
    zer along the axis, i.e. in the actual experiment, but for
    a primary beam it is important to avoid focusing the beam
    into the analyzer.

It is not surprising that the measured relative transmission
factor proved very sensitive to the trimming of the beam
in the beamline. Great care was taken to align the beam
with the axis of the analyzer, and defocus strongly on the
aperture in front of it.

The relative transmission factor I_{det}/I_2 was measured at
various energies from 1.5 to 3 keV, and found to be constant
within ± 10% in this energy range.

b. For eV energies no direct beam is available for testing.
Unfortunately this is the energy region where the trans-
mission is most likely to be energy dependent, so an alterna-
tive principle was used:

The analyzer was mounted on the side of the target chamber
with the cryostat in place, i.e. in the very configuration
used in the actual experiments (Sect. 3.4). As we were now
studying much lower, scattered intensities the channeltrons
were used again. Channeltron No. 2 was used to align the
analyzer with the beam spot on the target (substrate), by
simply maximizing on the scattered intensity detected. This
is, of course, much easier than to align with the primary
beam itself, as above.

A beam of 6 keV H_3^+ was now directed onto a target of
2000 Å N_2/Au and the energy distribution of the emitted low
energy positive particles reaching the analyzer was measured
with various degrees of retardation.

For the simple case of no retardation and variable, sym-
metrical deflection voltages the analyzer functions just
like the one used by Verbeek et al.[83], and we may assume
that the transmission is little (or not at all) energy
dependent. Instead, of course, the energy resolution is not
nearly as good, but the effect of this is easily recognized.
Thus, on comparing energy distributions obtained with and
without retardation, systematic distortions should be dis-
closed.

Since a broad energy distribution may be measured only by individual collection at many different energies, the stability of the emitted intensities is critical. Using a target of "bulk" N_2 we may be reasonably confident that the target surface is reproducible. Furthermore, a 6 keV H_3^+-beam is not particularly unstable, but still we must allow for fluctuations. Thus, the agreement between spectra obtained with and without 80% retardation (Fig. 2.5) is certainly satisfactory.

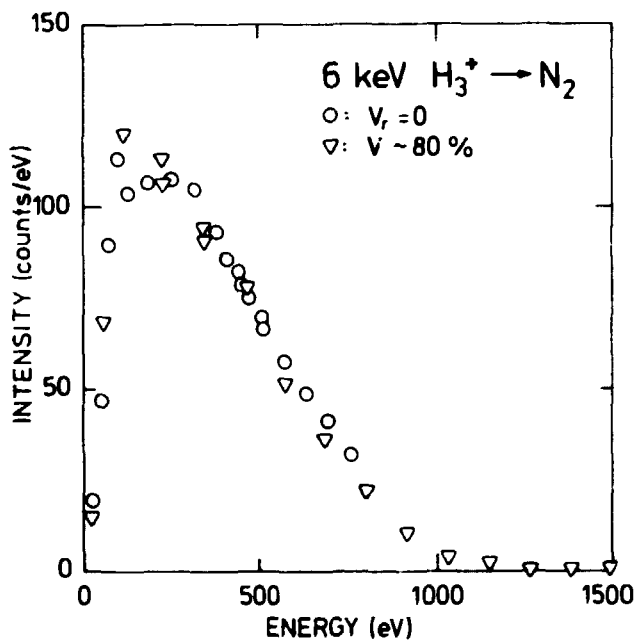For stronger retardation considerable distortion was observed.

Fig. 2.5. 6 keV $H_3^+ \rightarrow N_2$. Comparison of experimental energy distributions at 45° to surface, measured without retardation (o) and with 80% retardation (x).

2.6. Data accumulation

For most measurements of charged emission only momentary currents were needed. These currents were measured by means of a storage oscilloscope, the display of this was photographed and the relative currents were then measured from the picture[77]. This actually was sufficiently accurate for the determination of charged emission coefficients (Eqs. 2.1 - 2.4).

During the rather preliminary erosion measurements with ions (Chapter 6) the continuous target current $i_t^\pm$ (Fq. 2.1 or 2.2) was collected in a multichannel analyzer as a function of time. The variation of γ or ($\delta-\gamma$) was then evaluated from the printed output.

The erosions with electrons (Chapter 5) were made using a beam sweep (Sect. 2.3), so that $i_t^\pm$ would appear as a kind of ir- regularly pulsed current. This then had to be smoothened in an RC-filter before being digitized and collected in a transient recorder, because the aperture time of the recorder was only of the order of 40 nS. These measurements were quite automated: The recorder was operated in a pre-trigger recording mode, triggered by the onset of target irradiation. The sampling was then timed by external pulses from an ABC-80 computer, and after the col- lection of 900 samples of i_t the recorder would, in turn, ter- minate the irradiation of the target. In this manner it was ensured that all erosion would be recorded. After completion of a recording cycle the data were automatically transferred to the computer via a digital output interface. Also the data evaluation was, of course, performed by the computer.

During backscattering measurements (Chapter 3) the target was bombarded by ions for a given length of time (1 - 10 sec) while the reflected ions of the selected energy were counted in the electrostatic analyzer. Clearly this had to be repeated for many energies in order to measure a single spectrum. The discrete pulses from the channeltron were preamplified immediately before being transferred to the main amplifier. After discrimination of most of the noise in a single channel analyzer, the pulses were finally counted in a scaler.

2.7. Charge-up of films

Bombarding very thick films of D_2 by electrons or ions and apply- ing a suitable bias to the grid (Sect. 2.4) the measured target current i_t was seen to vary with time as the target charged up. As this might be important for our measurements, particularly

of erosion, the phenomenon was further investigated. It appeared
that any irradiation of a film would induce some degree of
charge-up, but that sometimes we may estimate how much, and
possibly neglect the effects:

i) Ion-incidence: Low-energy ions penetrating a solid surface
may be expected to somehow pick up electrons close to the sur-
face, and thus in effect deposit positive charges at the surface.
Furthermore, if they induce secondary electron emission, even
more positive charges are produced. As the mobility of charge
carriers in diatomic molecular solids is quite low[85] this may
then lead to charge-up.

Bombarding thick D_2-films by 7 keV H_2^+-ions, and monitoring the
target current i_t^+ (eq. 2.2.a) corresponding to a bias of +45 V,
this current was observed (Fig. 2.6) to fall off towards a lower
level, i_t^+ (∞), which depended on the film thickness x_0. This was
interpreted as caused by a decreasing secondary electron emission
due to positive charge-up of the target surface. In order for
such an effect to occur, the surface potential must at least be-
come comparable to the grid bias (+45 V). In agreement herewith,
the effect was suppressed when raising the grid bias to 90 V.

As long as the equilibrium target current i_t^+(∞) was still larger
than the beam current i_b we were obviously not suppressing all
secondary electrons. We recall (Sect. 2.4.1.i) that if the sur-
face potential just exceeded the grid bias by 30 V almost all sec-
ondary electrons would be suppressed, i.e. as long as i_t^+(∞) is
larger than i_b the surface potential was somewhere between 45 and
75 V.

For a given grid bias there appeared to be a monotonous relation
between i_t^+(∞) and x_0 up to thicknesses where i_t^+(∞) did no longer
exceed i_b. The behaviour is interpreted as follows:

Irradiation of the target film induces a conductivity along the
beam path, and the electric field between the charged surface
and the grounded substrate then creates a current through the
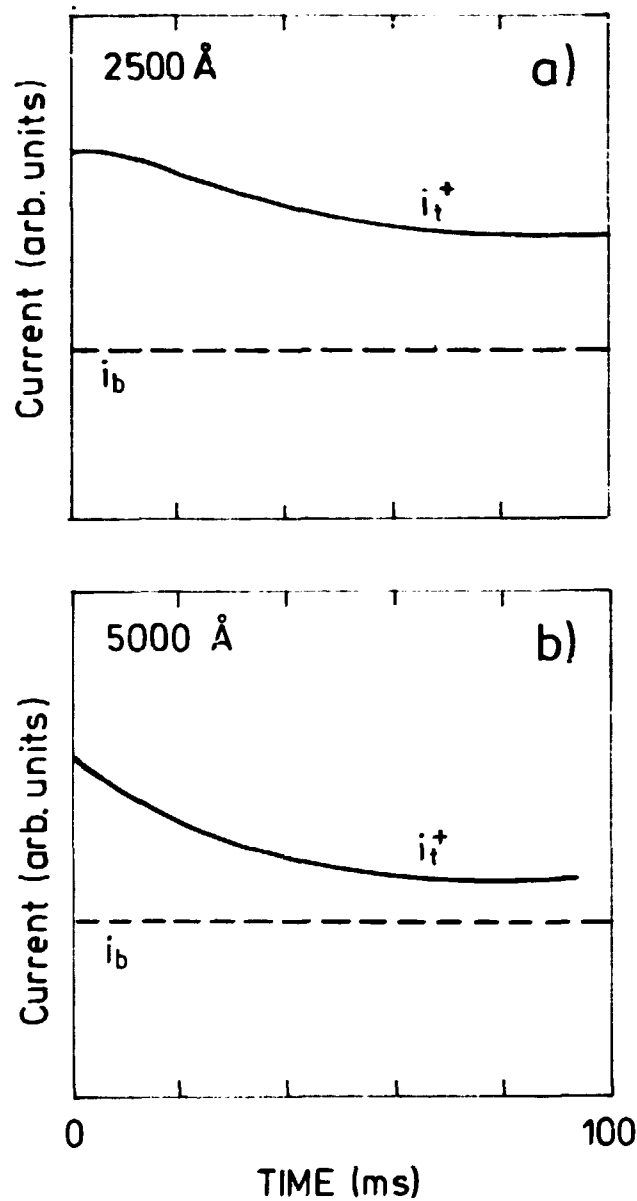film. Raising the surface potential (depositing more positive

Fig. 2.6. Target current i_t^+ vs. time for 7 keV H_2^+ incident on a) 2500 Å D_2/Au and b) 5000 Å D_2/Au. The current varies due to charge-up.

charges) then also raises the current through the film, until an equilibrium is reached where the charges deposited are transported to the substrate, so that the surface potential (and thus i_t^+) remains constant. Clearly, for larger x_o the conductivity becomes poorer, and therefore the equilibrium potential becomes higher.

In the present example $i_t^+(\infty)$ reaches i_b (the surface potential reaches $\sim$ 75 V) for $x_o \cong$ 5200 Å. For comparison, the projected range of the projectiles is $\sim$ 3500 Å (Sect. 3.5.a).

We might note, that equilibrium potential and film thickness are so closely related, that during continuous irradiation the potential is seen to decrease when the film is eroded away.

After termination of the irradiation a delayed conductivity[86,87] might perhaps still allow for a considerable amount of charge transport, but some amount of charge has been seen to remain for hours after irradiation (see below).

ii) Electron incidence: Also keV electrons induce secondary electron emission, thus depositing positive charges at the surface. However, in this case the projectiles themselves constitute a negative charge deposition which easily cancels out the positive charge-up. In agreement herewith the target current i_t^+ remained constant during continuous irradiation (compare above).

Suppressing the secondary electrons, only negative charges are deposited by an electron beam, and the target charges up negatively. This is observed when monitoring i_t^- (Eq. 2.3), because this current will begin to fall off when the surface potential approaches the grid bias (-45 V), i.e. when the electron suppression "fails". In this case, when the surface potential exceeds the grid bias, the target current i_t^- will equal i_t^+; i.e. as long as $i_t^- > i_t^+$, the surface potential lies between 0 V and and -45 V.

Some of the considerations above should then also apply to electron incidence, but unlike the case for ions we do expect the deposited charges to be distributed in depth after slowing-down. For 2 keV electrons incident on D_2-films the surface potential was seen to reach $\sim$ -45 V for $x_o \cong$ 8000 Å, while the projectile range[1] is $\sim$ 5800 Å.

iii) Stable charges: Negative charges were deposited in films of $\sim$ 10000 Å D_2 by bombardment with 2 keV electrons. Afterwards, the

target was heated (Sect. 2.1.i) so that the film evaporated while the target current i_o^+ was monitored. Since the beam is turned off (i_b = 0) we might expect also i_o^+ to be zero, except that negative charges still remaining in the film would also escape during evaporation. Thus a kind of "delayed secondary emission" would cause i_o^+ to increase above zero (Fig. 2.7). This emission apparently occurs in two "bursts", one at the beginning of the evaporation and the other somewhat later. One possible interpretation is that the deposited charges are concentrated at the surface and at some finite depth (projectile range?).

The same behaviour was observed even when waiting half an hour or more between irradiation and evaporation, indicating that some amount of charges remain stable for a long time within a film. Correspondingly, the surface potential of a 2 μm D_2-film has been observed[77] to remain near or below -45 V for a longer period of time.
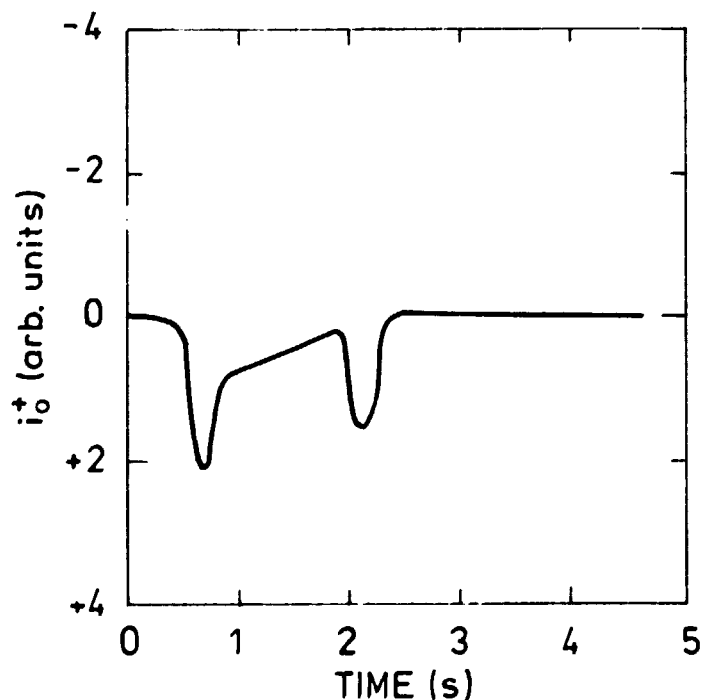

Fig. 2.7. Target current i_o^+ vs. time during evaporation of 10^4 Å D_2, after irradiation. The current varies because of release of charges previously deposited by 2 keV electrons. Note direction of ordinate-axis.

3. STOPPING IN SOLID H_2, D_2, AND N_2

The stopping in condensed gases may be evaluated a) theoretically, b) from the stopping in vapours, and c) by direct or indirect measurements on the targets in question.

The many uncertainties involved in direct measurements with keV light ions in solid H_2, D_2, and N_2 makes it preferable to extract our knowledge from a combination of the three approaches.

Very few experimental data are available for light ions below 10 keV in gaseous H_2, D_2, and N_2 (Sect. 3.1). Furthermore, it is difficult to predict whether or not we should expect any kind of phase effect at these energies (Sect. 3.2).

The present experiments are based on two different principles (Sect. 3.3): The projectile range is measured by a kind of "mirror-substrate" method, and the stopping cross section is measured by backscattering.

Both methods are based on many assumptions, some of which are investigated and discussed in Sec. 3.4.

Fortunately the two methods have rather few assumptions in common, so that the mutual agreement of the results (Sect. 3.5) is an indication of the validity. For solid H_2 and D_2 we generally[2] find very good agreement with vapour-data and theory, whereas[3,4] there is strong evidence that the electronic stopping cross section in solid N_2 is only half as large as that in the gas.

For incidence of electrons it is argued, on the basis of previous measurements, that Bethe's stopping cross section applies very well (Sect. 3.6). Apparently in this case there is no phase effect in the stopping.

3.1. Stopping in gases

For the purpose of later comparison we shall first try to establish some values for the ranges and the stopping cross sections in gaseous H_2, D_2 and N_2.

i) Ranges: The only available range measurements in H_2 and N_2 below 10 keV are the "ionization extrapolated ranges" (IER) of Cook et al.[88] The IER[89] is a concept somewhat similar to our range, R_L (see Sect. 3.4.iv):

A beam of protons is passed through a gas cell and into a charge collector. For a constant beam intensity the "ionization current" i is measured as a function of target thickness τ. The steepest tangent to the resulting, decreasing, $i(\tau)$-curve is then extrapolated to zero current, and the intercept defined as the IER.

It is not obvious precisely how the IER is related to the projected range R_p, but it appears from Fig. 3.13 and 3.17 that the IER (broken line) is in quite good agreement with the R_p (dotted line) calculated[90] from the theoretical stopping cross sections of Lindhard et al.[20,23] for both H_2- and N_2-targets.

ii) Stopping cross sections: Phillips[91] measured the stopping cross section in 9 different gases by passing a proton beam through a gas absorption chamber limited by thin foils. The resulting energy distribution was determined with a decelerator by measuring the beam current as a function of retarding voltage. The ion-optical difficulties inherent in strong retardation (see Sect. 2.5) and the energy loss (5-10 keV) in the foils add to the experimental uncertainties.

Values for H_2-gas at 7 and 10 keV are ~ 12% lower than the theoretical electronic stopping cross section of Lindhard and Scharff[20] (Eq. 1.7). No other experimental data are available at the present low energies, but we remember that Eq. 1.7 gave good agreement also with the IER-data (above), despite the reservations mentioned in Sec. 1.1.

For N_2-gas also two newer sets[92,93] of experimental data are
found, showing quite different energy dependences but agreeing
within ~ 20% at 5 keV. Both sets of measurements are made with
electrostatic analysers and differentially pumped targets. Only
the measurements of Dose and Sele[93] extend to energies below
5 keV, and major disagreement is reported with values obtained
by differentiation of the IER of Cook et al.[88]. However, it may
easily be demonstrated that this comparison is invalid without
path length corrections: Projected ranges R_p calculated from
Winterbon's tables[90] assuming the electronic stopping cross
section of Dose and Sele[93] actually agree very well with the
ranges of Cook et al.[88], i.e. the two sets of measurements sup-
port each other. S_e-values of Phillips[91] at 8 and 12.4 keV are
only ~ 8% higher than those of Dose and Sele, while Eq. 1.7
gives values that are ~ 3% lower. The semi-empirical S_e-curve
of Andersen and Ziegler[19] is ~ 7% higher than that of Dose and
Sele[93].

3.2. Phase effects

Ever since Swann[94] first suggested a possible variation of
stopping cross section with material density people have been
concerned with the possible influence of phase effects on the
energy loss of heavy charged particles. Nevertheless the picture
is still rather confusing.

Fermi[95] estimated that at very high energies solids should have
perhaps 50% lower stopping than gases due to "polarization
screening", an effect that would be negligible at low energies.

One of the most significant differences between various phases
is that the electric interaction between distant particles in
condensed matter will raise the outer shell excitation
levels[28,96,97] so that one should expect lower stopping. Cal-
culations[98] using solid-state wave functions in the formalism
of Lindhard and Winther[99] suggest a few per cent difference
for He^+-ions near the stopping cross section maximum.

Various surveys[67,100,101] of published stopping data attempt to describe systematic differences between various phases, but in most experiments phase effects could not be distinguished from effects of chemical binding, and disagreements are considerable[67,100]. It is suggested[100,102] that phase effects should generally be largest for the low-Z elements where a major part of the electrons are outershell electrons, reaching 20-40% near the stopping cross section maximum[67,100], but the extension to lower energies is not clear.

A few experimental results exist for low-energy stopping in H_2O and D_2O: Stopping cross sections for 10-100 keV protons and deuterons in H_2O and D_2O ice[103-105] are consistently 10-20% lower than those in water vapour[91,106], whereas Matteson et al.[107] report a ~ 12% difference for 300 keV He^+, increasing with decreasing energy.

One may not very easily extrapolate these results to our experiments. For one thing we are concerned with still lower energies, and furthermore it is important to distinguish between several classes of condensed phases according to electronic structure, as these may show varying degrees of phase effects upon excitation levels[97]. We note here that the target materials used in this work (H_2, D_2, and N_2) are all homonuclear diatomic molecules with closed-shell structure, bound together by Van der Waals forces. One may thus perhaps make qualitative comparisons between these targets, but not necessarily with H_2O in which the structural modifications by condensation are caused mainly by the presence of the hydrogen bond[108].

Let us then consider our direct measurements on solid H_2, D_2, and N_2 with 0.3 - 10 keV/amu ions. In the following section the principles of both range- and stopping cross section measurements are described, ignoring for now the problems and limitations involved. These are then investigated and discussed in Sect. 3.4.

3.3. Principles of measurement

The energy spectra of light particles reflected from a heavy substrate might be expected to have well-defined "front edges" corresponding to scattering from the surface. For hydrogen beams incident onto Xe or Au these front edges should approach the incident energies: A single backscattering collision gives an elastic energy loss of less than 3% and plural scattering may
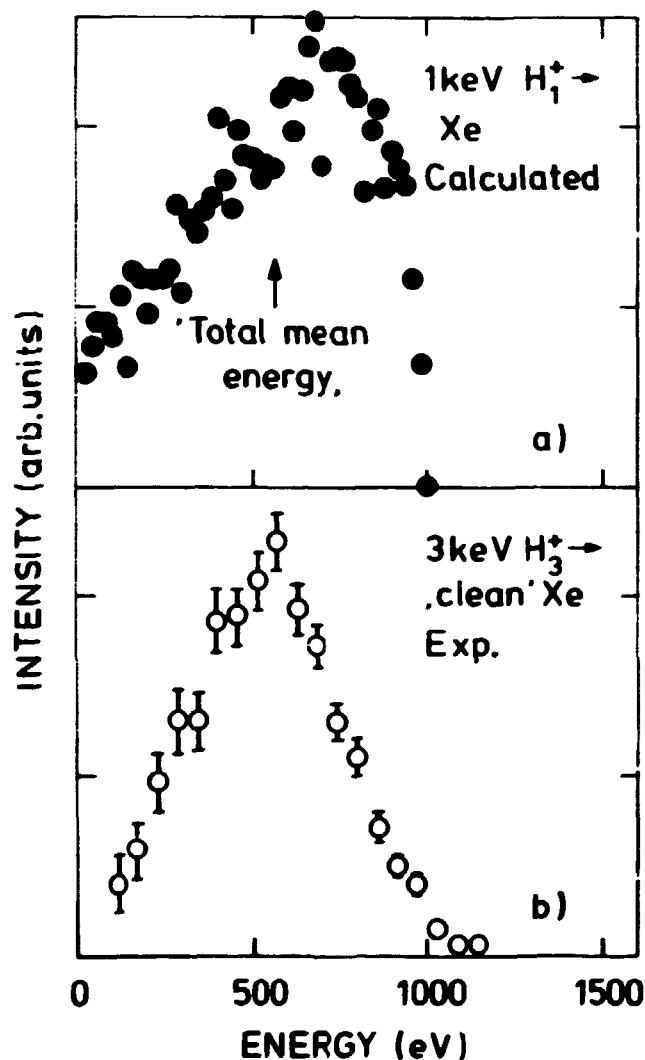

Fig. 3.1. a) 1 keV H_1^+ → Xe. energy distribution of reflected projectiles emitted at angle β =45°. Calculated by means of the Monte Carlo computer program TRIM[109].

b) 1 keV/amu H_3^+ → Xe, experimental spectrum of positive emitted particles at β =45°.

give even less. Fig. 3.1a) shows an example calculated by Monte Carlo simulation[109] corresponding to detection at an angle β = 45° to the surface (Fig. 3.2). The spectrum summed over all exit angles looks essentially the same.

Consider the spectrum detected at the angle β: A film of thickness ΔX on the substrate (Fig. 3.2) will cause the spectrum to be shifted to lower energies. A beam of primary energy E_{in} will lose the energy ΔE_{in} in the film before reaching the substrate with energy

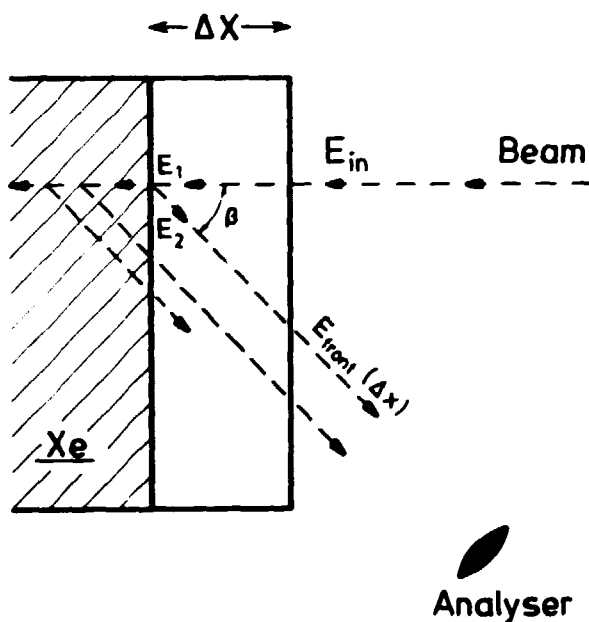$$E_1(\Delta X) = E_{in} - \Delta E_{in} \tag{3.1}$$

Fig. 3.2. Experimental principle. Beam incident on film (thickness Δx) on heavy substrate (Xe). Primary energy $E_1(\Delta x) = E_{in} - \Delta E_{in}$. Maximum reflected energy $E_2 \approx E_1$. Maximum exit energy $E_{front}(\Delta x) = E_2 - \Delta E_{out}$, depends on detection angle β.

Of course ΔE_{in} depends on ΔX. Projectiles reflected at the substrate surface will still suffer very little elastic energy loss: The maximum energy E_2 of the reflected beam approaches E_1 ($E_2 = K \cdot E_1$, where $K \approx 1$). Particles with this outward energy at the substrate again lose the energy ΔE_{out} in the film, reaching the film surface with exit energy

$$E_{front}(\Delta X, \beta) = E_2 - \Delta E_{out} \tag{3.2}$$

Here ΔE_{out} depends on $\Delta X/\cos\beta$. For large ΔX the particles reflected from the substrate do not have sufficient energy to reach the film surface ("E_{front} ($\Delta X,\beta$) < 0").

The probability of reflection from the film is small.

For now we disregard the question of charge state, pretending that all exiting particles are positive. The above picture may then be exploited in two quite different ways:

a. For various ΔX we measure the positive emission coefficient $\gamma(\Delta X)$, defined as the ratio of emitted to incident current. The probability for reflected particles to escape through the film is a decreasing function of film thickness (see later). Thus, $\gamma(\Delta X)$ decreases until the thickness $\Delta x = L^+$ where the reflected ions have just sufficient energy to reach the film surface along the shortest path ($\beta = 0^O$), i.e. $E_{front}(L^+,0^O) \approx 0$. It is suggested that the projected range R_p is closely related to $2L^+$.

b. For a thin film we determine the maximum energy E_{front} detected at $\beta = 45^O$, corresponding to particles penetrating the film along straight paths and reflected through 135° at the substrate surface. For $E_2 = K \cdot E_1$ in Fig. 3.2 we then have, from Eqs. 3.1 and 3.2,

$$E_{front}(\Delta X) = E_{front}(0) - (K \cdot \Delta E_{in} + \Delta E_{out}) \qquad (3.3)$$

since $E_{front}(0) = K \cdot E$. For thin films the stopping cross section $S(E) \equiv dE/dX$ does not vary much along the path, and we may let

$$\Delta E_{in} \approx S(E_{in}) \cdot \Delta X \qquad (3.4)$$

and

$$\Delta E_{out} \approx S(E_{front}) \cdot \Delta X/\cos\beta \qquad (3.5)$$

For an appropriate energy E between E_{in} and E_{front} we then have

$$E_{front}(\Delta X) = E_{front}(0) - S(\bar{E}) \cdot \Delta X \{K + 1/\cos\beta\} \qquad (3.6)$$

Even including the energy dependence of $S(E)$, E_{front} would still vary essentially linearly with ΔX for reasonably thin films. As E approaches E_{in} for $\Delta X \to 0$ we may then obtain an estimate of $S(E_{in})$ from the slope of the linear part of the E_{front} (ΔX)-curve.

This is a well-known[104,110] technique at MeV-energies, but the validity of the assumptions at the present low energies is far from obvious.

The problems involved with the above two principles are considered in a later section.

3.4. Investigation and discussion

Because of the many assumptions made, both of a technical/experimental and a basic physical nature, a thorough investigation and discussion of the individual phenomena is essential to the later evaluation of our results.

We shall start i) with an attempt to link the shape and behaviour of the experimental energy spectra to theoretical predictions. Explanations are suggested for the observed discrepancies.

This leads right on to ii) a consideration of the use of molecular ions. The molecules may be expected to dissociate, and further behave as an assembly of atoms with an energy distribution in the laboratory frame of reference. It is argued, that "cluster effects" may result in errors of no more than 6-8% in the backscattering measurements.

An investigation iii) of the characteristics of the $\gamma(\Delta X)$-curve indicates that the structure in the curve is probably caused by projectiles penetrating the target twice, i.e. is characteristic of the projectile range R_L.

It is noted iv) that R_L is somewhat similar to, but still different from, the "ionization extrapolated range" measured in gaseous targets.

The backscattering method is discussed v) in somewhat less detail, but it is argued that a break-down of the assumptions must cause the measured energy E_{front} to deviate from a linear dependence on target thickness. The method is seen to be limited to energies near 1.5 keV/atom and among the major experimental difficulties is the maintaining of a stable beam during a longer period of time.

The quality of the films vi) is of most importance for the backscattering method, and one of the major limitations hereof.

i) Energy spectra: Fig. 3.1a) shows a spectrum of particles reflected from a target of solid Xe and exiting at an angle $\beta = 45^{\circ}$ to the surface (Fig. 3.2). The spectrum was calculated by Monte Carlo simulation with the computer code TRIM[109] for normal incidence of 10^5 protons of energy 1 keV, and does not distinguish between different charge-states of the exiting particles. The program is based on binary collisions and the Moliere[111] interatomic potential, and has been found[112] to reproduce spectra for 8 keV protons incident on Au very nicely. Despite the statistical fluctuations we easily identify a sharp front edge in the spectrum.

In comparing with experimental spectra we run into a couple of technical problems. For instance, until now we have disregarded the complication that we detect only positive particles. There is no doubt that many of the emitted particles are neutral and thus undetected. The positive fraction of the emitted particles is largely unknown, but it is expected to increase with exit-energy[113], or actually with the component of the exit-velocity

perpendicular to the surface[114]. Over some part of the energy range it is even likely to increase very strongly[115], but unfortunately we do not know over which part this occurs. The assumption of a positive fraction which increases faster than linearly with exit-energy would actually help explain independent measurements of positive emission coefficients (see Sect. 6.1).

For "clean" Xe the positive fraction is very small, and at such low energies sufficient beam intensities could only be obtained with H_3^+- and D_3^+-ions at such low energies. Fig. 3.1[b)] shows an experimental spectrum for 3 keV H_3^+ incident on bulk Xe. Most of the molecules are expected[116] to dissociate before or during collision and be emitted as H_1^+ or H_1^0 with energies near or below 1 keV, i.e. the beam should behave essentially as 1 keV protons. This kind of assumption is rather common[117,118]. Undissociated molecules would result in signals extending up to 3 keV, whereas H_2^+-ions would be reflected with energies up to 2 keV. No signals could be distinguished above the noise level at energies above 1.2 keV.

The observation of H_1^+-ions with energies up to ~ 1.07 keV (Fig. 3.1[b)]) is in good agreement with experiments of Heiland et al.[116], and is apparently explained by the release of excess energy during dissociation (see below).

The shape of the experimental spectrum (Fig.3.1[b)]) disagrees quite significantly with that of the calculated one (Fig. 3.1[b)]. This may not be explained by the energy dependence of the positive fraction (see above) but a couple of other factors may be important. We note, that the mean energies of the two spectra agree very well, so that only the shapes disagree.

Experimentally, the energy spread due to dissociation (see below) is likely to cause some smearing of sharp features, including the front edge in Fig. 3.1[a)], but this effect alone may hardly explain the discrepancy. Another possibility is that the Moliere potential assumed in the computer program overestimates the true interatomic potential[27,112]. It has been shown[112] that the potential has a significant influence on the shape of the energy

spectra, and the examples shown in Ref. 112 suggest that a more realistic (lower[27]) potential would, in fact, distort the calculated spectrum to a better agreement with Fig. 3.1[b)].

An N_2-film on the substrate was found to strongly enhance the positive fraction. As expected the energy spectra are shifted to lower energies with increasing f:'m thickness ΔX (Fig. 3.3). until we reach the "bulk" signal. Even for bulk targets (Fig. 3.3[c)]), do we observe positive particles of reasonably high energy, in agreement with the assumption of reflection by multiple scattering in the N_2. It would appear that actually a large part of the emitted positive particles are reflected projectiles - we compare the shape of the spectrum with the expected average energy of ~ 350 eV for reflected projectiles.

The same general behaviour is observed for hydrogen films (Fig. 3.4) except that here the signal peaks near 100 eV. The peak is smaller for bulk targets than for thinner films, and the position is less sensitive to the beam energy than was the case for N_2-targets. For hydrogen targets the dominant part of the signal may be interpreted as caused by sputtered target particles, if the positive fraction increases strongly with exit-energy (see Sect. 6.1).

Probably many emitted particles will have energies below ~ 50 eV, but if so they apparently are all neutral and thus undetected (Figs. 3.3 and 3.4).

ii) Molecular ions: In many experiments[117,118] with hydrogen projectiles molecular ions have been used to achieve higher current densities at lower incident energies per proton, assuming the ions to dissociate immediately upon impact under equal sharing of the energy. This, of course, is an approximation which needs justification in the particular case: For a dissociating H_2^+-molecule there will be some repulsive energy Q acting between the atoms (protons) in the center-of-mass system (CMS), which in the laboratory system contributes a kinetic energy excess $\Delta E = \pm \sqrt{E_o Q} \cos\theta$. Here E_o is the incident (molecular) energy, and θ is the CMS-angle between the molecular velocity and the inter-
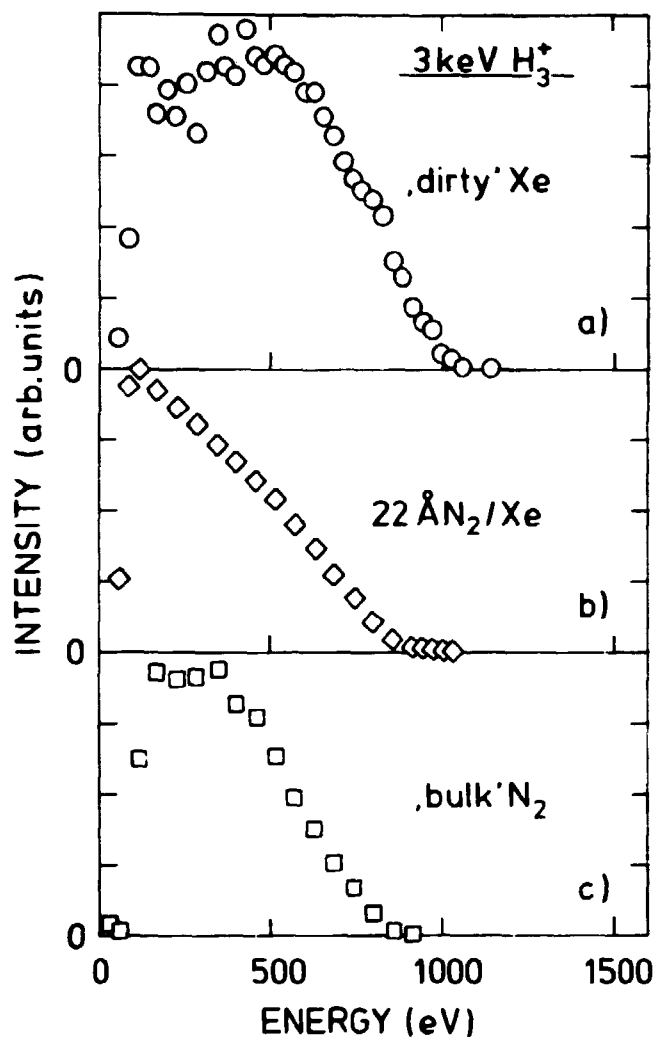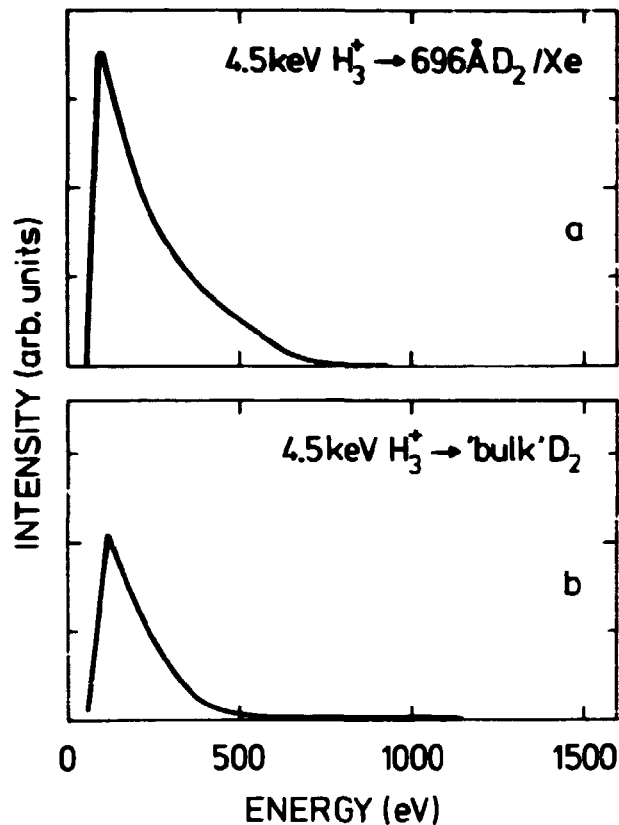
Fig. 3.3. Experimental energy distributions of positive
particles emitted at $\beta = 45°$ for 1 keV/amu H_3^+ incident on
a) ~ 0 Å N_2/Xe
b) 22 Å N_2/Xe
c) "bulk" N_2.

nuclear axis. If the dissociation was caused by Coulomt repulsion
after loss of the electron, a 2 keV H_2^+-ion would result in
protons with energies distributed between 835 and 1165 eV. For
0.2-2 keV H_2^+ions incident on Ni(111) and W(100) surfaces
Heiland et al.[116] find electron pick-up to be the most likely
process. They suggest that the incoming ion is neutralized 2-3 Å
above the surface, and if the electron is picked up into an anti-
bonding excited state the molecule falls apart independently of

Fig. 3.4. Experimental energy distributions of positive particles emitted at $\beta = 45°$ for 1.5 keV/amu H_3^+ incident on
a) 696 Å D_2/Xe
b) "bulk" D_2.

further scattering, else subsequent collisions will provide opportunity for electronic, vibrational and rotational excitation, which may lead to dissociation. Among their observations we may note (remembering the quite different target materials used): For incidence of H_2^+-ions the yield of reflected H_2^+-ions is only a few per cent of the yield of H_1^+-ions, i.e. most of the molecules do indeed dissociate (see above). The H_1^+-peak is shifted towards higher energies than the peak resulting from an H_1^+-beam of the same incident velocity. Although this shift is very small at FWHM, the maximum H_1^+-energy detected is over 100 eV higher for a 1.2 keV H_2^+-beam than for a 0.6 keV H_1^+-beam!

The precise treatment of an H_3^+-molecule is slightly more com-
plicated, but the above considerations suggest that we may
indeed explain the observed "excess" energies (Fig. 3.1[b)]) as
some effect of the repulsion between particles during dis-
sociation. As demonstrated below (3.4.v) we may simply consider
a molecular beam as an assembly of atoms, some of which have a
higher than average energy.

Another problem connected with the use of molecular ions, even
if they do dissociate immediately upon impact, is the possibility
of "cluster effects" on the energy loss. Such effects were first
reported in measurements[119-121] on the protons from dissociated
H_2^+- and H_3^+-molecules, showing larger energy loss for protons
travelling in clusters. This has been interpreted[122-125] in terms
of interference effects in the excitation of target electrons,
varying with internuclear distance, and thus with dwell time
inside the target. Interference calculations[125] for 25 keV/amu
dissociated H_2^+-molecules penetrating carbon foils suggest that
the energy loss is larger or smaller than that for individual
protons depending on the orientation of the internuclear axis.
The observed[119-124] larger average energy loss then results from
an averaging over this orientation.

Here we should be careful: We shall essentially be concerned with
the largest reflected energies (see Sect. 3.4.v), and thus per-
haps put larger weight on those molecules which are aligned with
the beam ($\theta = 0$, see above). According to Levi-Setti et al.[125],
proton clusters aligned with the beam suffer considerably smaller
energy loss than single protons until the internuclear distance
is somewhat larger than that of the original molecules. This is
unlikely to play a major role in our range measurements where
the particles shall be widely separated early in the path, but
for our thin-film measurements the effect might be relatively
larger. Fortunately, since we are concerned with backscattering
measurements (v), cluster effects may not exist for more than
~ 40% of the path (along the inward part, before the scattering).
Using the values of Levi-Setti et al. for H_2^+ in C we thus esti-
mate that the energy loss measured by backscattering might be
too small by no more than 6-8%. For the range measurements (iii)
the effect is probably much smaller.

iii) $\gamma(\Delta x)$: The "positive emission coefficient" γ (def. in Eq. 2.!) is measured as a function of film thickness ΔX. An example is shown in Fig. 3.5 for D_2-films on Au.

In the following, characteristics of the $\gamma(\Delta x)$-curve are investigated in order to ascertain that we interpret the curve correctly (Sect. 3.3.a), i.e. that we may indeed determine from this a range $R_L \simeq 2L^+$.
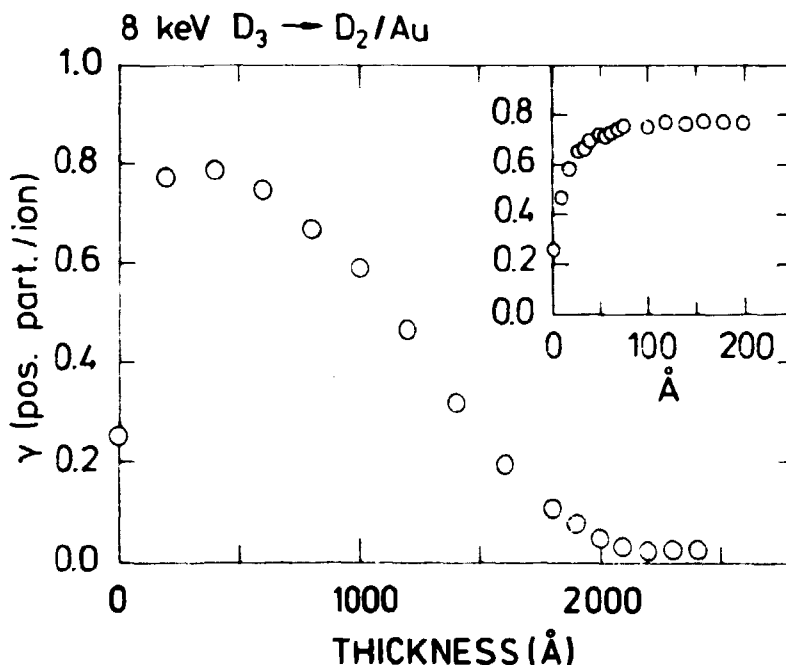

Fig. 3.5. Positive emission coefficient γ (eq. 2.1b) vs. film thickness Δx, for 8 keV $D_3^+ \rightarrow D_2/Au$.

For thick targets, $\gamma(\Delta x)$ is seen to be independent of film thickness Δx. The behaviour of this "bulk" coefficient is investigated and discussed in Sect. 6.1. Apparently, the bulk yield for H_2 and D_2 may be explained by sputtered particles. As expected, it is independent of the substrate.

For smaller film thicknesses, γ varies with Δx in a quite significant way (Fig. 3.5), which we have suggested is directly related to reflection from the substrate. This assumption was checked by replacing our usual Au-substrate with one of carbon.
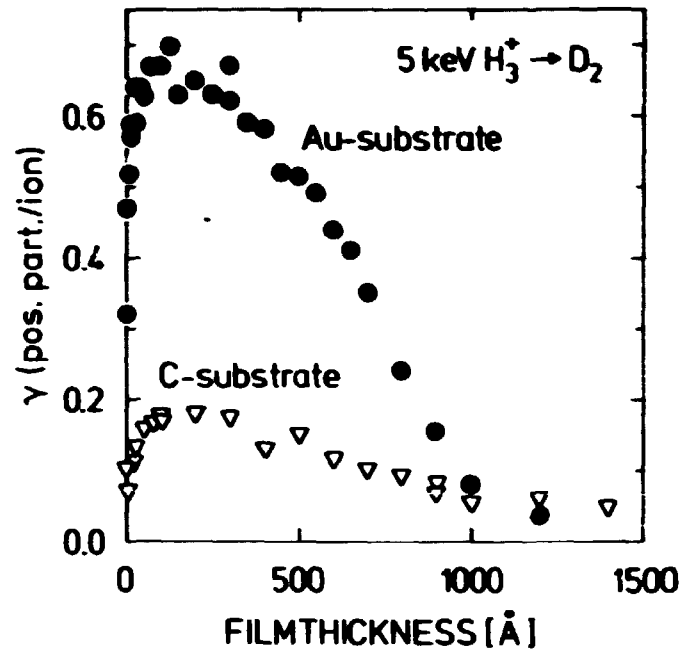
Fig. 3.6. γ(Δx) for 5 keV H₃⁺ → D₂ on Au-substrate (●) and C-substrate (▽).

Thereby, the peak was strongly reduced (Fig. 3.6) in agreement with reflection coefficient data[126] for hydrogens, and we suggest three mechanisms as possible origins of the peak in the γ(Δx)-curve (Fig. 3.7):

1) Projectiles are reflected from the substrate and escape,
2) on the way out they sputter target particles, and
3) recoiling target particles or collision cascades are reflected from the substrate.

In using the term "sputtering" we do not intend to imply any specific mechanism for producing recoils.

Mechanism 1) is obviously somehow related to the penetration dept. We shall argue that so is mechanism 2) whereas mechanism 3) is negligible for the present projectile-target combinations:

Considering mechanisms 2) and 3) together, we are dealing with a phenomenon somewhat analogous to transmission sputtering. Esti-
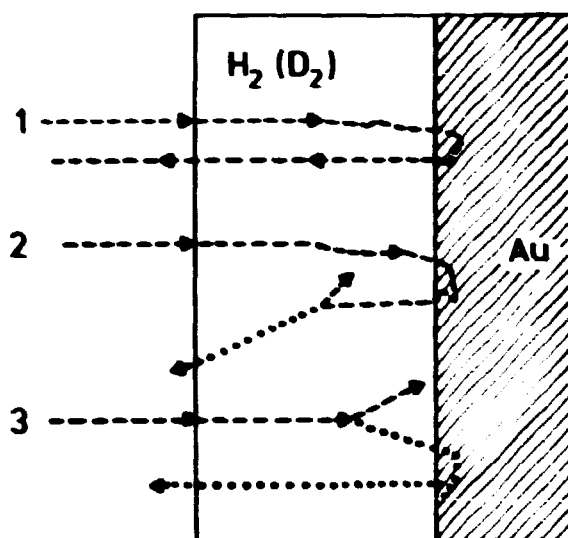
Fig. 3.7. Possible positive emission mechanisms involving reflection on Au.
1) Reflected projectiles
2) Sputtering by reflected projectiles
3) Recoils or collision cascades reflected on Au.

mates within ordinary sputtering theory[29] (linear collision cascades) show clearly that the corresponding yield would originate essentially from the immediate exit-surface region of the film, i.e. mechanism 3) is unimportant. In order to test this argument, we compare the results for 8 keV D_3^+-ions incident on H_2-, D_2- and N_2-films (Fig. 3.8). Due to the relatively short ranges of the recoiling nitrogen in N_2, mechanism 3) is expected to contribute very little here. The observation that the peak is just as high for N_2- as for D_2-targets supports the assumption that mechanism 3) is negligible in all cases, unless for some reason the positive fraction is simply much higher for sputtered nitrogen.

Estimating the relative importance of mechanisms 1) and 2) is somewhat difficult because the emitted energy spectra to be expected from mechanism 2) probably depend on the specific mechanism for producing recoils. Comparing results for hydrogen and deuterium ions in the same targets we found that the maximum γ-value was typically $\gtrsim$ 30% larger for D_3^+-beams.

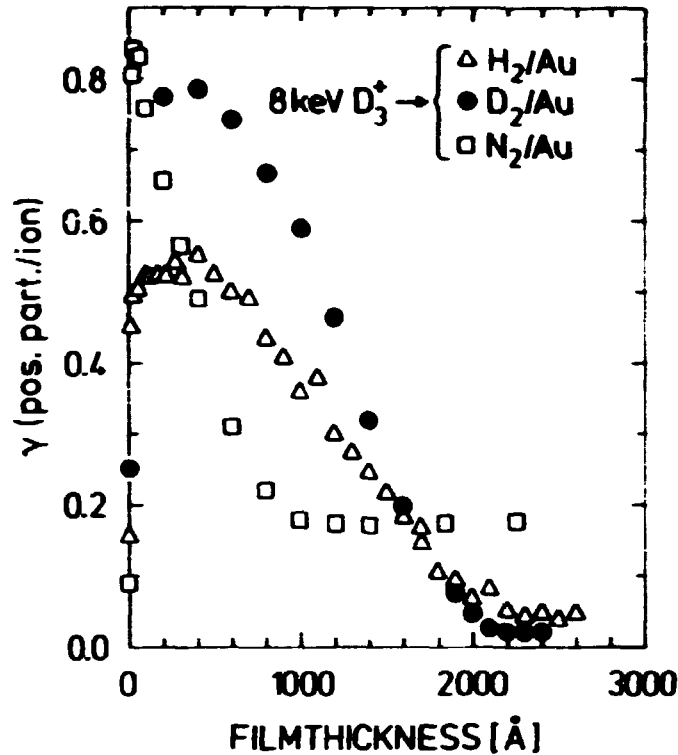This might suggest that the emitted species depends on the beam rather than on the target.

Fig. 3.8. γ(Δx) for 8 keV D₃⁺ incident on H₂/Au (Δ), D₂/Au (●) and N₂/Au ( ).

Measurements in gases[127] suggest that the observed difference would not result from mechanism 2). Also the positive fraction of a beam after passing through H_2- or N_2-gas was found[128] to be larger for D- than for H-beams in the 100 eV range and below.

However, gas data for the charged fraction may not be applicable to solids, where the surface energy barrier is likely to be important.

In view of the above we find it very unlikely that mechanism 3) has a measurable influence on our results, and it seems reasonable to assume that emitted recoils originate close to the surface.

Qualitatively, either of the mechanisms 1) and 2) may explain the peak in γ(ΔX). For the sake of illustration consider the yield of positive reflected projectiles (mech. 1)) as a function of film thickness ΔX.

The reflected projectiles will leave the substrate at all possible angles, and the probability of escape through the film will depend on the angle as well as the energy of each particle. Clearly this probability decreases with increasing ΔX up to half the range of the beam, as mentioned earlier.

The resulting decrease in $\gamma(\Delta X)$ is further enhanced by the behaviour of the positive fraction.

The charged fractions of the emitted particles are usually believed to be determined by excitations in the last few monolayers of the target[129] or even partly outside the surface[114]. For ΔX large enough that the projectiles lose a measurable amount of energy in the film, the charged fractions are apparently independent of the substrate[130]. For not too small ΔX we therefore assume the positive fraction to depend only on exit energy (actually on velocity perpendicular to the surface[114]). The positive fraction is generally expected to increase exit-energy (see also above), and it was seen that the energy spectra are shifted towards lower energies with increasing ΔX.

So we do indeed expect γ to be a decreasing function of ΔX. The only exception occurs at very small ΔX: The positive fraction of the particles emitted from a clean metal surface is very small[130], and for very small ΔX it should then increase strongly with "contamination".

So in summary, mechanism 1) should result in a peak in $\gamma(\Delta X)$ extending up to the film thickness above which beam particles may no longer traverse the film twice and escape as positive ions (i.e. with energy above 50 eV).

iv) Range R_L: We define, and measure, the "threshold thickness" L^+ (see Sect. 3.3.a) as the intercept of the bulk level and the steepest tangent of negative slope for the $\gamma(\Delta X)$-curve (Fig. 3.9).

It appears from the discussion above, that beam particles will lose almost all their energy in penetrating the "range" $R_L = 2L^+$. As mentioned in Sect. 3.1, R_L is a concept somewhat similar to
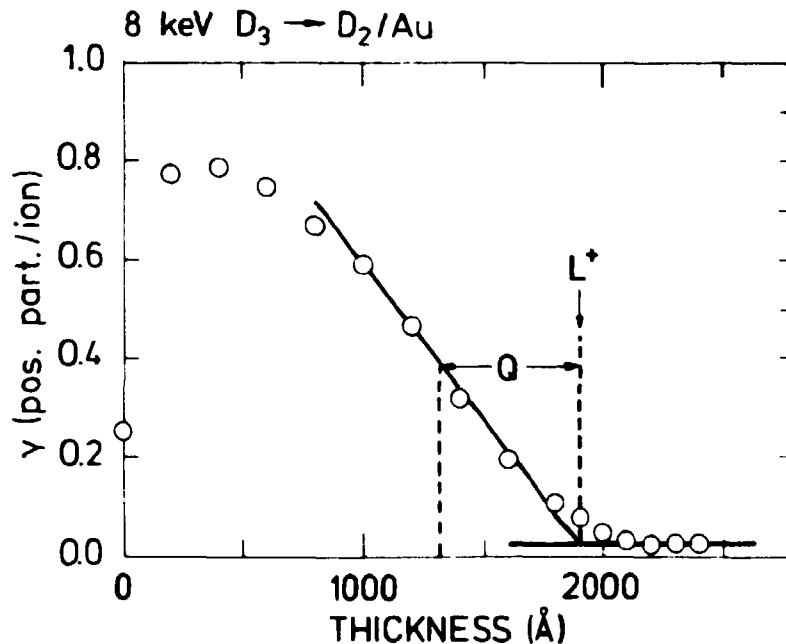
Fig. 3.9. As Fig. 3.5. L^+ is intercept of bulk level and the steepest tangent of negative slope. $Q = L^+ - \Delta X(1/2\gamma_{max})$ (see later).

the IER of Cook et al.[88], but two basic differences should be noted:

(1) the scattering on the substrate results in an additional energy and angular distribution, and

(2) the exit through a solid-vacuum interface may be expected[114] to strongly influence the charge states of the emitted particles.

Nevertheless, we shall see that for H_2-targets the results agree very well (Fig. 3.13).

The uncertainties in the energy scale are negligible (Sect. 2.2), whereas many factors contribute to those in L^+: The uncertainty in the $\gamma(\Delta X)$-curve was in each case estimated from the reproducibility of the curve. Together with uncertainties in the data analysis this led to confidence limits of 5-10%. Combined with the uncertainty in absolute film thickness (Sect. 2.1) this gives estimated errors of 10-15% in L^+.

v) Backscattering: In the usual applications of the back-scattering principle[104,110] the average energy loss for projectiles scattered from the substrate surface is evaluated from the position of the half-height point of the front edge of the energy spectrum. Because of the shape of the energy spectra (Figs. 3.1[b]) and 3.4) our "front edges" are not as well-defined as expected (Fig. 3.1[a]). Instead we measure the maximum energy $E_{front}(\Delta X)$ of each spectrum, defined as the intercept of the front of the peak and the high energy noise level. Fig. 3.10 shows 2 examples of "front edges": The maximum reflected energies are estimated as $E_{front}(54 \text{ Å}) \simeq 992 \pm 6$ eV and $E_{front}(105 \text{ Å}) \simeq 945 \pm 5$ eV. Signals of higher energy simply constitute the noise level. Error bars indicate counting statistics (see below).

We suggest now that $E_{front}(\Delta X)$ gives us the minimum energy loss for passage in and out through the film, and is determined mainly by the stopping cross section. Let us briefly consider some possible competing mechanisms:

Particles may undergo scattering in the film before or after reflection from the Xe, but this will generally result in longer paths, additional energy loss and thus energies lower than $E_{front}(\Delta X)$. The same is obviously the case for particles reflected from behind the Xe-surface.

However, particles undergoing plural or multiple scattering in the film may be reflected a total of 135° without ever reaching the Xe, and thus possibly lose less energy along the path. This might then result in a detected energy larger than the $E_{front}(\Delta X)$ of Eq. 3.6. But this energy cannot exceed the maximum energy from the "bulk" target (Figs. 3.3[c] and 3.4[b]), which means that it does not decrease with increasing ΔX. This effect is therefore easily recognized, but defines an upper limit for the applicable ΔX.

Straggling effects are likely to influence the detected energies, leading to smaller minimum energy losses ΔE_{in} and ΔE_{out} than given by the stopping cross section (Eqs. 3.4 and 3.5). This would give a clearly non-linear thickness dependence of E_{front}.
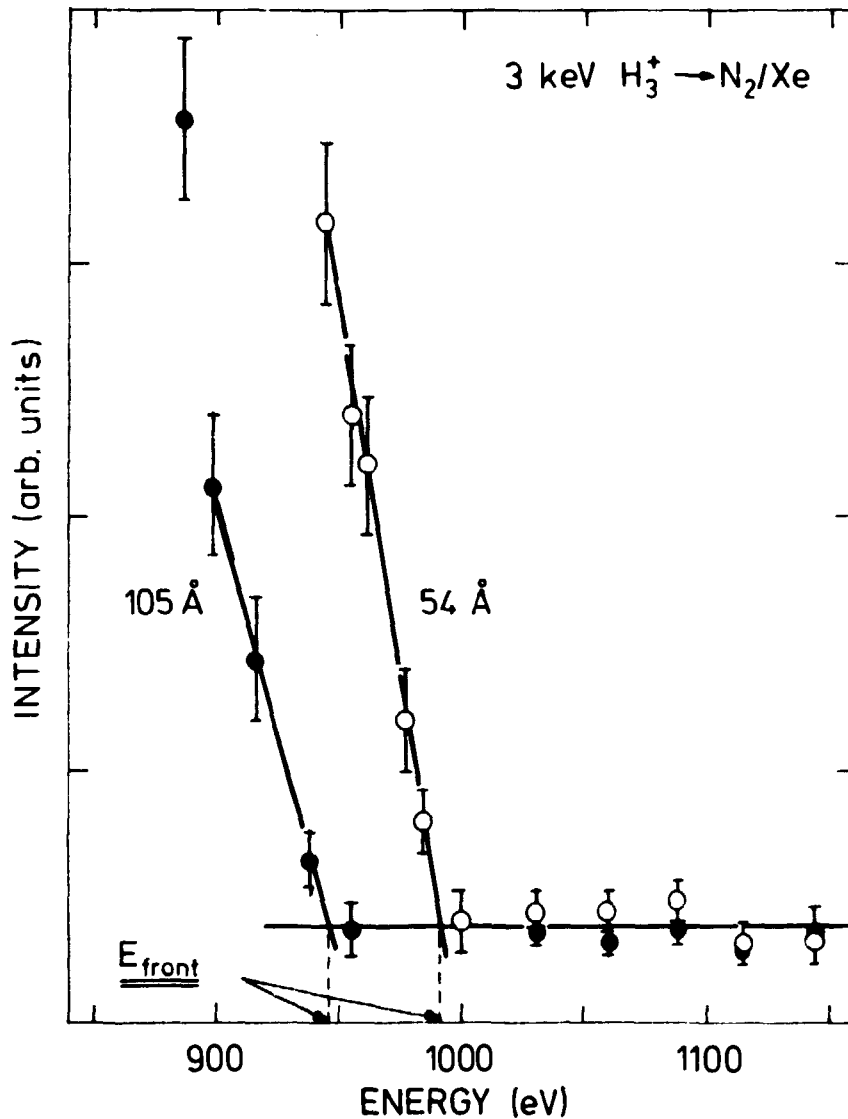
Fig. 3.10. 1 keV/amu H_3^+-ions incident on 54 Å N_2/Xe and 105 Å N_2/Xe. Experimental energy distributions (high energy part) of positive particles emitted at $\beta = 45°$. E_{front} is energy of intersection between signal and noise level. Error bars indicate counting statistics.

Finally, we expect $E_{front}(\Delta X)$ to be non-linear for thicknesses so small that the beam does not reach charge equilibrium. For the sake of estimate we consider 1.5 keV protons incident on solid N_2 and take the charge-exchange cross sections as $\sigma_{10} \sim 6 \cdot 10^{-16}$ cm^2 [131] and $\sigma_{01} \sim 10^{-16}$ cm^2 [132]. From this we expect charge equilibrium after penetration of ~ 25 Å.
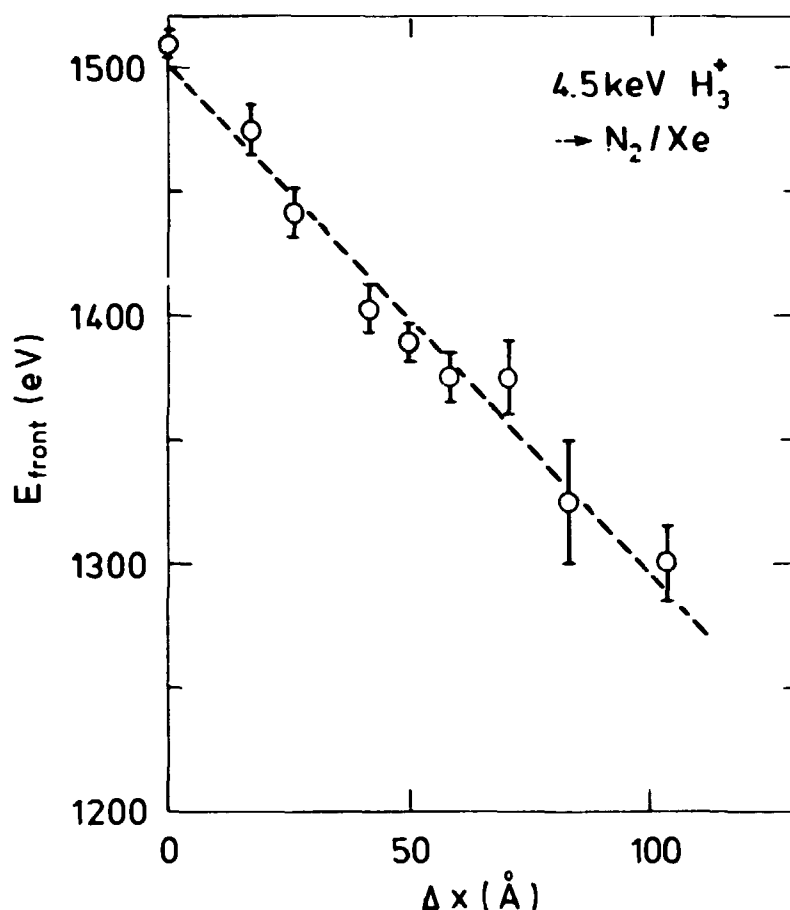
Fig. 3.11. Maximum reflected energy, E_{front}, vs. film thickness ΔX for 1.5 keV/atom $H_3^+ \rightarrow N_2/Xe$. Also best straight line through E_{front} (ΔX).

Any of the above effects would cause E_{front} to deviate from a linear dependence on ΔX, so the linearity of a plot of E_{front} vs. ΔX provides an indication of the validity of the assumptions behind Eq. 3.6. As shown in Figs. 3.11 and 3.12 the maximum reflected energy was indeed observed to vary linearly with ΔX for sufficiently thin films (in the present cases for energy losses up to 10%). For larger ΔX (> 350 Å in Fig. 3.12) the energy approached a constant ("bulk") level. By means of Eq. 3.6 we determine the stopping cross section $S(E_{in})$ from the "linear region", although with uncertainties of the order of 20%.

The "linear region" of course depended on primary beam energy, and below ~ 1 keV/atom it became prohibitively small. On the
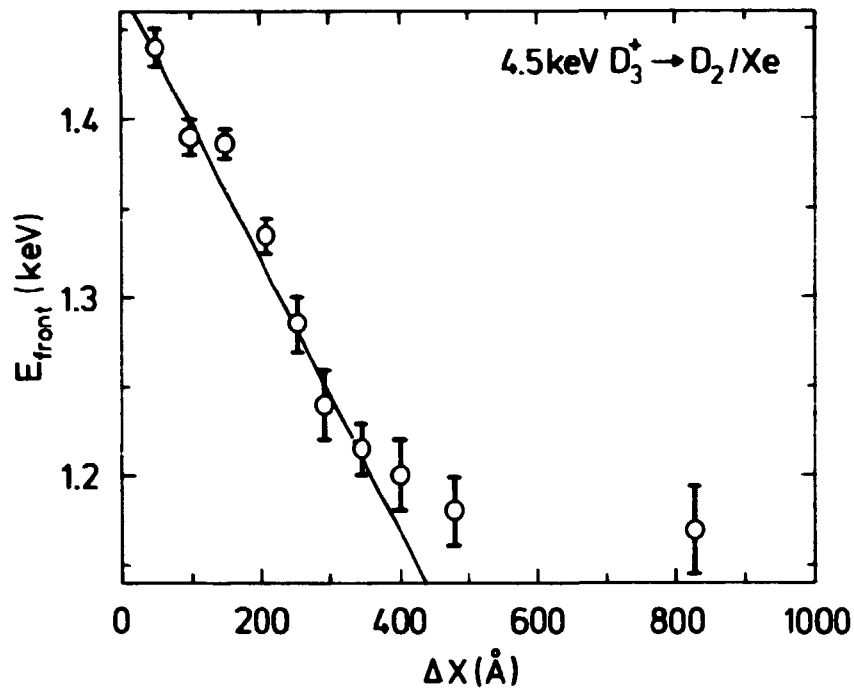
Fig. 3.12. Maximum reflected energy, E_{front}, vs. film thickness ΔX at $\beta = 45°$ for 1.5 keV/atom $D_3^+ \to D_2/Xe$. Also best straight line through $E_{front}(\Delta X)$-points for $\Delta X < 350$ Å.

other hand, we were limited towards higher energies by the decreasing reflected intensities (see below).

At these low energies the stability of the beam during a longer period of time (namely, while collecting an entire spectrum) proved to be one of the most critical requirements. We therefore preferred to work with H_3^+- and D_3^+-ions, assuming these would dissociate immediately upon impact.

It was suggested above (3.4.ii) that we may simply consider such a molecular beam as an assembly of atoms, some of which have a higher than average energy. In order to investigate this, measurements were also made with H_1^+- and H_2^+-beams at a few energies. The resulting $E_{front}(\Delta X)$-curves for a given energy were all essentially parallel, but with no "extra" energy for H_1^+.

vi) Films: Deterioration (erosion) of the film during irradiation proved to be a major limitation for the measurement of energy

spectra (3.4.v). As shown in Sect. 6.6.3, thin films of D_2 are eroded with yields of the order of 10^3 D_2-molecules per incident ion. For thin H_2-films the corresponding yields ($> 10^4$ H_2 per ion) are directly prohibitive, whereas N_2-films erode somewhat slower than D_2-films.

Each film was therefore irradiated with a series of very short pulses, and the corresponding yields checked for systematic effects. In order to obtain sufficient statistics, each point of an energy spectrum is obtained as the sum of the yields from several independent films. Unfortunately, we are concerned primarily with that part of the spectrum where the front of the peak falls off to the noise level (see 3.4.v), i.e. we are looking for small count rates. Thus, one of the spectra in Fig. 3.10 is already the result of irradiating at least 50-60 films. As the reflected intensities decrease rapidly with increasing primary energy, we are strongly limited to low energies ($\lesssim$ 1.5 keV/atom for D_2, $\lesssim$ 2 keV/atom for N_2) with this method.

As the erosion yields for H_3^+-ions incident on thin hydrogen films are considerably larger than for D_3^+-ions (Sect. 6.6.3), the spectra obtained with H_3^+ show considerably poorer statistics. As furthermore the "region of linearity" is somewhat smaller than for D_3^+-ions, the corresponding stopping cross sections are not nearly as accurately determined.

Erosion problems are easily avoided in the measurement of ranges, since γ-values are determined with 0.5 mS pulses.

A possible microcrystalline structure of the films is expected to affect mainly the width of the range distribution, whereas R_p should remain reasonably unchanged[133].

3.5. Results and discussion

a. The results of the range measurements are shown as $R_L = 2$ L^+ (see Sect. 3.4.iv) vs. incident energy per mass unit in Figs. 3.13-3.18:
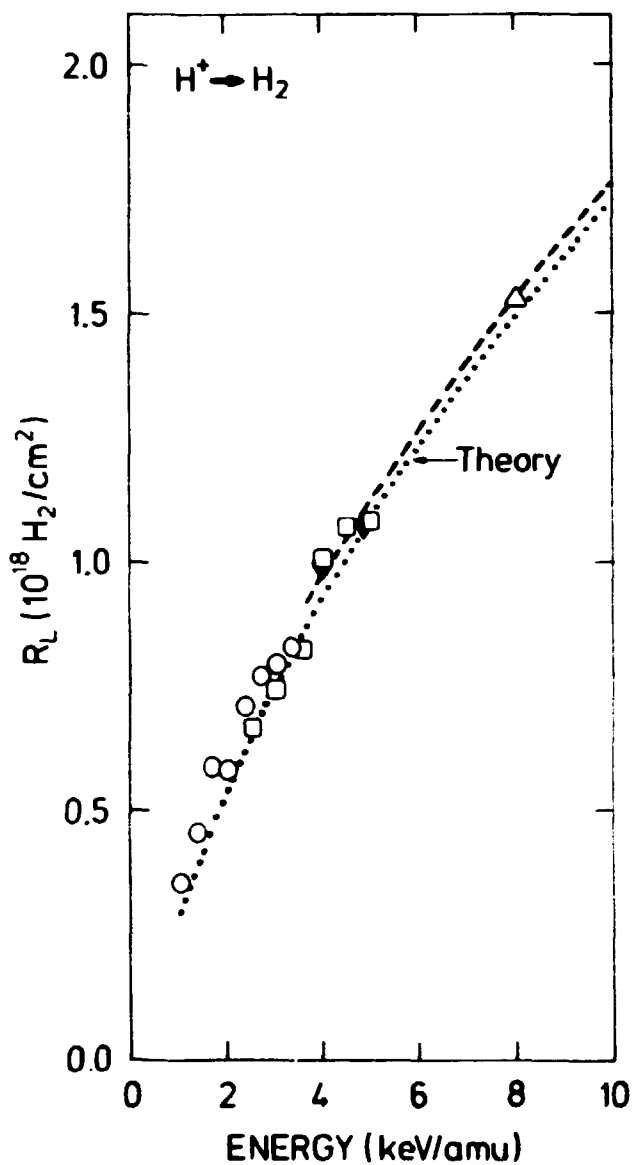
Fig. 3.13. Range of hydrogen ions in H_2. Present results (R_L) for solid H_2 with H_3^+-(o), H_2^+-( ), and H_1^+-(Δ) beams. Experimental results[88] for gaseous H_2: Low energy points (∇) and fit for 4-37.5 keV (broken curve). Theoretical R_p[90] assuming Lindhard-stopping (dotted curve).

In agreement with the discussion of Sect. 3.4.ii we find no significant difference between values obtained with different H-molecules (Figs. 3.13 and 3.14).
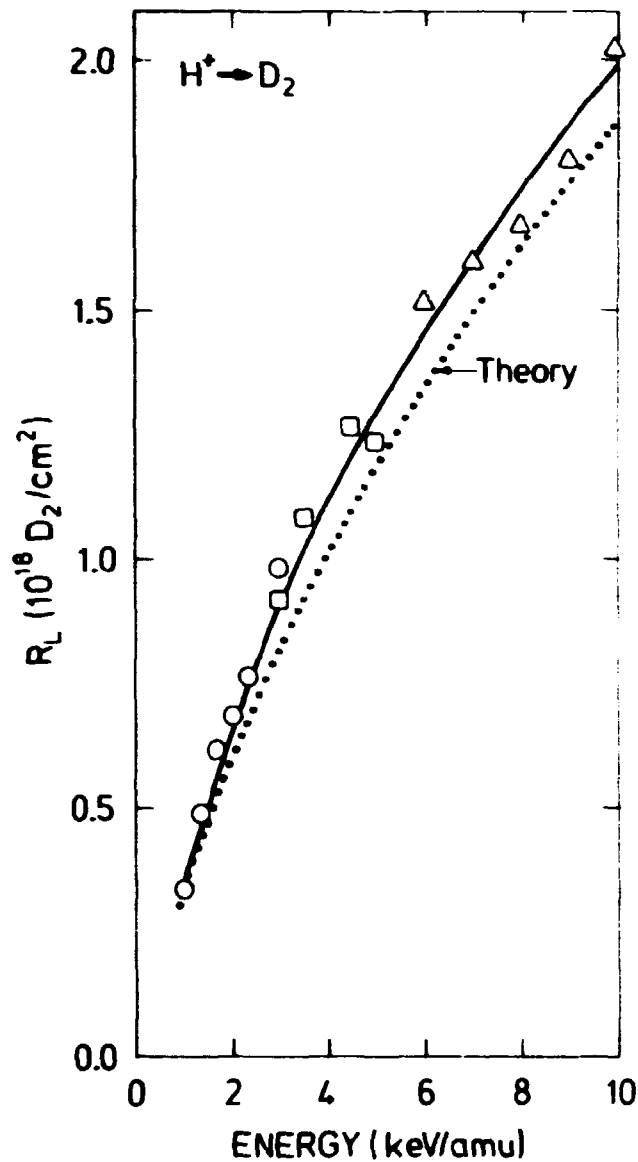
Fig. 3.14. Range of hydrogen ions in D_2. Present (R_L) for solid D_2 with H_3^+-(o), H_2^+-( ), and H_1^+-($\triangle$) beams. Theoretical R_p^{90} fitted to R_L by varying S_e (solid curve). Theoretical R_p^{90} assuming Lindhard-stopping (dotted curve).

The ranges are larger in D_2 than in H_2, in qualitative agreement with the difference in nuclear stopping.

For solid H_2 (Fig. 3.13) the R_L-values agree very well with the "ionization extrapolated ranges" (IER, see Sect. 3.1.i) of Cook et al.[88] for H_2-gas, in spite of the inherent differences between the range concepts (Sect. 3.4.iv).
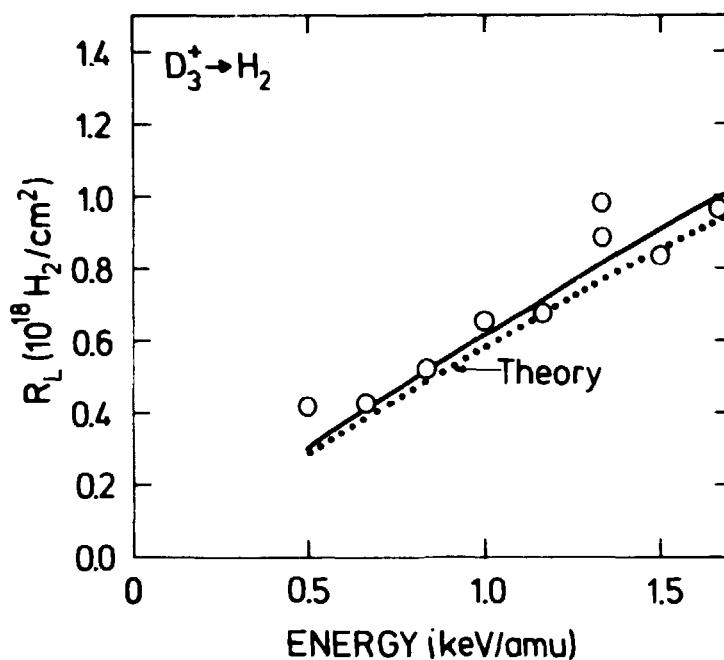
Fig. 3.15. Range of deuterium ions in H_2. Present results (R_L) for solid H_2 with D_3^+-(o) beams. Theoretical R_p^{90} fitted to R_L by varying S_e (solid curve). Theoretical R_p^{90} assuming Lindhard-stopping (dotted curve).
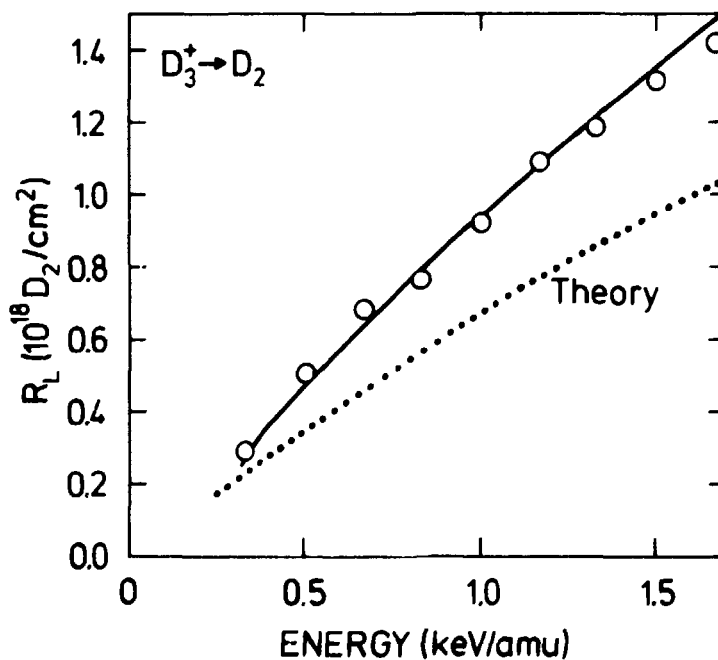

Fig. 3.16. Range of deuterium ions in D_2. Present results (R_L) for solid D_2 with D_3^+-(o) beams. Theoretical R_p^{90} assuming Lindhard-stopping (dotted curve).

In general, our R_L-values for hydrogen targets agree reasonably well with the projected ranges R_p calculated[90] from Eqs. 1.7 and 1.14, except for deuterium ions in D_2 (Fig. 3.16). For deuterium ions in H_2 the points scatter relatively much (Fig. 3.15).

An attempt was made to estimate the effect of energy loss straggling on the range distribution by numerical integration of an energy straggling composed of an electronic and a nuclear term. For the straggling in the electronic energy loss we used the expression of Lindhard and Scharff[134], while the straggling in nuclear energy loss was calculated directly from the interaction cross section[23]. Correlation effects were neglected. The resulting range straggling varied between 10 and 40% of the range in our energy region, i.e. quite substantial.

The effects of the range straggling are expected to include a smearing of the $\gamma(\Delta X)$-curve, reducing the extrapolated slope and possibly influencing the extrapolation (Fig. 3.9) itself. In analogy to Langley[135] we therefore define a relative "range straggling factor" Q/L^+, where Q is the difference between L^+ and the film thickness at which γ has fallen to half its maximum (see Fig. 3.9). The values thus determined scatter strongly due to the quality of the data (Fig. 3.19), but they generally decrease with increasing energy, in agreement with theory. The theoretical curves show the full widths at half maximum of the calculated range distributions divided by the corresponding average ranges.

It should be emphasized that the measured "range straggling factors" may give only qualitative information. For instance, due to the reflection process at the substrate, Q/L^+ would have a finite value even if there was no range straggling involved (compare Fig. 3.1). However, we do observe systematic differences between the straggling factors corresponding to the same incident velocities: Q/L^+ for the same ion is larger in H_2- than in D_2-targets, and in the same target it is larger for hydrogen than for deuterium ions. It seems fair to assume that this reflects differences in the actual range straggling, but whether

it is related, somehow, to the various degrees of agreement between R_L and R_p is not quite obvious.

We note here that the agreement between R_L and theory is better in H_2 than in D_2-targets, and that theory seems to underestimate R_L most for the smallest Q/L^+. If indeed the range straggling caused an error in R_L, one might have expected the opposite relation!

Below, we shall compare our ranges to measured stopping cross sections, but for now we simply note that for three out of four projectile-target combinations in solid hydrogens we seem to agree with theory and gas-measurements within ~ 10%.

For solid N_2, however, our R_L-values (o) are about 50% higher than the R_p (dotted curve) calculated[90] from Eqs. 1.7 and 1.14 (see Figs. 3.17 and 3.18). This discrepancy may not be explained by errors in the theory for N_2-gas: We recall that for protons in N_2-gas, theory was well supported by both range-[88] and stopping cross section[91,93] measurements (see Sect. 3.1 and Fig. 3.17). In principle, of course, the different range concepts might lead to quite different results despite the agreement observed for hydrogen targets. On the other hand, our values for solid N_2 are supported both by stopping cross section measurements (below) and secondary electron emission coefficients (Sect. 4.4.iii).

It might be of interest to note that the theory of Lindhard and Scharff[20] works well for a neighbouring solid (carbon): Projected ranges R_p of 10-30 keV deuterons in C were measured[136] by means of the $D(^3He,\alpha)H$ nuclear reaction[137] and found to agree well with ranges calculated on the basis of Eq. 1.7. However, we recall (Sect. 3.2) that it may be important to distinguish between various classes of materials.

b. The stopping cross sections were also measured "directly" by backscattering, but for the reasons mentioned above (Sects. 3.5.v and 3.5.vi) this was possible only in a few selected cases.
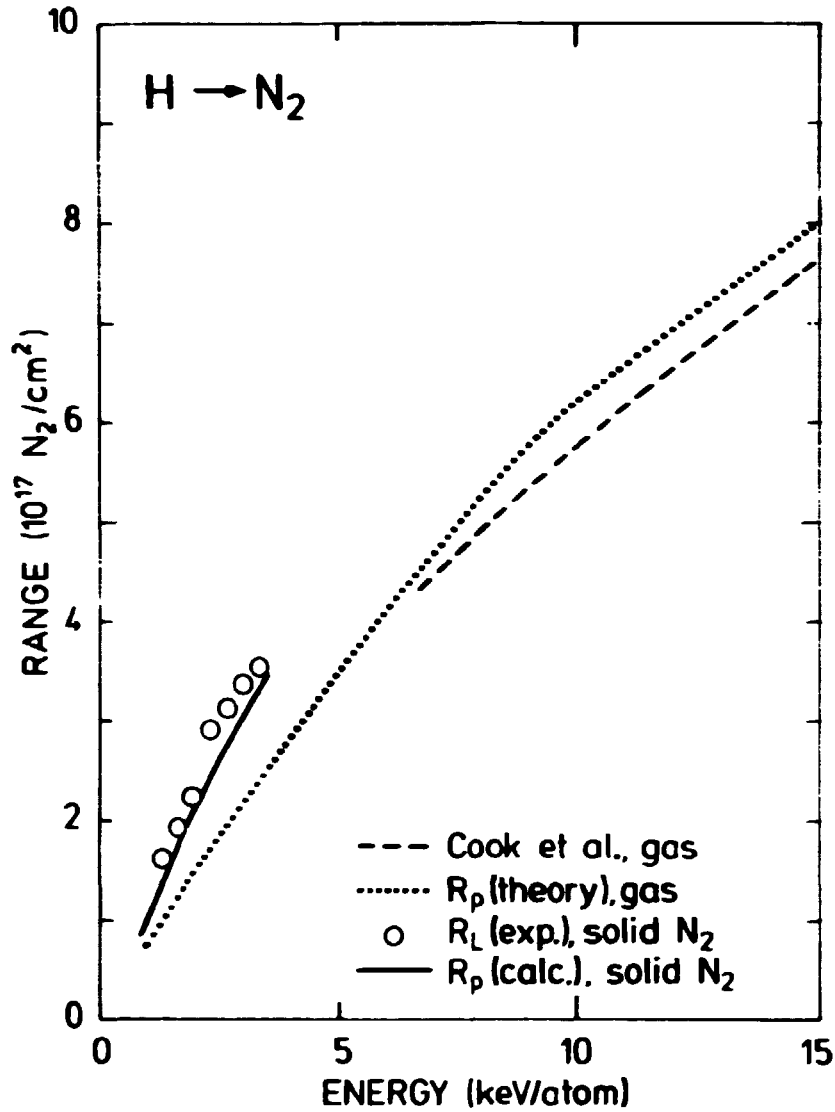
Fig. 3.17. Range of hydrogen ions in N_2. Present results (R_L) for solid N_2 with H_3^+-(o) beams. theoretical R_p[90] for solid N_2 assuming experimental S_e of present work (solid curve) (see later). Experimental results[88] for gaseous N_2 (broken curve). Theoretical R_p[90] assuming Lindhard-stopping (dotted curve).
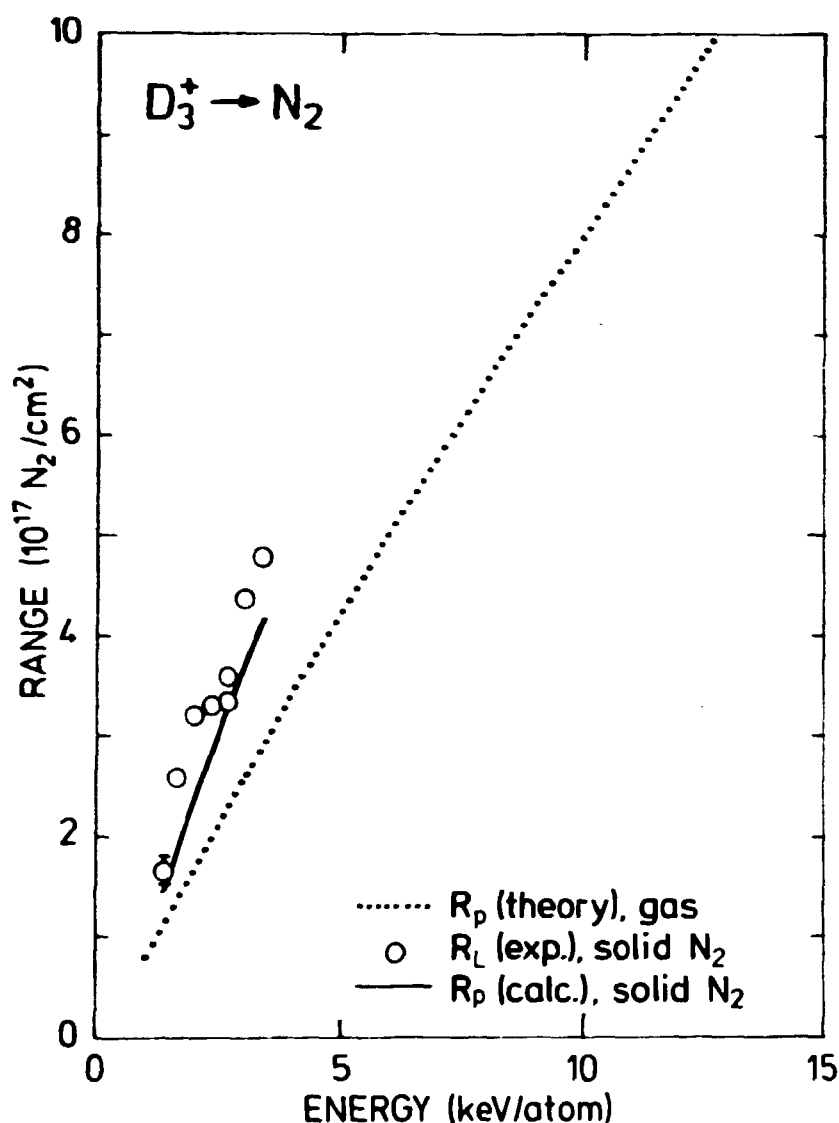
Fig. 3.18. Range of deuterium ions in N_2. Present results (R_L) for solid N_2 with D_3^+-(o) beams. theoretical R_p^{90} for solid N_2 assuming experimental S_e of present work (solid curve), see later. Theoretical R_p^{90} assuming Lindhard-stopping (dotted curve).

Figure 3.20 shows results for H_1^+-, H_2^+-, and H_3^+-ions incident on solid N_2, extracted by means of Eq. 3.6. The rather large error bars are estimated from statistical uncertainties and re-producibility, and indicate the quality of the H_3^+-values. Due to the much greater difficulties involved in maintaining good H_1^+- and H_2^+-beams, the corresponding uncertainties for these are even larger.

RANGE STRAGGLING FACTORS
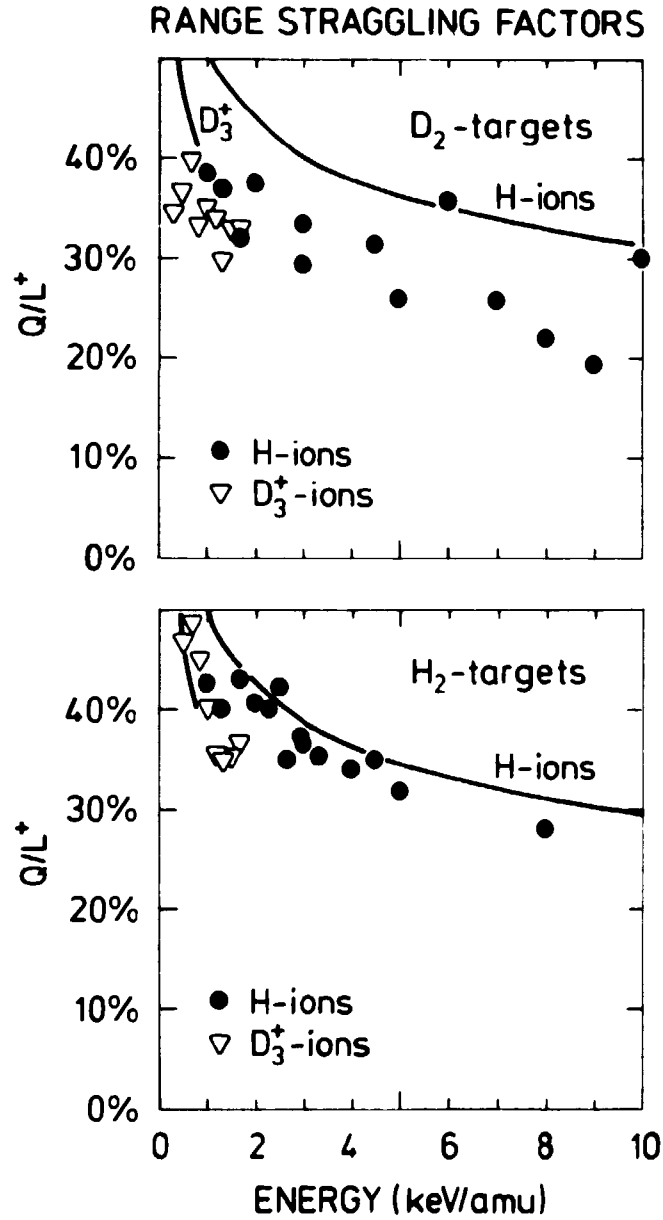
Fig. 3.19. "Range straggling factor", Q/L^+, versus incident energy for H- (●) and D-ions (∇) in solid D_2 and H_2. Curves are calculated from electronic and nuclear energy loss straggling.

In agreement with the discussion of Sect. 3.4.ii (and 3.5.a) we find no significant difference between values obtained with the different H-molecules. We recall that "cluster effects" were expected to result in lower S_e-values for molecular beams.
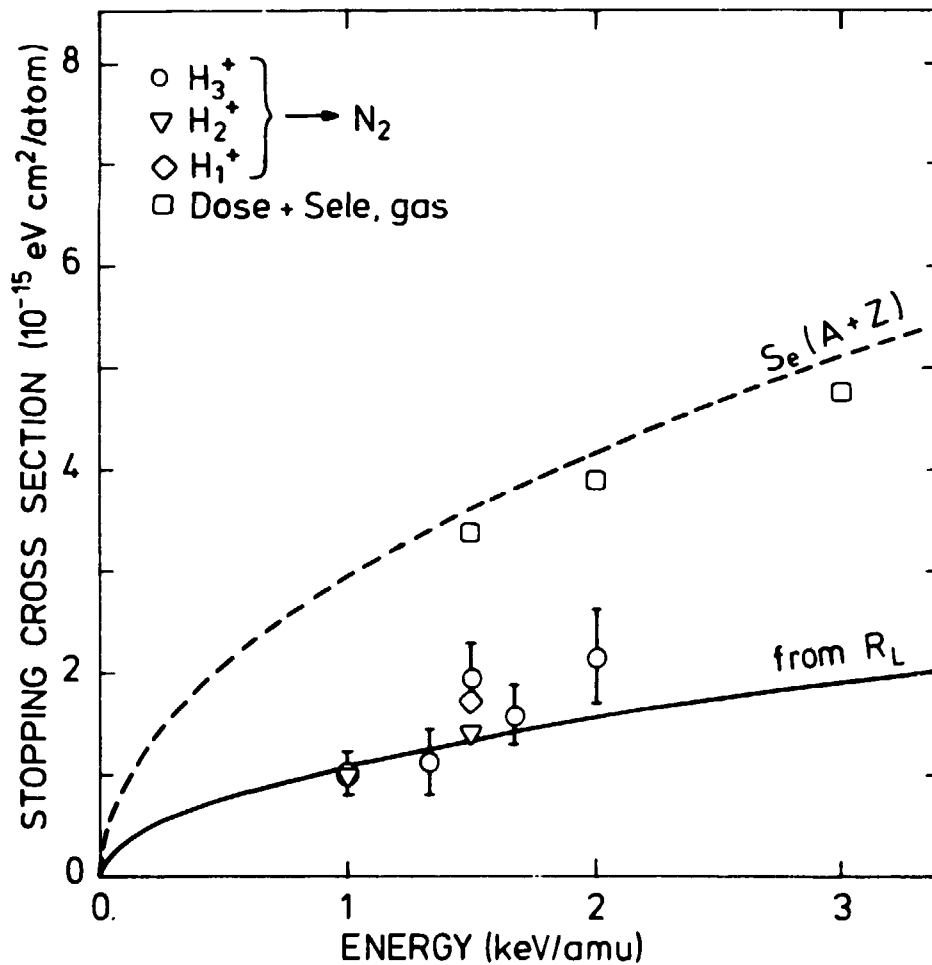
Fig. 3.20. Stopping cross section vs. energy for hydrogen ions in N_2. Present results for solid N_2 with H_1^+-(□), H_2^+-($\triangledown$) and H_3^+(o) beams. S_e for solid N_2 (solid curve) obtained by fitting Rp to exp. ranges R_L. Experimental results[93] for gaseous N_2(□). Semi-empirical[19] S_e (broken curve).

Apparently, the stopping cross section is approximately proportional to the energy, but the energy range is much too small to determine the energy dependence.

Figure 3.20 also includes the experimental values for N_2-gas of Dose and Sele[93], and the semiempirical S_e-curve of Andersen and Ziegler[19] (see Sect. 3.1.ii). Our results are seen to be 40-60% lower than these, a difference larger than the combined uncertainties.

In searching for systematic errors in this comparison, we might suggest that in using quite different experimental methods we also account differently for nuclear stopping contributions. However, the discrepancy may not be explained by different contributions from the nuclear stopping cross section S_n, which is typically 10-20% of S_e at these energies.

The effect of multiple scattering, etc., on our results is not easily estimated theoretically, since we are measuring minimum energy losses, which are not necessarily sensitive to the average multiple scattering. We thus rely mainly on the linearity of $E_{front}(\Delta X)$ (Sect. 3.4.v).

We recall that also our range measurements (Figs. 3.17 and 3.18) suggested lower stopping in solid than in gaseous N_2. In order to compare the two sets of results we calculate the projected range R_p assuming the measured S_e (actually the best velocity proportional curve through the points). As we see there is quite good agreement between the calculated R_p (solid curve) and the measured R_L (open circles).

Clearly, we might just as well have compared our stopping cross section results to the $S_e(E) = k \cdot E^{1/2}$ extracted from our measured $R_L(E)$: By means of Winterbon's tables[90] we compute $R_p(E)$-curves for various values of k. The value k_{exp} which best reproduces our $R_L(E)$-values is the determined by interpolation. We note that this procedure is based on various assumptions. Firstly, just like in the reverse comparison above, we assume that we know the nuclear stopping cross section S_n. More seriously, however, we start with defining S_e to be proportional to the velocity (Eq. 1.5), and only find the best proportionality constant k_{exp}. The resulting $S_e(E)$-curve is included in Fig. 3.20 and shows very good agreement with the measured points.

We shall see (Sect. 4.4) that based on very different assumptions we may also deduce S_e-values from secondary electron emission coefficients, and that also these agree with Fig. 3.20. Apparently, we may thus conclude that the stopping in our solid N_2-targets is indeed at least 40% lower than in gaseous N_2, whether this

is due to a "real phase effect" (Sect. 3.2) or to structure in
the target. The difference between solid and gaseous targets is
not caused by systematic errors in the measurement of target
thickness (Sect. 2.1): Our ranges, R_L, are in good agreement with
the gas-values of Cook et al.[88] for H_2 (Fig. 3.13) but in clear
disagreement for N_2, i.e. several possible systematic errors in
the two sets of measurements are excluded. Furthermore, we note
that the results of Sect. 4.4 are independent of target thick-
ness.

For hydrogen targets the backscattering method is even more un-
certain, and only applicable to D_2 (see Sect. 3.4.vi). For D_3^+-
beams of incident energies of 0.67 and 0.75 keV/amu S_e was esti-
mated to within ± 15%, but because of the greater difficulties
with H_3^+-beams the value at 1.5 keV/amu was only determined to
±25% (see Fig. 3.21).

These data are far from sufficient to calculate R_p-values from
them with any kind of certainty. For the sake of comparison we
instead extract $S_e(E)$-curves from our R_L-data by fitting computed
$R_p(E)$-curves, as described above. The best fits $R_p(k_{exp}, E)$ are
indicated in Figs. 3.14-3.16 (solid curves), but omitted in Fig.
3.13 to avoid confusion. The resulting $S_e(E)$-curves are included
in Fig. 3.21 (solid and broken curves). Within the rather large
uncertainties the three backscattering points are seen to agree
with the corresponding $S_e(E)$-curves.

As discussed in Sect. 3.1.ii our best estimate of S_e for H_2-gas
is the theory of Lindhard and Scharff[20] (Eq. 1.5). The resulting
curve (dotted curve) shows good agreement with three of the
extracted $S_e(E)$-curves, while S_e is considerably lower for deu-
terium ions in D_2. The latter deviation is a direct reflection
of the particular deviation for the ranges (Fig. 3.16). The small
difference for hydrogen ions (solid curves) between H_2- and D_2-
targets is within the experimental uncertainty. This is not the
case for deuterium ions. We note that the particularly low values
for D-ions in solid D_2 seem to be supported by the backscattering
measurements, whereas the secondary electron emission does not
show any peculiarities for D-ions incident on D_2 (Sect. 4.2.i).

Although the scatter of the corresponding R_L-points is surpris-
ingly low (Fig. 3.16), we find the data insufficient to conclude
that S_e is really so much lower in this case.

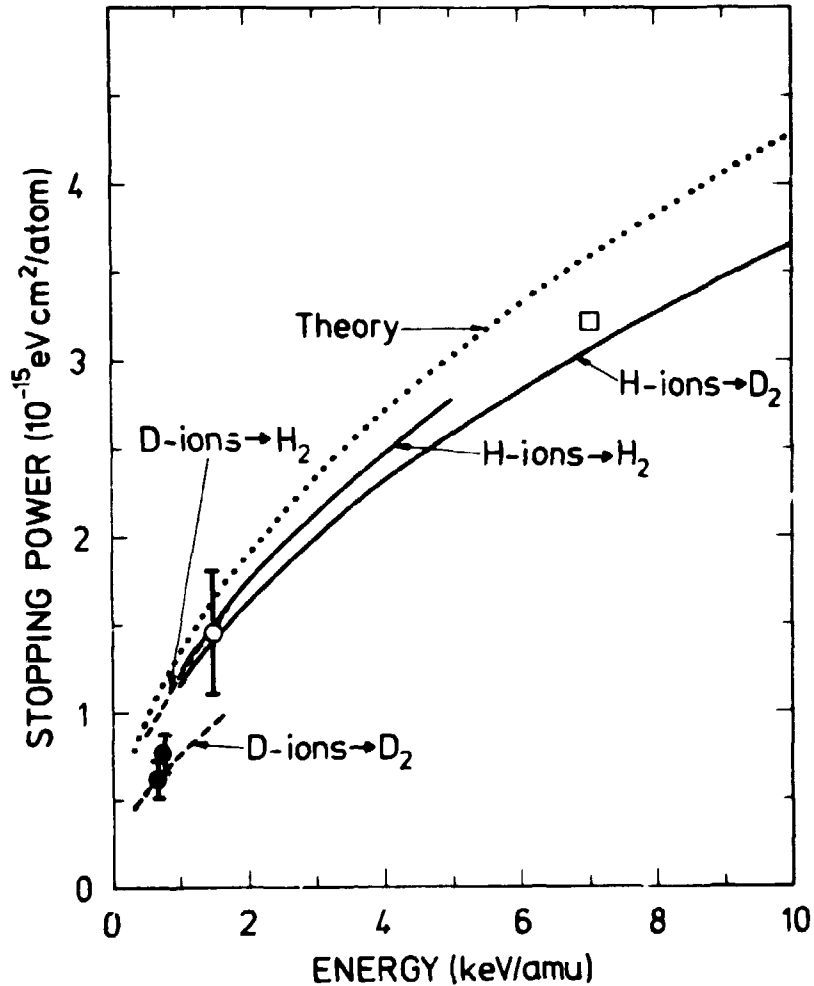Fig. 3.21. Stopping cross section vs. energy for hydrogen
and deuterium ions in H_2 and D_2. Present results obtained by
fitting R_p to exp. ranges R_1 for D_3^+-ions (broken curves)
and H-ions (solid curves) incident on solid H_2 (upper
curves) and D_2 (lower curves). Theoretical stopping cross
section of Lindhard and Scharff[20] (dotted curve). Also exp.
value of Phillips[91]($\square$).

3.6. Stopping cross sections for electrons

It has been suggested[138,139] that Bethe's stopping theory (Sect. 1.1.i) should typically be valid to within ~ 10% at energies near 1 keV, and comparisons with various other models[140-142] suggest that deviations from Eq. 1.4 do not become severe until we reach energies below ~ 100 eV.

Stopping cross section measurements are not available for the cases of interest to us, but ranges for electrons have been measured recently (see below). In the evaluation of these it becomes important to clarify which kind of range we are considering, since scattering may be appreciable (Sect. 1.1). The experimental method is described below in some detail, because it is also the basis of our erosion measurements (see Sect. 6.4).

3.6.1. The mirror method[143]

The ranges of keV electrons in solid H_2, D_2, and N_2 have previously been determined[1,11,12] by a method which is quite analogous to our range measurements for ions (Sect. 3.3.a):

A gold substrate was used as a "mirror" for an electron beam. For normal incidence of keV electrons the reflection coefficient η is of the order of 40%, and the energy distribution of the reflected electrons has its maximum slightly below the primary energy[144]. In contrast, the reflection coefficients for H_2, D_2 or N_2 are very low.

Most of the simultaneously emitted "true" secondary electrons have energies of a few eV, and it is an experimental convention[1] to simply define electrons of energy below 45 eV as secondaries (see Sect. 2.4.ii). Figure 3.22 shows measurements of the reflection coefficient η for D_2-films on a gold substrate as function of the film thickness ΔX for perpendicular incidence of 1.9 keV electrons. The coefficient is seen to fall off almost linearly as the probability for reflected electrons to escape through the film decreases with ΔX. Thus $\eta(\Delta X)$ decreases until the thickness d where the electrons that have been reflected
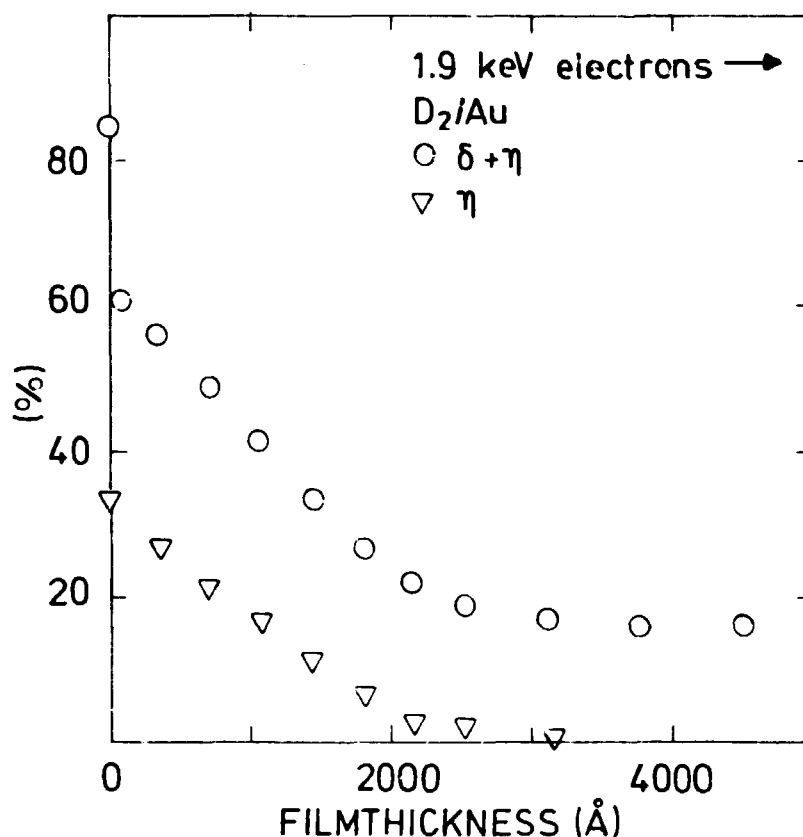
Fig. 3.22. Reflection coefficient, η, and total electron emission coefficient, η + δ, vs. film thickness for 1.9 keV electrons → D₂/Au.

from the gold surface have just sufficient energy to reach the film surface again with ~ 45 eV remaining. The projected range is taken as twice this thickness:

$$R_p(E) \approx 2d. \tag{3.7}$$

As secondary electron emission is induced by both incident and reflected electrons, also the secondary electron emission coefficient δ varies with film thickness. Figure 3.22 also shows measurements of the total electron emission (η+δ). For very thin films (ΔX < 50 Å), δ(ΔX) varies particularly strongly because secondary electrons from the gold may escape also[1]. Of course also (η+δ) may be used for range measurements.

The method for measuring η and (η+δ) is described in Sect. 2.4.1.

3.6.2. Results for electrons

It has been found that

$$R_p(E) \approx 0.53 \cdot E^{1.72} \cdot 10^{18} \text{ molecules/cm}^2 \qquad (3.8)$$

for solid H_2 and D_2[11], while

$$R_p(E) \approx 9.02 \cdot E^{1.75} \cdot 10^{16} \text{ molecules/cm}^2 \qquad (3.9)$$

for solid N_2[12]. Just like for ions (Sect. 3.5.b), it is not
straightforward to extract stopping cross sections from these
ranges, because multiple scattering is not easily accounted for.
Clearly, simple differentiation of $R_P(E)$ will lead to a "stopping
cross section" $S_R(E)$ which is too large, but since nuclear stop-
ping is negligible, S_R will converge towards $S_{e,e}$ at high
energies.

For hydrogen targets the ratio $S_R/S_{e,e}$ should be reasonably close
to unity at the present energies. Thus, the assumption of Bethe's
formula (Eq.1.4) for $S_{e,e}$ is supported by the observation[1,11] that
$S_R/S_{e,e}$ then decreases from ~ 1.13 at 0.5 keV to ~ 1.06 at 3 keV.
For N_2-targets the ratio should be larger, and indeed it is found
to decrease from ~ 1.55 at 0.5 keV to ~ 1.24 at 3 keV. Here we
may try to estimate the stopping cross section S_{N_2} better by means
of the following argument:

Grün[145] measured both a projected range, R_G, and a differential
stopping cross section, S_G, in air, i.e. a target material com-
parable to N_2. This gives a basis for estimating the importance
of multiple scattering by comparing S_G with the stopping cross
section derived from R_G by differentiation. We simply note that
R_G exceeds Eq. 3.9 by ~ 5% but shows the same energy dependence.
As then the corresponding stopping cross section[145] S_G is ~ 5%
lower than Eq. 1.4, we may conclude that our S_{N_2} is well de-
scribed by this equation.

We thus suggest, that for our targets and energies $S_{e,e}(E)$ is
described by Eq. 1.4 to within ~ 10%.

We note that the agreement between R_G (above) and Eq. 3.9 seems
to exclude the possibility of a phase effect for the stopping
of keV electrons in N_2.

4. SECONDARY ELECTRON EMISSION

This subject was discussed in detail in ref. 1, and the following is therefore mainly based hereon. The relation between electron emission and stopping theory is best illustrated by factorizations as in Sect. 4.1. Such factorizations lead to the definition of a "material parameter" Λ_{exp} to be determined experimentally. The observation that Λ_{exp} is actually a characteristic of the target material, only weakly dependent on projectile, supports the qualitative relation to stopping theory (Sect. 4.2). The agreement with previous data[1] for incidence of electrons (Sect. 4.3) further supports this, and illustrates the limitations. Finally, the relation investigated is applied to the question of stopping in solid N_2 (Sect. 4.4). The agreement with the results of Sect. 3.5 supports both the assumption of a phase dependent stopping cross section in N_2, and the theory for secondary electron emission.

4.1. Theory

A necessary condition for the validity of Eq. 1.18 is that high-energy electrons dominate the spectrum of primary excitation[146], so that cascades may develop. This assumption is not necessarily fulfilled in our cases[82] (see also Sects. 2.4.1.i and 2.4.2.i), but no better theory is available at present.

The factorization in Eq. 1.19 becomes particularly useful when recoiling target atoms do not play an essential role in the generation of secondary electrons[1]. Thus β is utilized mainly for light primary particles (electrons or protons), or for heavier particles in the energy region where $S_n(E) \ll S_e(E)$. It turns out[1] that β is a very slowly varying function of the primary energy.

Not only is the full validity of Eq. 1.18 questionable, but furthermore the present knowledge of physical quantities is insufficient[1] to allow evaluation of the material parameter Λ for solid H_2, D_2, and N_2. Instead we may prefer to define an "experimental" material parameter (see Eqs. 1.18 and 1.19)

$$\Lambda_{exp} = \Lambda \cdot \beta \cdot N \qquad (4.1)$$

to be determined experimentally as

$$\Lambda_{exp} = \delta/S_{p,e}(E) \qquad (4.2)$$

This does not depend on cascade theory.

However, the crude assumptions made[1] must be kept in mind, and measured Λ_{exp}-values are used only for qualitative estimates, etc.

4.2. Results and discussion, ions

The secondary electron emission coefficient δ (defined in Eq. 2.2) was measured as described in Sect. 2.4.1.i for normal incidence of 2-10 keV H^+, H_2^+, H_3^+, D_3^+, D_2H^+, $^4He^+$, $^{14}N^+$, and $^{20}Ne^+$ on bulk targets of solid H_2, D_2 and N_2. The coefficient is expressed as the number of emitted electrons per incident atom.

Figs. 4.1, 4.2, and 4.4 show the results as functions of the incident energy (in keV/amu).

i) Hydrogen targets: For hydrogen-ions (H_1^+, H_2^+, H_3^+ and D_3^+) the results are seen to increase almost linearly with energy (Fig. 4.1). The points for D_2H^+-ions (not shown) agree very well with these. In a previous publication[5] it was attempted to account for the simultaneous positive emission (see Sect. 2.4.1.i), but the energies of the emitted positive particles were unknown. The present results (Fig. 4.1), therefore, constitute a minor ($\lesssim$ 10%) improvement of the previous ones. The suggested[5] system-

atic differences between δ-values for different molecules are
δ-values for different molecules are still indicated, but are
weaker:

Apparently, (Fig. 4.1) the δ-values are systematically a few per
cent smaller for heavier than for light molecules, although the
differences are mostly within the uncertainty. According to Eq.
1.19 such differences might be explained by corresponding differ-
ences in the electronic stopping cross section $S_e(E)$, but typi-
cally we would expect "cluster effects" to give larger energy
loss for protons travelling in clusters (see Sect. 3.4.ii).
Another possibility is to consider a molecular projectile as
composed of positive and neutral particles inducing correspond-
ingly different secondary emissions[147], but this would not ex-
plain why also D_3^+-ions give slightly lower δ-values than do
H_3^+-ions. At any rate, the differences are too small to justify
too many speculations.

Parabolic curve fits through all points give

$$\delta_{H_2} = 3.911 \cdot 10^{-2} + 9.778 \cdot 10^{-2} \cdot E - 1.6 \cdot 10^{-3} \cdot E^2 \qquad (4.3)$$

for H_2, and

$$\delta_{D_2} = 4.062 \cdot 10^{-2} + 1.7059 \cdot 10^{-1} \cdot E - 4.89 \cdot 10^{-3} \cdot E^2 \qquad (4.4)$$

for D_2. The results for solid H_2 was 63-68% of those for solid
D_2 over the whole energy range. This difference has been at-
tributed[18] to a smaller range of internal secondaries in H_2 due
to larger energy losses to target nuclei, and we note that the
same ratio is found for incidence of $^4He^+$-ions and electrons
(see below).

For 3-10 keV $^4He^+$-ions (Fig. 4.2) a somewhat different energy
dependence is found, but again a ratio, $\delta_{H_2}/\delta_{D_2}$, of 0.65-0.68
is observed.

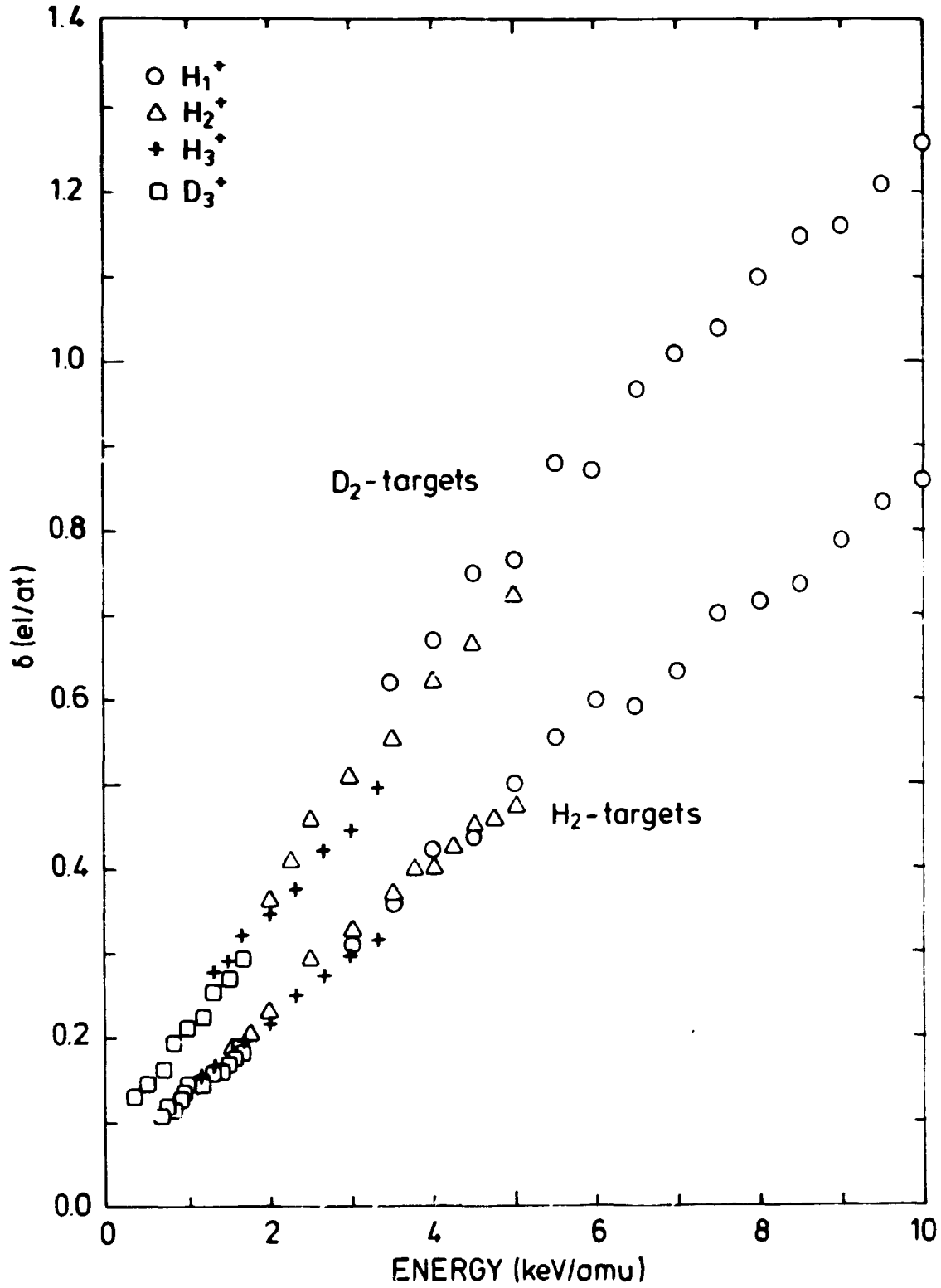**Fig. 4.1.** Secondary electron emission coefficient δ vs. incident energy, for H_1^+-(o), H_2^+-(Δ), H_3^+-(+) and D_3^+-($\square$) beams incident on solid H_2 (lower values) and D_2 (Higher values).

Roughly the same behaviour is seen for 5-10 keV $^{14}N_1^+$-ions. For comparison also the parabolic fits (Eqs. 4.3 and 4.4) are shown in Fig. 4.2 , and finally a set of δ-values for 5-10 keV $^{20}Ne^+$ incident on H_2 is included.

Calculating the material parameter Λ_{exp} from the above data (Eq. 4.2) we are faced with a need for $S_e(E)$-values. For hydrogen-ions we may simply use the experimental values of Sect. 3.5, while for $^{14}N_1^+$- and $^{20}Ne^+$-ions our best choice seems to be the
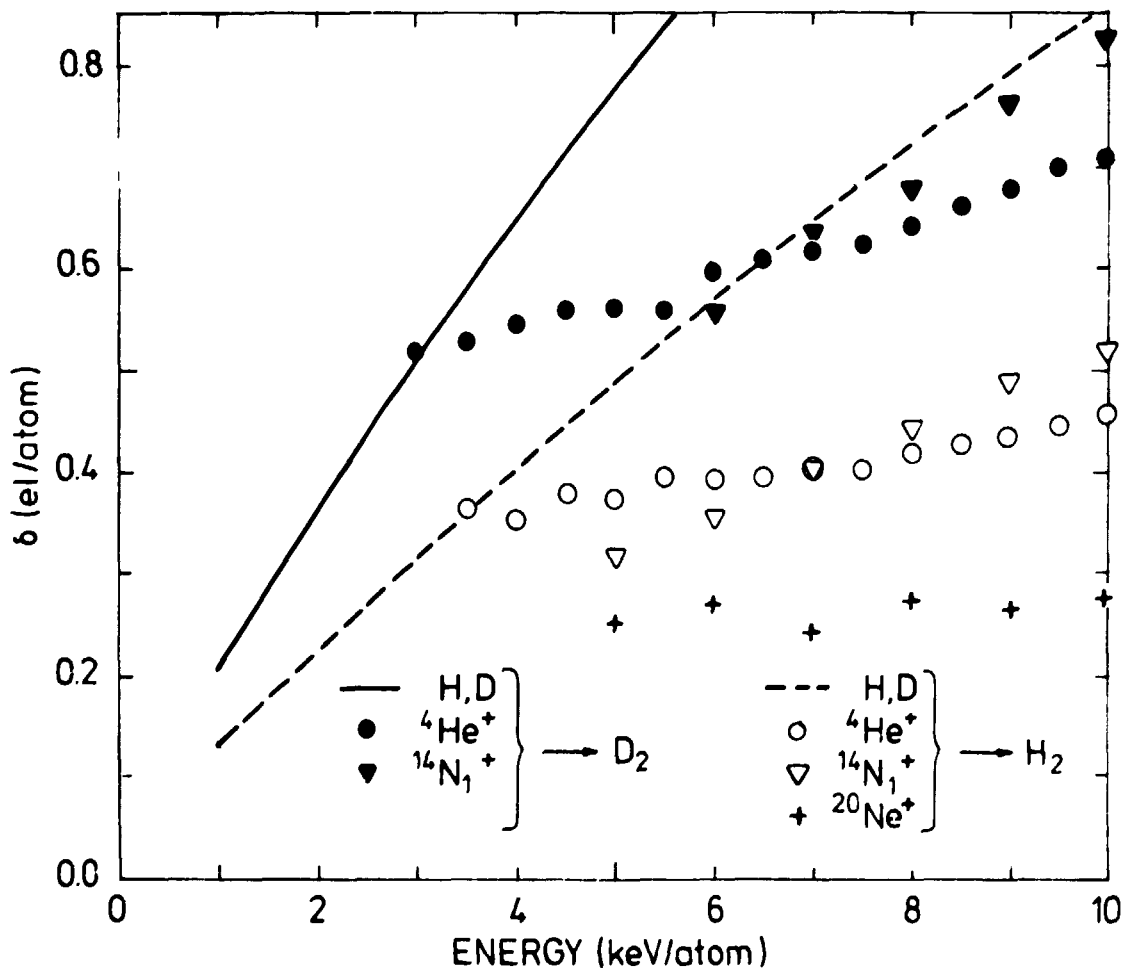
Fig. 4.2. Secondary electron emission coefficient δ vs. incident energy, for $^4He^+$-(o), $^{14}N^+$-($\triangledown$) and $^{20}Ne^+$-(+) ions incident on solid H_2, and for $^4He^+$-($\bullet$) and $^{14}N^+$-($\blacktriangledown$) ions incident on solid D_2. Also shown are the parabolic fits (Eqs. 4.3 and 4.4) to δ-values for hydrogen and deuterium incident ions on H_2 (broken curve) and D_2 (solid curve).

theory of Lindhard and Scharff[20] (Eq. 1.7). For $^{20}Ne^+$-ions, at least, we would expect[22] this to be valid. However, for $^4He^+$-ions we have no particular reason to trust the theory, however:

For hydrogen-ions we found very good agreement between our ranges in solid H_2 and those of Cook et al.[88] in gaseous H_2 (see Sect. 3.5). It is therefore not unreasonable to assume also the results of Cook et al. for $^4He^+$-ions in H_2. However, these were only measured at 20 keV and above, where they are in very good agreement with the semi-empirical stopping cross sections of Ziegler[101]. In lack of a better alternative we therefore prefer to use the electronic stopping cross section of Ziegler[101] for 3-10 keV $^4He^+$ in H_2, but Λ_{exp} was also evaluated using Eq. 1.5.

A plot of Λ_{exp} (Eq. 4.2) vs. energy for H_2 (Fig. 4.3) now apparently brings some systematics to our data, i.e. there does indeed appear to be a relation between δ and S_e. It should be noted that in Fig. 4.3 the highest set of points (Δ) is calculated from Ziegler's S_e for $^4He^+$, while the assumption of Eq. 1.7 for $^4He^+$ gives much better agreement with the other data. With the remarks of Sect. 4.1 in mind, though, this is not sufficient argument to prefer one set of $S_e(E)$-values from another. The other Λ_{exp}-values are seen to agree within a factor of ~ 2. The heavier ions are indeed expected to give lower Λ_{exp}-values (as seen), because of larger contributions from recoiling target atoms[1,148] to $D(0,E)$, and thus to β.

For a given projectile, the electronic stopping cross section $S_{p,e}$ is essentially the same in H_2 and D_2 (see Sect. 3.5), so in general we find that $\Lambda_{exp}(H_2)/\Lambda_{exp}(D_2) = \delta_{H_2}/\delta_{D_2} \approx 0.65$ for any light ion (Eq. 4.2).

ii) N_2-targets: For incidence of hydrogen ions the secondary electron emission coefficient δ is essentially proportional to the square root of incident energy per mass unit (Fig. 4.4). Assuming the experimental stopping cross section S_e of Fig. 3.20 we then obtain a constant $\Lambda_{exp} \approx 0.77 \pm 0.05 \cdot 10^{15}$ atoms/eV cm^2, i.e. more than a factor of five larger than the corresponding parameter for H_2-targets. It seems reasonable that this reflects
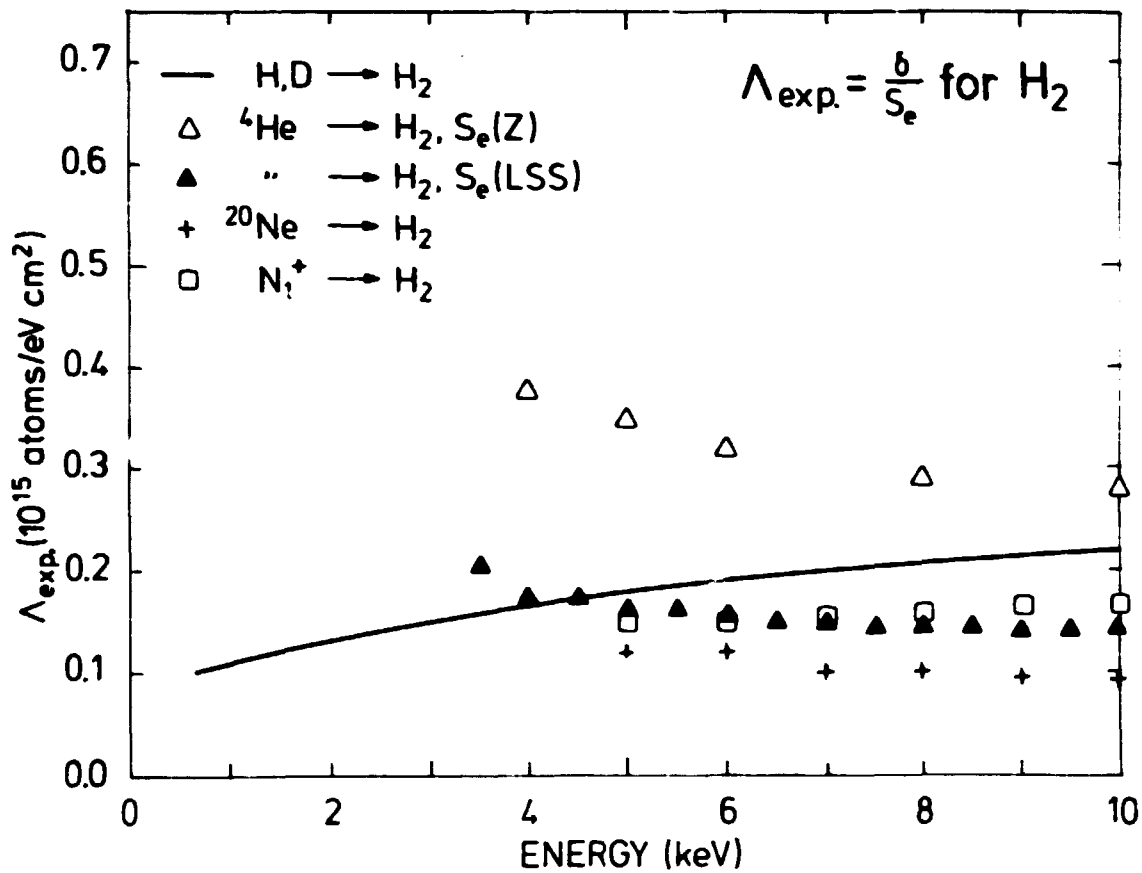
Fig. 4.3. "Experimental material parameter" $\Lambda_{exp} = \delta/S_e$ vs. incident energy, for solid H_2. Incidence of $^{20}Ne^+(+)$, $^{14}N^+(\square)$ and hydrogen and deuterium ions (solid curve). For incidence of $^4He^+$-ions Λ_{exp}-values are calculated assuming the S_e of Lindhard and Scharff[20] (▲) and of Ziegler [101] (Δ).

a basic difference between the target materials (and thus between the parameters Λ of Eq. 1.18), since the escape depth for secondary electrons is almost an order of magnitude larger for solid N_2[12] than for solid H_2[11,18], i.e. in the case of N_2 a considerably thicker layer contributes to the emission. Also, the different reflection properties of the targets might, in principle, play in: For hydrogen ions incident on solid N_2 the reflection coefficient is estimated to be 5-15% in the present energy range (see Sect. 6.2). Thus reflected projectiles might contribute to the surface energy $D(0,E)$, i.e. alter the factor β (Eq. 1.19). However, we shall see in Sect. 4.4.ii that $\beta_{N_2} \sim \beta_{H_2}$, so this contribution should be small.
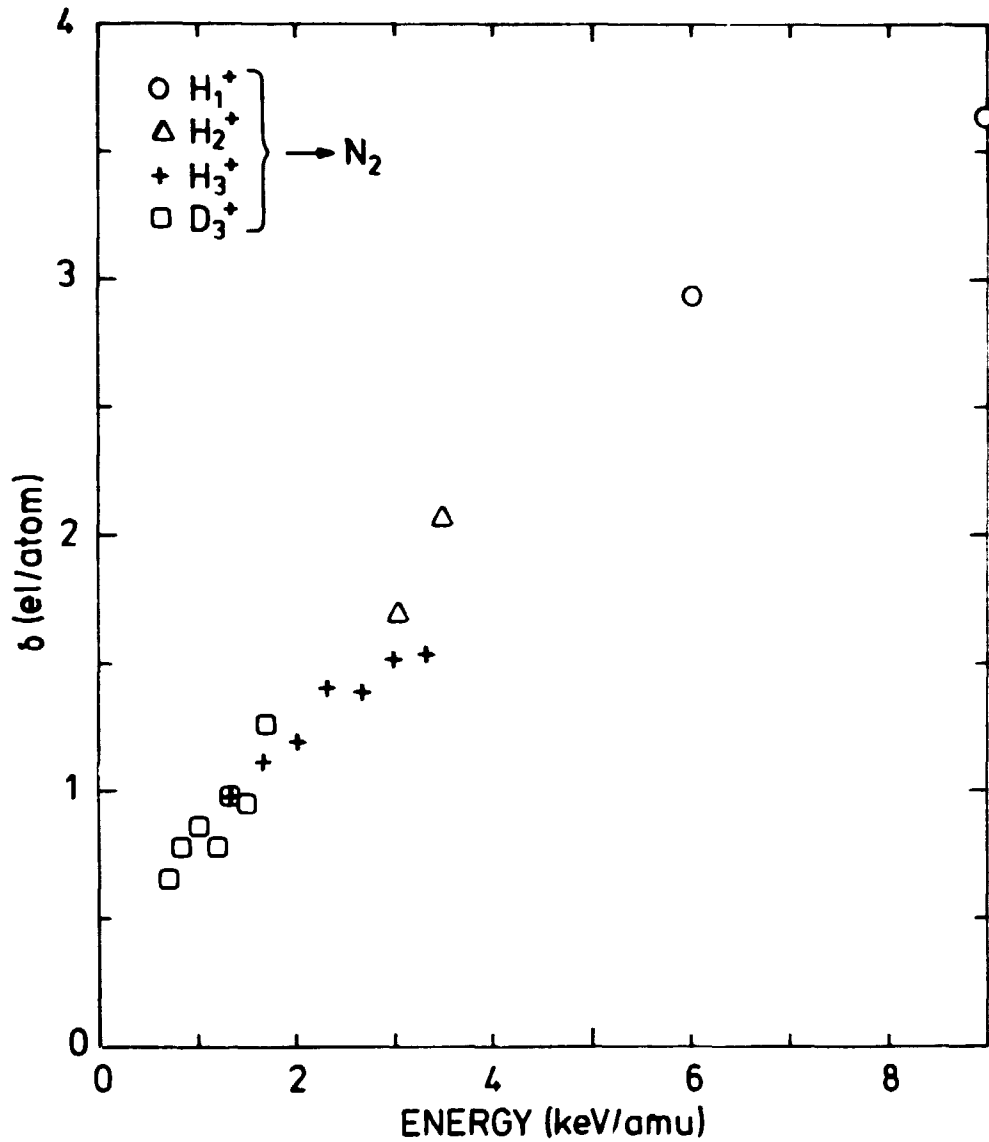
Fig. 4.4. Secondary electron emission coefficient δ vs. incident energy per mass unit, for H_1^+-(o), H_2^+-(Δ), H_3^+-(+) and D_3^+-(□) ions incident on solid N_2.

We note that assuming instead the $S_e(E)$ of Andersen and Ziegler[19] for N_2-gas (see Sect. 3.5) we would get $\Lambda_{exp} \simeq 0.29 \cdot 10^{15}$, i.e. only about twice as large as for H_2. In view of the above this seems a bit low (see also below).

4.3. Electron-induced emission

The secondary electron emission coefficient δ (defined in Eq. 2.4) has been determined previously for normal and oblique incidence of 0.5-3 keV electrons on solid H_2 and D_2[13,18] and for normal incidence of 1-3 keV electrons on solid N_2[12].

For hydrogen targets[13,18] δ was essentially inversely proportional to the energy E, and also here $\delta_{H_2}/\delta_{D_2} = 0.65$. For normal incidence a parabolic curve fit gave[13]

$$\delta_{D_2} = (0.201+0.0736E-0.0118E^2)/E \qquad (4.5)$$

for solid D_2, and simply 65% hereof for H_2. E is here given in keV. Recently, we have checked these results in connection with independent measurements[6] on HD-targets and mixtures of H_2 and D_2, and found very good agreement. Thus, we estimate the uncertainty to be less than 5%.

Assuming Eq. 1.4 for $S_{e,e}(E)$ (see Sect. 3.6.2), we find a material parameter $\Lambda_{exp} \approx 0.31 \cdot 10^{15}$ atoms/eV cm^2 for solid H_2, which is quite encouraging (see Fig. 4.3). As mentioned above the lightest projectiles are indeed expected to give the highest Λ_{exp}. Clearly, since $S_{e,e}(E)$ is the same in H_2 and D_2 we have $\Lambda_{exp}(H_2)/\Lambda_{exp}(D_2) \approx 0.65$ (see Eq. 4.2).

For N_2-targets[12] the coefficient is again considerably larger than for hydrogen. The uncertainty, however, is also larger[4] (5-7%). Here δ varies more like $E^{-0.7}$, decreasing from 2.4 at 1 keV to 1.2 at 3 keV. Assuming again Eq. 1.4 for $S_{e,e}(E)$ the material parameter becomes $\Lambda_{exp} \approx 1.0 \cdot 10^{15}$ i.e. in good agreement with the value found for ions assuming our experimental $S_{H,e}(E)$-values for solid N_2 (see Sect. 4.2.ii). Unlike for ions, $\Lambda_{exp}(N_2)$ exceeds $\Lambda_{exp}(H_2)$ by only a factor of $\sim$ for electrons, although reflected electrons are much more effective in producing secondaries than are reflected ions. Furthermore, the reflection coefficient for N_2 is actually larger[12] ($\sim$ 15%) for electrons, but still unimportant, as we shall see in Sect. 4.4.ii.

4.4. Stopping in solid N_2

The most controversial result of Chapter 3 was the very low stopping cross section for hydrogen ions in solid N_2. This result was reached by two methods based on somewhat different assumptions, but both involving the penetration of a film and reflection from a substrate. Furthermore, both methods depended on the probability that an emitted particle would be positive.

We shall now once more attempt to determine S_e for hydrogen ions by a different method. This method is based on many more assumptions than the two previous ones, and thus should not really be trusted on its own, but the assumptions are here of a quite different nature and the agreement with the previous results, therefore, still supports these:

We recall that the stopping cross sections in solid H_2 were in good agreement with theory (and experiments in gases), so we shall base our data analysis on these. From this, and measurements of secondary electron emission coefficients δ (see above), we then propose to determine S_e for N_2.

i)   Method: For a target material A we may rewrite Eq. 4.2 as

$$S_{p,e}(E,A) = \delta_A / \Lambda_{exp}(A) \tag{4.6}$$

and for the same projectile in another material B we then immediately have

$$S_{p,e}(E,B) = \frac{\delta_B}{\delta_A} \frac{\Lambda_{exp}(A)}{\Lambda_{exp}(B)} S_{p,e}(E,A) \tag{4.7}$$

We now propose to use this equation to extract $S_{H,e}(E,N_2)$ from $S_{H,e}(E,H_2)$. Clearly the ratio, $\delta_{N_2}/\delta_{H_2}$, of the electron emission coefficients may be determined directly, but also the ratio, $\Lambda_{exp}(H_2)/\Lambda_{exp}(N_2)$, of the material parameters must be known. Our method is based on the assumption that the latter ratio is the same for incidence of electrons as for protons. This is certainly not a trival assumption, but is justified for our case below, and in Ref. 4.

ii) $\Lambda_{exp}(A)/\Lambda_{exp}(B)$: As we have seen in Sect. 4.2, Λ_{exp} actually depends to some extent on the projectile, through the factor β (Eq. 4.1). This is so essentially for three reasons[1]

a) The energy spectrum of the primary excitation is different for very different projectiles.
b) The reflection of the projectile depends on the projectile.
c) The production of recoiling target atoms depends on the projectile.

As for c) we note first that both electrons and protons produce very few recoils by elastic collisions. It does seem that they may produce recoils through electronic processes (see Chapters 5 and 6), but this is not yet really understood.

If we compare first H_2- and D_2-targets the reflection coefficients are negligible. There is no reason why a) and c) should not be just as important here as for any other target-pair, but still the ratio $\Lambda_{exp}(H_2)/\Lambda_{exp}(D_2)$ was found to be the same for both light ions (Sect. 4.2.i) and electrons (Sect. 4.3).

For solid N_2, however, the reflection coefficients were $\lesssim$ 15% (Sects. 4.2.ii and 4.3) so here a projectile dependent contribution to δ_N could be important.

We therefore compare β_{N_2}/β_{H_2} (see Eq. 4.1) for electrons and protons, and find essentially no difference:

For incidence of 2 keV electrons we estimate β_{N_2} and β_{H_2}(partly) from the distributions[149] $D(x,E)$, see eq. 1.19) as described in Ref. 52, and find $\beta_{N_2}/\beta_{H_2} \approx 1.07$. As the reflected electrons are much more efficient than the reflected ions, in producing secondaries, the ratio β_{N_2}/β_{H_2} is expected to be larger for electrons than for ions, i.e for ions the ratio must be somewhere between 1.0 and 1.07.

Thus, in conclusion we may determine $\Lambda_{exp}(H_2)/\Lambda_{exp}(N_2)$ of Eq. 4.7 from experiments with electrons.
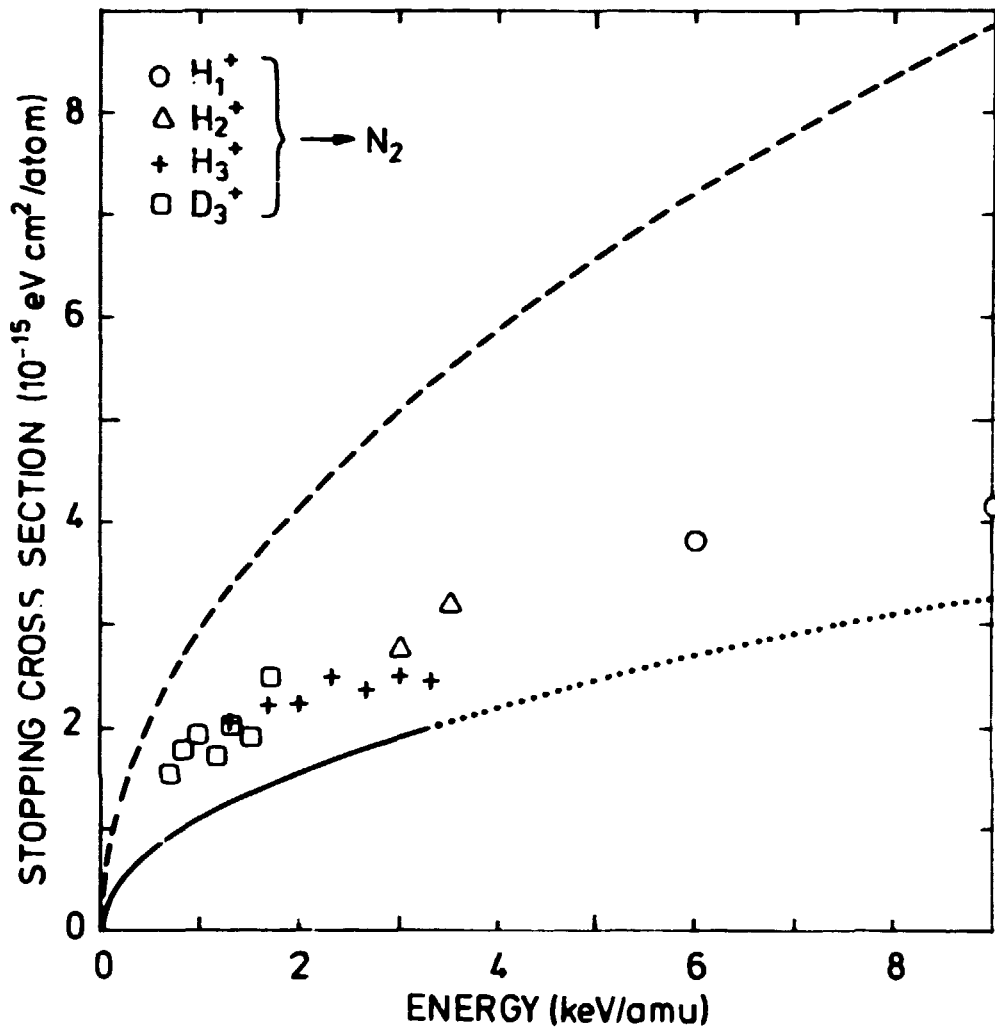
Fig. 4.5. Electronic stopping cross section vs. energy for hydrogen and deuterium ions in N_2. Results extracted from experimental δ-values for H_1^+-(o), H_2^+-($\triangle$), H_3^+-(+) and D_3^+-($\square$) ions. Also shown is S_e obtained by fitting R_p to exp. ranges R_L (see Fig. 3.20), indicated as a solid curve in the energy range where R_L-values existed (Figs. 3.17 and 3.18) and extrapolated as a $\sqrt{E}$-dependence (dotted curve). The semiempirical[19] S_e (broken curve) is included for comparison.

iii) Results: The stopping cross sections for hydrogen ions in solid N_2 were now determined by means of Eq. 4.7. For the corresponding $S_e(E)$-values in solid H_2, the experimental results of Sect. 3.5 (Fig. 3.21) were assumed, and the secondary electron emission coefficients δ_{N_2} and δ_{H_2} were taken from the data of Sect. 4.2 . The ratio $\Lambda_{exp}(H_2)/\Lambda_{exp}(N_2)$ was calculated from Eq. 4.2 using data for incidence of electrons (Sect. 4.3), where the stopping cross sections $S_{e,e}(E)$ were evaluated from Eq. 1.4 (see Sect. 3.6.2). The accuracy of the results is best at the highest energies where all the above data are largest, despite the larger relative uncertainty of the $S_e(E)$-values for H_2. This also means that we can extend our $S_e(E)$-measurements for N_2 to higher energies than with range- or backscattering measurements.

The results are shown in Fig. 4.5 together with the two curves from Fig. 3.20: $S_e(AZ)$ for N_2-gas, and $S_e(R_L)$ for solid N_2 derived from our range-data (Sect. 3.5). The latter curve is extrapolated beyond the actual measurements of Sect. 3.5. The uncertainties are estimated to be of the order of 25%, probably more at the lower energies.

Varying between 45% and 65% of $S_e(AZ)$, the results are in quite good agreement with the backscattering measurements (see Fig. 3.20), and confirm the observation that S_e is indeed much lower in solid than in gaseous N_2. These results are based on the stopping in solid H_2, but here no gas-solid difference was observed.

5. ELECTRON INDUCED SPUTTERING

The linear collision cascade theory[29] for heavy-ion sputtering
of metals is totally inapplicable to the sputtering of condensed
gases by ions or electrons. Various models have been proposed
instead, in order to explain both the apparent conversion of
electronic into nuclear energy and the subsequent dissipation
of this energy (Sect. 5.1). It seems reasonable to assume that
the thermal and/or electrical properties of the target materials
are of importance for the observed sputtering.

Simple considerations (Sect. 5.2) show, that the unusual magni-
tude of various important factors (notably the binding-energies
and target masses) might conceivably make the sputtering of solid
hydrogens a particularly complex phenomenon.

Very few experiments have been made with electron induced sput-
tering of condensed gases, and only one reference is found
quoting absolute yields from solid hydrogens (Sect. 5.3).

The present measurements are based on continuously monitoring
the target thickness by means of the electron emission induced
by the eroding beam itself (Sect. 5.4).

The erosion was found to be independent of beam intensity and
temperature below ~ 3.5 K for solid D_2 and below ~ 3 K for H_2
(Sect. 5.5).

The erosion yield for solid D_2 decreased with target thickness
up to ~ 650 Å, reaching a "bulk" value of ~ 7.8 atoms/el. inde-
pendently of incident electron energy. The erosion of solid H_2
was thickness dependent up to more than twice this thickness, but
the bulk erosion yield was only about twice as high (Sect. 5.6).

The data are far from sufficient to permit much theoretical
interpretation (Sect. 5.7).

5.1. Sputtering of condensed gases

Recently, there has been a growing interest in the sputtering of condensed gases by energetic ions and electrons, partly because of the observed large deviations from the well established linear sputtering theory (see Sect. 1.3). Most of the experiments have been made with ions (see Sect. 6.3), and the results typically exceed the estimates of Eq. 1.16 by orders of magnitude. In the search for explanations the most significant result until now seems to be that the erosion of frozen gases is due predominantly to energy initially deposited in the electronic system[43-46]. Apparently, the erosion yields of both ice and noble gases scale with S_e^2, the square of the electronic stopping cross section. Various models have been proposed in order to explain this dependence, but we should note that some of them are also capable of explaining another S_e-dependence:

i) In the "ion-explosion" model of Brown et al.[32] the ionization induced by the projectile causes the formation of a positively charged region around the path. At the surface Coulomb repulsion between positive ions then causes an ejection of atoms. This model depends heavily on the immobility of electrons, and it is argued[46] that in rare-gas solids we should expect an "explosion" to be inhibited by fast 're-neutralization'. This is not necessarly so for diatomic molecular solids where the electron mobilities are 10^5-10^9 times lower[85,150], and we have seen (Sect. 2.7.iii) that in D_2 some amount of beam-induced ionization remains stable for hours after irradiation.

Because of the assumed participation of two ionized target pa - ticles, the model predicts an S_e^2-dependence[32,50]. If indeed the charge state of an emitted particle is determined outside the surface[114] (see also Sect. 3.4.iii), an "ion-explosion" need not result in a positive emission (see Sect. 6.1)! Energy deposited directly in nuclear motion may, of course, also lead to sputtering, but the two contributions should be essentially independent.

ii) Haff[50] instead suggested that an "ion-explosion" would initiate a collision cascade, which would then cause sputtering.

Such cascades will, of course, be very short, since the ion-explosion yields only low energy recoils, but the model includes the previous one (i) as a special case. Also, this model naturally depends on the electron mobility in the target material, and predicts an S_e^2-dependence.

iii) Versions of a "thermal" model are described and discussed by different authors[45,46,32]:

Following excitation by the primary particle, secondary ionization, photon, and phonon generation all help to distribute the energy without spreading it much. If sufficient energy is somehow transferred to atomic motion ("heat") much faster than it is dissipated by thermal diffusion, etc., a local region may be raised to a sufficient temperature to make evaporation from the surface important.

Various mechanisms have been suggested for the rapid conversion of electronic into nuclear energy: "ion-explosion" as in UF_4[51], elastic scattering of secondary electrons on nuclei, inelastic electron molecule collisions, and neutralization between positive and negative ions. An estimate of the times involved may help eliminate some of them[46]. Such an estimate[166] seems to show that a very rapid conversion of electronic into nuclear energy may in some cases occur via the formation of a "core plasma" around the primary particle track.

For any model based on evaporation we expect the sputtering yield to increase rapidly with increasing initial target (substrate) temperature near the "evaporation temperature"[46].

The S_e^2-dependence is possible with a "thermal" model, but not necessary. We should also keep in mind that such a model is almost forced to include a dependence[45] on S_n, since energy deposited initially in nuclear motion will certainly contribute to the "heat".

iv) Some of the absolute sputtering yields are reasonably well estimated by a modification of Eq. 1.16:

Assuming for simplicity that all the energy initially deposited in the electronic system is "immediately" transferred into nuclear motion (see also Sect. 5.2), we substitute the electronic energy deposition rate $D(0,E)$ for $F_D(0)$ in Eq. 1.15. A thorough discussion of why such a substitution is actually unreasonable is outside the scope of this work, and quite unnecessary. It is not the intention of the author to propose any kind of "model", but only to point out that if we further insert the $D(0,E)$ from Eq. 1.19 we arrive at a quite useful expression

$$Y_e \cong \frac{0.042}{U_0[Å^2]} \cdot \beta \cdot S_{e,e}(E) \tag{5.1}$$

which is formally equivalent to Eq. 1.16. Independent of the above considerations, it is not unreasonable to propose a sputtering yield which is proportional to the energy deposition rate divided by the sublimation energy.

For very large erosion yields, as observed for keV ions, we should substitute instead $D(x,E)$ for $F_D(x)$ in Eq. 1.17. This may be done along the lines sketched in Ref. 33, assuming a Gaussian distribution for the depth distribution of the deposited energy:

$$Y_{high} \cong \frac{D(0,E)}{\pi^2 U_0}(2\langle\Delta R_I^2\rangle)^{1/2} \exp\left\{\frac{\langle R_I\rangle^2}{2\langle\Delta R_I^2\rangle}\right\} \ erf\left\{\frac{x-\langle R_I\rangle}{(2\langle\Delta R_I^2\rangle)^{1/2}}\right\}_o^h \tag{5.2}$$

Here $\langle R_I\rangle$ and $\langle\Delta R_I^2\rangle^{1/2}$ are, respectively, the average depth and straggling of the distribution, in our estimate taken from Winterbon's tables[90].

5.2. Sputtering of solid hydrogens

The solid hydrogens constitute an extreme type of target material, first of all because of the particularly low bulk and surface binding energies. The binding between condensed molecules is the result of a competition between Van der Waals forces and the kinetic energy of the molecules. Already at $0°$ K the repulsive energy is ~ 70% of the Van der Waals attraction in an undis-

turbed H_2-target (Sect. 1.5), and the presence of radiation might have quite drastic effects:

We shall see later (Sect. 6.6.3) that an 8 keV H_3^+-ion may cause the emission of over $2 \cdot 10^4$ H_2-molecules, corresponding to a crater of diameter and depth ~ 70 Å. It has been suggested that the presence of a highly disrupted surface may cause a considerable reduction in surface binding energy[34-36]. Another effect that might result in reduced average surface binding energy per atom is cluster emission. Clusters of up to 99 atoms have been observed[151] from solid H_2 bombarded by low energy electrons, and it would not be surprising if some of the $2 \cdot 1C^4$ H_2-molecules mentioned above were actually emitted in clusters.

It is thus impossible to predict an effective surface binding energy for sputtering of solid hydrogens, but probably the sublimation energy may be taken as an upper limit.

Implicit in most discussions of sputtering theory[152] is the minimum energy, E_{min}, an atom must have in order to be considered "in motion", although this energy is not always specified. We shall want E_{min} to be negligible compared to displacement energies and surface binding energy, and ignore any effect which does not eventually lead to an energy transfer larger than E_{min} to the nuclei (see Sect. 1.3.i). For solid hydrogen targets E_{min} then becomes so small that we must carefully consider a multitude of different processes which might safely have been neglected for less volatile target materials. This problem is further enhanced by the low nuclear masses which mean that even low energy electrons may induce "significant" nuclear motion.

A theoretical treatment of the sputtering process is beyond the scope of this work, but a few simple considerations may illustrate the situation:

i) Incident ions and electrons initially deposit most of their energy in excitations and ionizations (see Sect. 1.2).

Thus, about half the energy loss of a keV electron in H_2 is initially deposited in kinetic energy of internal secondary electrons, while the rest is almost equally shared between excitation and (ionization) potential energy of the ions[17,153].

Due to the low electron mobility and the very low binding energies an "ion-explosion" (see Sect. 5.1) might then be expected to transfer a substantial part of the ions' potential energy to nuclear motion.

Secondary electrons will deposit their energy close to the track of the primary particle, in D_2 within a radial distance[11] of less than 50 Å and in H_2 even closer[18]. Electrons with energy above 10 eV lose energy by ionization and by excitation of electronic states[154,155], and in this way another 10-20% of the primary energy loss is converted to potential energy of ions (for electron incidence)[17]. The secondary electrons are thus quickly degraded to energies below 10 eV, where they still retain ~ 10% of the primary deposited energy. Now they will collide with almost all molecules around them, losing energy to the nuclei by elastic scattering (very little) and by excitation of rotational and vibrational molecular states[17]. In H_2, the threshold for excitation of vibrational states is 0.516 eV[156], so we end up with highly localized quanta of energy considerably larger than both bulk and surface binding energies (local "heating").

The principles above hold for incidence of electrons as well as ions, although the harder recoil spectrum due to electrons may cause a larger spreading of secondary electrons.

These considerations are by no means quantitative, and little concern has been given to the precision of details and numbers. However, it has been illustrated that the sputtering of hydrogen is probably a very complex process. That it is also a very violent (non-linear?) process may then be illustrated by a primitive estimate of the energy densities to be expected:

The time scale of "ion-explosions", if they do occur, is quite short. From the total stopping cross section[17] in H_2, we estimate

that a substantial part of the sub-excitation energy is deposited
within ~ 10^{-11} sec. Ignoring any question about the validity of
classical heat-conduction we further estimate that within that
same time thermal diffusion[53] will have spread the "heat" radially
by 30-50 Å, i.e. the primary energy loss may be assumed to be
distributed within a cylinder of radius ~ 60 Å. An incident H_1^+-
ion of energy 2.7 keV/amu deposits ~ 1.25 eV/A, i.e. an H_3^+-ion
creates an energy density of ~ 12.5 meV/H_2-molecule within the
cylinder. We recall that the sublimation energy is ~ 8 meV/H_2.
So bombardment with such ions is certainly a violent treatment
of our target, and we may be dealing with some kind of
"spike"[152].

It should be noted that the estimated energy density is unlikely
to be uniformly distributed.

In view of the above, any agreement with ordinary sputtering
theory (Eq. 1.16) would be highly surprising, and in the follow-
ing our results will therefore not be described in terms of
their deviation from Eq. 1.16.

5.3. Sputtering by electrons

As mentioned in Sect. 1.3.ii the understanding of sputtering by
ions may sometimes be complicated by the possible contributions
of both nuclear and electronic energy transfer. In that case one
might conceivably clear up some of the questions by comparing
with results for sputtering by electrons, since these transfer
their energy predominantly to the electronic system. However,
it should be noted that also electrons suffer nuclear collisions,
and, for instance, collisional sputtering af Au-foils by 600 keV
electrons has been observed[157]. For condensed gases the same may
occur at much lower energies[158] since the binding energies here
are particularly small (see Sect. 1.3.i). Thus a 15 eV electron
colliding head-on with a proton will transfer more than the
sublimation energy for an H_2-molecule!

Still, for those materials where excitation or ionisations may lead to sputtering, this is likely to be the dominant contribution to the sputtering by electrons.

Electron beam sputtering experiments are not very numerous, and confined to very few types of target materials. Most work has been done on alkali halides, where, for instance, yields of 3-17 atoms/electron were observed[41] for 500 eV electrons. As mentioned in Sect. 1.3.ii, the corresponding sputtering mechanism appears to be specific to these compounds.

Ollerhead et al.[45] made an attempt to measure the erosion of thin films ($\sim 5 \cdot 10^{16}$ atoms/cm^2) of solid Xe, and estimated a yield of of the order of 0.03 atoms/el, and qualitative results[158] for 40-60 eV electrons incident on thin crystals ($\sim$ 20 monolayers) of Xe, Kr, Ar, and Ne indicate increasing desorption rates with decreasing (bulk) sublimation energies. However, as mentioned in Sect. 5.1.i, the mechanisms of sputtering of noble gases may be quite different from those for diatomic molecules.

Erents and McCracken[47] bombarded H$_2$-films with 2 keV electrons and measured the resulting pressure increase in the vacuum chamber. The film thickness is deduced from the gas inlet time assuming a sticking coefficient. The erosion yield was found to vary with film thickness up to something like half the penetration depth, reaching finally a bulk yield of the order of 200 atoms/el. The yield decreased with increasing energy between 2 and 5 keV. It should be noted that these measurements were made at 3.2 K, i.e. near the temperature dependent region for H$_2$ (Sect. 5.5). The method is discussed further in Sect. 6.3. Presently, measurements are in progress on the erosion of solid H$_2$[8], D$_2$[7,8], HD[8], N$_2$[9], O$_2$[9], CO[9], and Ne[10] by 1-3 keV electrons.

5.4. Experiment

The mirror-substrate method for range measurements (see Sect. 3.6) is based on measuring the electron reflection coefficient η (see Sect. 2.4.ii) for light films on a heavy substrate as a func-

tion of the film thickness ∆X. For keV electrons incident on D_2-films on an Au-substrate η(∆X) was found to decrease linearly until the thickness d ≈ R_p/2 (see Fig. 3.22). By means of the known η(∆X)-curve we might now instead determine an (unknown) film thickness $∆X_u$ by measuring the reflection coefficient η($∆X_u$).

In the present erosion measurements we suppress secondary electron emission by applying a bias of -45 V to the grid (see Sect. 2.4.ii), and collect the target current i_t^- continuously during irradiation, as described in Sect. 2.6. From this we immediately obtain the reflection coefficient η versus incident beam dose, and by reference to the η(∆X)-curve we are thus continuously monitoring the target thickness ∆X by means of the eroding beam itself.

The electron beam is focussed to a diameter of ~ 0.7 mm and then swept horizontally and vertically by two independent sawtooth voltages over a 2 mm circular aperture in front of the target (see Sect. 2.3). This ensures a closely uniform beam intensity over the entire beam spot.

The beam current i_b is measured by deflecting the beam so that it is swept instead over a 2 mm aperture in front of the Faraday cup (see Sect. 2.3).

The sensitivity of the measurement is limited by the slow variation of η with ∆X. For initial film thicknesses below a few hundred Å this variation is prohibitively small, and we measure instead the sum of reflected and secondary electrons: The total emission coefficient (η+δ). This quantity varies strongly for ∆X < 50 Å (see Fig. 3.22) where the large number of secondary electrons from the Au starts contributing to the emission.

Unfortunately, the secondary electron emission is sensitive to the structure of the surface. Crater formation will increase the irradiated surface area and alter the angles of incidence (compare Sect. 1.3.i). Thus, we may expect δ to vary not only with film thickness during erosion. In contrast, it is reasonable to

assume that the reflection coefficient η will be less sensitive to the state of the surface and be characteristic only of the average remaining target thickness. Except for the thinnest films we therefore prefer to use only η for our measurements.

Figs. 5.1 and 5.2 show the variation of η and (η+δ), respectively, with incident beam dose D for 2 keV electrons incident on various films of solid D_2.

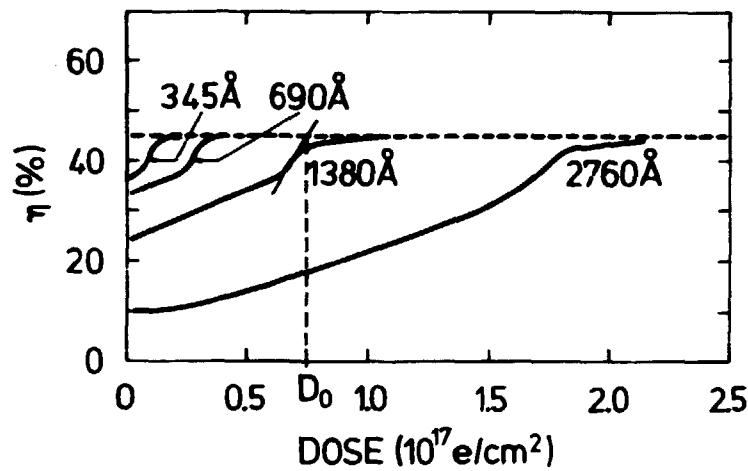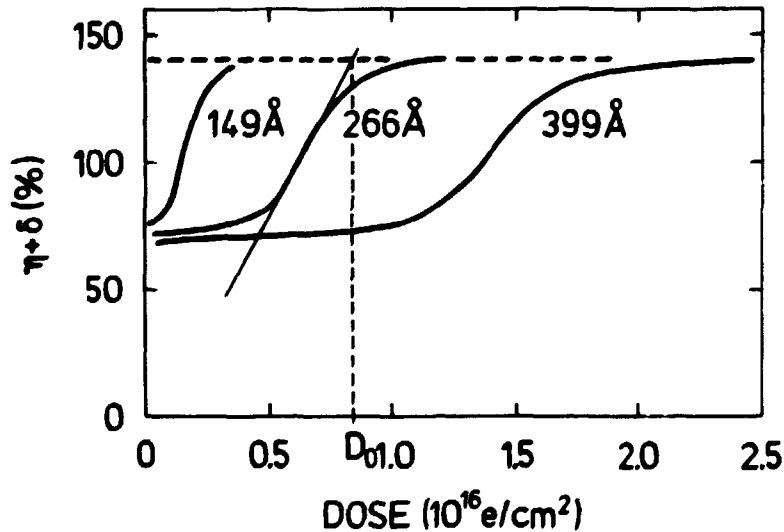Fig. 5.1. 2 keV e → D_2/Au. Reflection coefficient η vs. accumulated beam dose D for various film thicknesses X_o.

Fig. 5.2. 2 keV e → D_2/Au. Total emission coefficient (η+δ) vs. accumulated beam dose D for various film thicknesses X_o.

5.5. Investigation

i) The substrate was heated to various temperatures during
erosion (see Sect. 2.1). The thermometer was not calibrated, so
the temperatures were estimated only to within ± 0.2 K. It was
found that the erosion of D_2 was independent of temperature
below ~ 3.5 K. Above 4.2 K the erosion was strongly enhanced.

ii) The beam intensity was varied between 0.1 and 11 $\mu A/cm^2$. In
the temperature independent region (see above) the variation of
n and (n+δ) with incident beam dose remained unaffected within
the reproducibility (±10% for very thin films, better for thicker
films). This made the further collection of data considerably
easier. In the temperature-dependent region the target tempera-
ture would vary with beam intensity and the situation grew
complex.

iii) The erosion process was interrupted for periods of 10-15
minutes and then continued. There was no significant effect of
such interruptions. During the erosion of very thick films (dur-
ation up to 4 hours) we could therefore interrupt the irradiation
of the target and measure the beamcurrent in the Faraday cup.

iv) The variation of n with beam dose D over a given thickness
range was apparently independent of initial film thickness,
except for a certain "smearing" for thicker films (Fig. 5.1).
This smearing is probably caused by inhomogenous erosion (crater
formation, etc.).

v) The variation of (n+δ) with beam dose D over a given thick-
ness range depended somewhat stronger on initial film thickness,
as expected (see above).

vi) Suppressing the secondary electron emission during continuous
irradiation, we might expect very thick ("bulk") targets to
charge up negatively (see Sect. 2.7.ii), and thus influence the
primary beam energy. However, this would happen much faster than
any significant erosion, and when the target reached potentials

near the grid bias (-45 V, see Sect. 2.7.ii) the secondary elec-
trons would begin to escape, disturbing the measurement of η.
Such an effect would thus primarily appear when monitoring η for
thick targets, and would apparently raise the "bulk" coefficient
from $\eta(\infty) \sim 1\%$ to $\eta(\infty) + \delta(\infty) \sim 18\%$ (see Fig. 3.22). This would
be a clearly observable effect.

Using film thicknesses up to ~ 8000 Å with 2 keV electrons, no
charge-up effect was observed, in good agreement with the results
of Sect. 2.7.ii.

5.6. Results

Despite our reservations regarding the variation of $(\eta+\delta)$ with
beam dose D (see Sect. 5.5.v), there is little doubt that this
sum reaches the "Au-value" when the film is eroded away. Unfor-
tunately, this value (broken line, Fig. 4.2) is approached almost
asymptotically as the last remnants of the film are slowly eroded
away. We therefore define the erosion as completed for the total
beam dose D_O corresponding to the intercept of the steepest
tangent to the $(\eta+\delta)$-curve with the "Au-level".

Correspondingly, we determine values of D_O from the intercept
of the steepest tangent to the η-curve with the "Au-level"
(broken line, Fig. 5.1).

Plotting the eroded initial film thickness X_O vs. total dose D_O
of erosion (Figs. 5.3 and 5.4), we first note that the points
obtained from the two types of emission curves (Figs. 5.1 and
5.2) agree very well. This supports the assumption that the
erosion process is not significantly influenced by the method
of measurement (build-up of space-charge during secondary elec-
tron suppression, etc.).

Figs. 5.3 and 5.4 are now interpreted under the assumption that
the erosion yield Y depends only on the instantaneous thickness
X_i, i.e. is independent of prior erosion. This is not a trivial
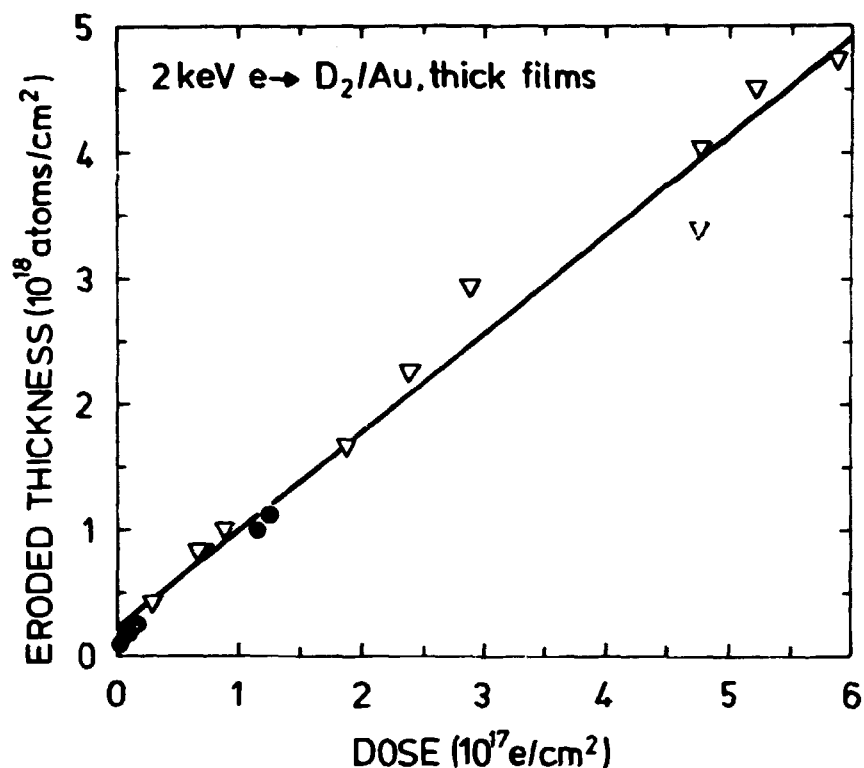assumption (see Sect. 6.6.2.ii), but is justified below. Con-

Fig. 5.3. Initial film thickness X_O vs. total dose D_O of erosion. Thick films. Results from n-curves ($\triangledown$, Fig. 5.1) and ($n+\delta$)-curves ($\bullet$, Fig. 5.2). Solid line: Fit through (D_O, X_O)-points for $X_O > 4 \cdot 10^{17}$ at/cm^2.

sider first the erosion of thick films (Fig. 5.3): There is some scatter of the points for the thickest films, partly due to beam instabilities, but $X_O/(D_O)$ is still essentially linear for $X_O \gtrsim 4 \cdot 10^{17}$ atoms/cm^2 (660 Å). For these thicknesses we thus fit a straight line (see Fig. 5.3) and obtain a "bulk" erosion yield $Y(\infty) = 7.8 \pm 0.5$ atoms/electron. We note that the penetration depth $R \sim 3.5 \cdot 10^{18}$ atoms/cm^2 for 2 keV electrons[11], i.e. unrelated to the region of linearity.

For thinner films (Fig. 5.4, notice the change of scales!) the erosion goes faster, varying with the remaining thickness X_i: For $X_O \lesssim 2.5 \cdot 10^{17}$ at/cm^2 the points are nicely fitted by the broken curve. Included for reference is the straight line from Fig. 5.3. The broken curve corresponds to a differential erosion yield $Y(X_i)$ proportional to $X_i-1.3$ (see Table 5.1).
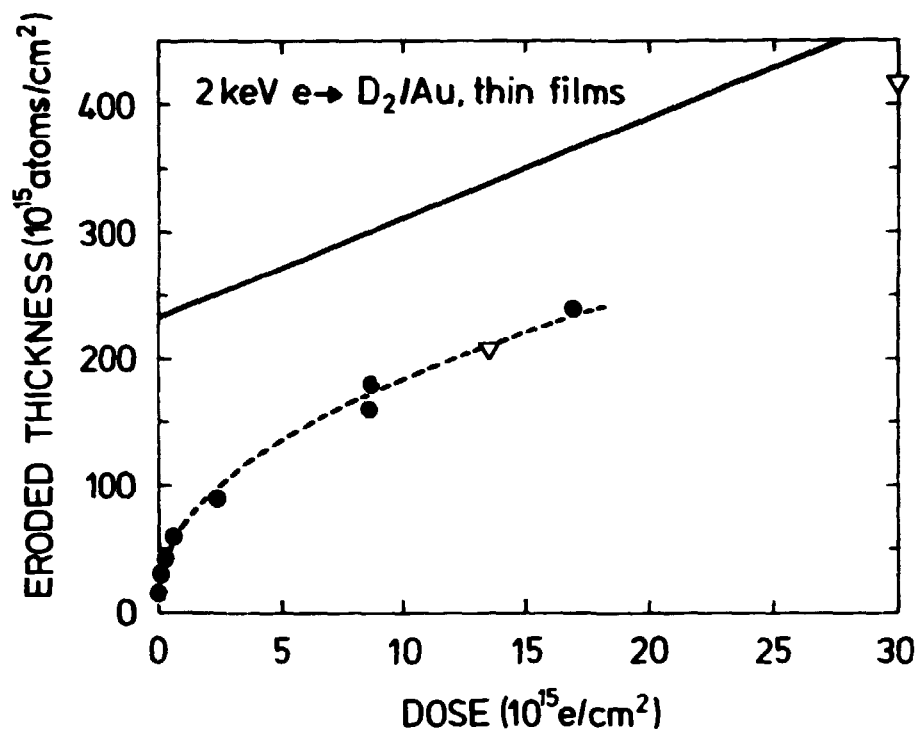
Fig. 5.4. Initial film thickness X_O vs. total dose D_O of erosion. Thin films (note scales!), Results from η-curves (∇, Fig. 5.1) and $(\eta+\delta)$-curves ($\bullet$, Fig. 5.2). Full line: Fit from Fig. 5.3. Broken curve: Fit through (D_O, X_O)-points for $X_O < 2.5\cdot10^{17}$ at/cm^2.

Table 5.1. Erosion yield Y versus remaining film thickness X_i. For 2 keV electrons $\rightarrow$ D_2/Au. From the fits (solid and broken curves) of Figs. 5.3 and 5.4.

X_i	Y
[Å]	[atoms/electr.]
25	199
50	82
100	34
125	26
200	14
"∞"	7.8

It was assumed above that Y depends on X_i, but is independent of X_o. This is essentially confirmed by the observation that the shape of the n vs. D-curve for $X_i < X_o$ is independent of X_o (see 5.5.iv), but let us investigate this more quantitatively. Consider, for example, the ($X_o = 1380$ Å)-curve of Fig. 5.1: If our assumption is correct we may directly convert the slope of the curve into a differential erosion yield $Y(X_i)$, by referring to the relation $n(X)$. The assumption is then confirmed by the good agreement we find with Table 5.1: For $X_i > 500$ Å the yield is constantly ~ 8 atoms/electron, while it increases with decreasing X_i between 500 and 125 Å. For the smallest X_i the yield again tapers off, probably because the substrate has already been reached on parts of the beam spot. For $X_i = 125$ Å a yield of ~ 25 at/el. is in very good agreement with Table 5.1.

The same type of results would be obtained from any of the other curves of Fig. 5.1.

For incidence of 1 keV electrons, the scatter of the data was smaller, and the results were identical to the ones for 2 keV. For 3 keV the scatter was somewhat larger, but no difference was observed within the reproducibility. Thus, for energies between 1 and 3 keV the erosion yield apparently varies less than 15%. For H_2-targets the scatter of the data was quite large, and apparently systematically related to the purity of the substrate surface. Investigations of this behaviour are in progress[8], but we may already estimate a bulk yield of 15 ± 1 atoms/el for 2 keV electrons. The thickness dependence extends up to ~ 1200 Å for this target material.

For the considerably less volatile N_2-targets the corresponding yield is estimated from preliminary measurements to be ~ 1.0 ± 0.3. Results on the energy dependence are to be published soon[9].

5.7. Discussion

Very few data are available for direct comparison with our results. Those of Erents and McCracken[47] for H_2-targets are only

in qualitative agreement with ours, their thickness dependence
being somewhat different and extending to considerably larger
thicknesses (see Sect. 5.3). The differences in absolute yields
are apparently outside the combined uncertainties of the two
methods, the bulk yield of Erents and McCracken[47] exceeding ours
by two orders of magnitude. There are other indications (see
Sect. 6.3) that their method somehow overestimates the erosion
yields to such an extent. For the erosion of N_2-films only ion-
induced yields are available (Sect. 6.3).

The bulk erosion yields are reasonably well estimated by Eq.
5.1: For bulk D_2 eroded by 2 keV electrons we calculate a value
$Y_{D_2} \simeq 15$ atoms/electron, assuming Eq. 1.4 for $S_{e,e}$ (see Sect.
3.6.2) and estimating β as in Sect. 4.4.ii. This is in very
good agreement with the measured value, $Y_{exp} \simeq 7.8$. Equation 5.1
also predicts a 1.52 times larger yield from H_2, where we found
$Y_{H_2}/Y_{D_2} \simeq 2$. Only for 2 keV electrons incident on N_2-targets
does the equation overestimate the erosion yield by an order of
magnitude. It is not clear whether this is somehow related to
the apparent phase effect in the stopping of keV ions in solid
N_2. We recall that no such effect was found for solid H_2 and D_2.
However, we shall see (Sect. 6.7) that Eq. 5.2 actually esti-
mates Y_{N_2} to within a factor of 2 for MeV $^4He^+$-ions. the elec-
tron-induced erosion yield of H_2 and D_2 might also be estimated
within a simple "ion-explosion" model[47]: If all of the Coulomb
repulsion energy available at the surface due to the first two
ionizations was used for sublimation, this would lead to an aver-
age yield of $Y_{D_2} \sim 20$ for 2 keV electrons, and $Y_{H_2}/Y_{D_2} \simeq 1.5$.

Anyway, both of the above estimates predict an energy-dependent
erosion yield, in contradiction to our observations: The erosion
yield for D_2 was found to vary less than 15% between 1 and 3 keV,
whereas for instance the electronic stopping cross section (and
the ionization cross section) varies by a factor of ~ 2.4 (see
Eq. 1.4). This is, in general, difficult to explain theoreti-
cally, but might suggest contributions from competing mechanisms.
It is interesting to note that for 1-3 keV electrons incident on
solid Ne[14], the erosion yield is closely proportional to $S_{e,e}(E)$

and agrees with eq. 5.1 to within a factor of 2. Actually, at at 2 keV also Y_{Ne}/Y_{D_2} is in excellent agreement with Eq. 5.1.

The thickness dependence of $Y(X_i)$ below ~ 650 Å for D_2 and ~1200 Å for H_2 is independent of energy, and thus of electron range[11]. It is therefore unlikely that the enhanced yield at small thicknesses is caused by electrons reflected from the

substrate. The same kind of behaviour is observed for ion-incidence (Sect. 6.6.4). No explanation is offered here, but we might speculate that the region of thickness dependence is somehow related to some property of the material like transport of heat, charge, etc. If this is so, an investigation hereof might give important information as to the general erosion mechanism also for bulk targets. The importance of the thermal conductivity of the target material is presently under investigation[8].

6. ION INDUCED SECONDARY ION EMISSION AND SPUTTERING

The status of theory for the sputtering of condensed gases in general and of solid hydrogens in particular was described briefly in Sections 5.1 and 5.2. As some theories suggest a relation between ionization and sputtering, we first investigate the emission of positive particles:

The emission of positive particles from bulk H_2 or D_2 may be explained within linear collision cascade theory[29] by assuming an appropriate positive fraction of the emitted particles (Sect. 6.1). In contrast, the emission of positive particles from bulk N_2 is caused predominantly by some other mechanism, possibly reflection (Sect. 6.2).

The experiments on ion-induced sputtering of condensed gases have mainly been made with MeV ions and not particularly volatile target materials (Sect. 6.3). In the few experiments with keV ions and solid hydrogen targets the erosion yields were determined by pressure measurements only.

The present measurements are based on the variation of reflection and secondary electron emission with film thickness (Sect. 6.4). The method is somewhat more uncertain than for electrons (Sect. 6.5), and a beam sweep was not yet available.

We may therefore only present an incomplete set of preliminary results (Sect. 6.6). These may be divided into qualitative results obtained by simple comparisons (Sect. 6.6.1), relative results obtained by keeping critical quantities (mostly the beam) constant and varying other parameters (Sect. 6.6.2) and absolute results (Sects. 6.6.3 and 6.6.4). Of the latter several critical assumptions are necessary for thin films (Sect. 6.6.3) where the erosion may depend both on initial and instantaneous target thickness. In contrast it is argued that for thick films the erosion is independent of initial thickness (Sect. 6.6.4).

As the results are uncertain and preliminary the reliability of the individual types of measurement should be considered carefully (Sect. 6.7). The thickness-dependent region is independent of incident energy (just as for electrons), and the erosion of H_2 is independent of temperature below ~ 3 K. Apparently, the erosion is related to both electronic and nuclear energy loss.

6.1. Positive emission from solid H_2 and D_2

The "positive emission coefficient" γ (defined in Eq. 2.1) was measured as described in Sect. 2.4.i for normal incidence of 4-10 keV H^+, H_2^+, H_3^+, D_3^+, D_2H^+, and $^4He^+$ on bulk targets of solid H_2 and D_2. It should be noted that in the present section γ is expressed as the number of emitted positive particles per incident atom.

The coefficient turns out to be so small that the relative uncertainty on the single points becomes rather large; thus, there was a large scatter of the data. The values for each type of ion were therefore smoothened by fitting them with parabolas.

Fig. 6.1 shows the parabolic fits as functions of the incident energy (in keV/amu).

i) Comparing different ions incident on the same target, the systematics are not obvious: For various hydrogen molecules - H_1^+, H_2^+, H_3^+ - the mutual agreement was good; actually all three sets of data points were equally well fitted by the same parabola. However, $^4He^+$-ions yielded γ-values a factor of about 4 above those obtained with H_3^+-ions, and of a quite different energy dependence. Plotting them instead as function of energy per incident atom (keV/atom) would not improve the agreement much, and plotting them vs. the reduced energy[23] ε (see Sect. 1.1.iii) would make it worse.

Also for D_3^+-ions the values were clearly higher than those for H_3^+-ions, and values obtained with D_2H^+-ions were systematically even higher. It might be of interest to note that for incidence

of 5-10 keV Ne^+-ions on H_2 the γ-values agree with those for H-ions of the same energy per atom.

ii) For incidence of a given ion, the positive emission is systematically ~ 30% larger for H_2- than for D_2-targets. This is seen both for H- and $^4He^+$-ions. For D_3^+- and D_2H^+-ions the indicated difference (Fig. 6.1) is within the statistical uncertainties.
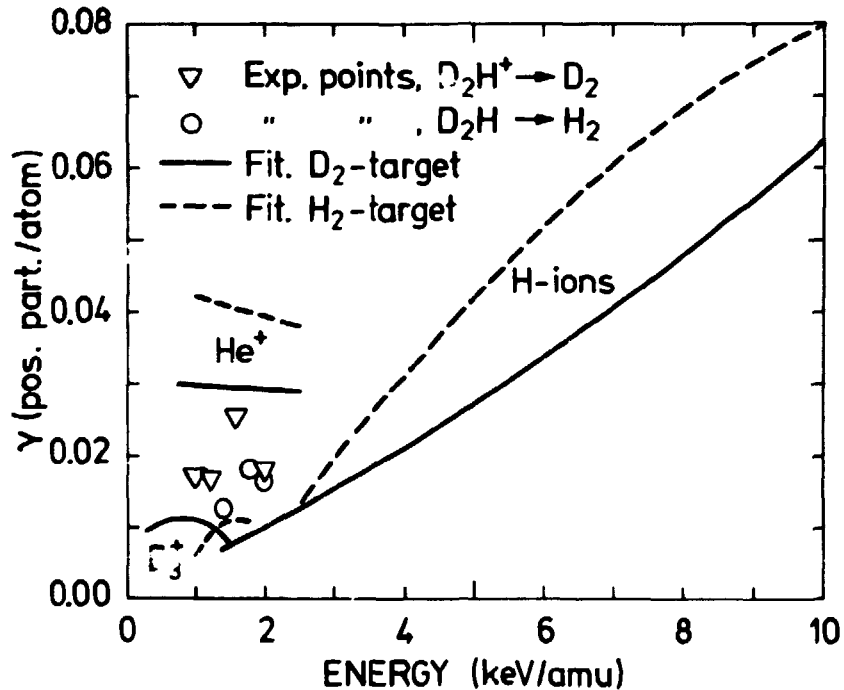

Fig. 6.1. Emission of positive particles from solid H_2 and D_2 bombarded by 4-10 keV H_3^+-, H_2^+-, H_1^+, D_2H^+, and He^+-ions. Emission coefficients γ (Eq. 2.1 b), are given as function of particle energy per mass unit. The curves are parabolic fits to the data points.

The above characteristics suggest that we are observing an on emission of positive sputtered particles. Simple considerations indicate that it is possible to explain both the absolute γ-values and the dependence on energy and target material by means of ordinary sputtering theory[29] (Sect. 1.3.1). It is only necess-

ary to assume an appropriate probability $P^+(v_{out})$ that a sputtered atom of normal escape velocity v_{out} leaves the surface as a positive ion.

For the sake of simplicity let the probability P^+ depend only on the escape energy E_1. Then the differential secondary ion yield $s^+(E_1)dE_1$ is related to the differential sputtering yield $y(E_1)dE_1$ by

$$s^+(E_1) = P^+(E_1)y(E_1) \qquad (6.1)$$

The total secondary ion yield is then

$$s^+ = \int P^+(E_1)y(E_1)dE_1 \qquad (6.2)$$

Now, for the purpose of making an estimate, we consider three situations:

(1) For $P^+ = 1$ the yield S^+ would equal the total sputtering yield Y, which for 1-10 keV H^+ incident on H_2 or D_2 is a strongly decreasing function of primary energy E_0 with Y_{H_2} more than twice as large as Y_{D_2} (Eq. 1.16).

(2) If instead P^+ increased linearly with escape energy E_1, the ion yield S^+ would be proportional to the "reflected energy". This quantity, as estimated from Winterbon's tables[90], is almost independent of primary energy, with $S_{H_2}^+/S_{D_2}^+ \approx 1.5$.

(3) If P^+ was to be proportional to E_1^2, it can easily be shown mathematically that S^+ would increase with primary energy E_0 for the present experiments.

Thus, we may expect that for some P^+ increasing faster than E_1, S^+ will not only increase with E_0 but also have $S_{H_2}^+/S_{D_2}^+ \approx 1.3$. Furthermore, we note that according to Eq. 1.16 the total sputtering yield of solid D_2 is ~ 3 times larger for incidence of $^4He^+$ than for hydrogen-ions of the same velocity (energy per mass unit, see Fig. 6.1).

It should, however, be noted that the sputtering yield for Ne^+ ions incident on H_2 is expected to be much larger than for hydrogen-ions of the same energy, while the positive emission does not differ appreciably.

As for the absolute γ-values, these are easily explained within the sputtering theory by an appropriate choice of P^+ since the total sputtering yields (Eq. 1.16) are at least half an order of magnitude larger. In contrast, reflection of the projectiles is much too weak to explain the positive emission.

6.2. Positive emission from solid N_2

The coefficient γ was also measured for normal incidence of 4-10 keV H_3^+-, H_2^+,- and D_3^+-ions on bulk targets of solid N_2 (Fig. 6.2). The behaviour is quite different from that seen for H_2- and D_2-targets (previous section): γ is a decreasing function of energy, and plotting the values as a function of reduced energy[23] ε (see Sect. 1.1) we find convincing agreement between points obtained with different ions.

In their collection of experimental and calculated reflection coefficients R_N for light ions incident on various targets, Eckstein and Verbeek[126] find the data to scale roughly with ε. If we first fit a general $R_N(\varepsilon)$-curve through all their data, and then normalize this curve to experimental values[159] for protons and deuterons incident on carbon we obtain a curve (broken curve, Fig. 6.2) which agrees surprisingly well with our points.

It thus appears that γ may be explained as caused by reflected projectiles if the positive fraction is near one for most of the exiting particles. In this context "near one" is estimated to mean clearly larger than 0.5.

The assumption of a nearly constant, large positive fraction is not in direct contradiction to the strongly increasing positive fraction assumed in the previous section, since the typical en-

ergies of reflected projectiles are expected to be considerably higher than those of sputtered target particles. In agreement herewith, we recall the behaviour of the energy spectra (Sect. 3.4.i): For bulk N_2 the spectra were found to extend to considerably higher energies (Fig. 3.3) than was the case for hydrogen targets (Fig. 3.4).

Equation 1.16 predicts sputtering yields about 17-25 times as high as the observed γ-values (Fig. 6.2) and of essentially the same energy dependence. Nevertheless, γ may not be explained by ordinary sputtering theory[29] in this case, since Eq. 1.16 also predicts more than 50% higher yields for D- than for H-ions in the present energy region.
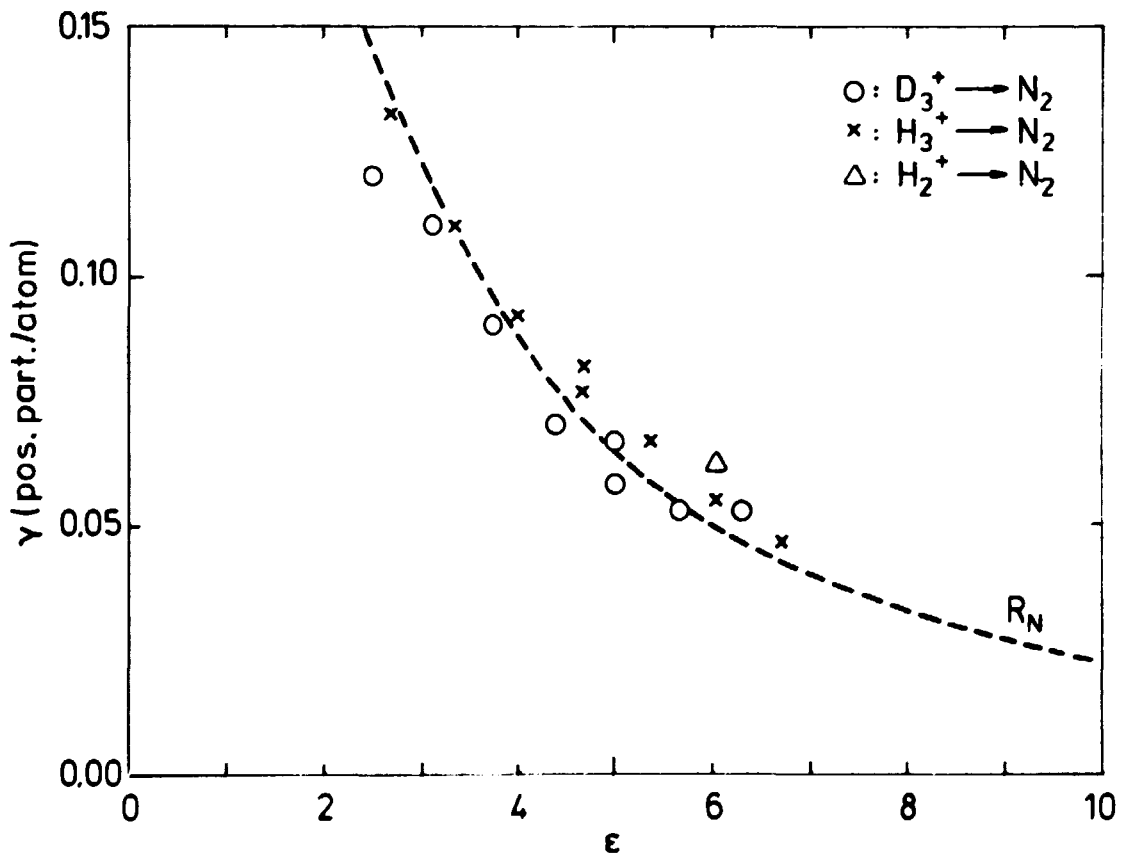

Fig. 6.2. Positive emission coefficient γ (Eq. 2.1 b) vs. reduced energy ε^{23}, for D_3^+-(o), H_3^+-(x) and H_2^+-(Δ) ions incident on solid N_2. Also shown is the estimated reflection coefficient $R_N(\varepsilon)$ (broken curve).

It is curious to note that in contrast it was possible to explain
γ for hydrogen targets by ordinary sputtering theory[29], although
Eq. 1.16 predicts an energy dependence very different from that
of γ (Fig. 6,1).

In conclusion, it appears that for all our targets the positive
emission may be interpreted as caused by sputtering and reflec-
tion, sputtering being the dominant mechanism for hydrogen
targets, while reflection plays a major role for N_2-targets.
However, it seems necessary to assume that a major part of the
projectiles reflected from N_2 are positive, which may be doubtful.

6.3. Ion-induced sputtering

Most experiments on sputtering of condensed gases have been made
with MeV ions. Ollerhead et al.[45] studied the erosion of solid
Xe by 0.3-2.0 MeV H-, He-, N-, and Ar-ions, finding yields up to
$\sim$ 300 atoms/atom. The yield increased strongly with temperature
from 18 to 45 K, and with target thicknesses up to $\sim$ 1400 Å, and
further was found to depend on beam energy, projectile, and sub-
strate. For the lightest projectiles, where S_n is negligible, the
yield scaled with S_e^2, whereas for heavier projectiles it scaled
approximately with S_n. Besenbacher et al.[46] found yields up to
$\sim$ 90 for the erosion of solid Ar by 0.1-3.0 MeV He-ions. The
erosion was here found to be independent of temperature between
6 and 24 K, but to increase with target thickness up to $\sim$ 750 Å.
Nuclear stopping, S_n, was negligible and the yield scaled again
with S_e^2.

Both the above sets of measurements were interpreted in favour
of a thermal spike model (Sect. 5.1).

Brown et al.[43,44,32] investigated the erosion of water ice by
light ions between 6 keV and 1.8 MeV, finding yields between 0.1
and 700 molecules/ion. The yield was independent of temperature
below about 100 K, and of target thickness above $\sim$ 250 Å, and
scaled roughly with S_e^2 for hydrogen and helium ions.

McCracken[160] also studied the erosion of H_2O at 77 K by 5-35 keV deuterons, but found yields about two orders of magnitude larger than comparable data of Brown et al.[32]. We here note that Brown et al.[32] used the well documented method of Rutherford back-scattering of 1-2 MeV $^4He^+$ for monitoring the film thickness, whereas McCracken[160] measured the pressure increase in the vacuum chamber during irradiation and deduced the initial film thickness from the gas inlet assuming a sticking coefficient.

Brown et al.[32] preferred to interpret the erosion of H_2O in terms of an "ion-explosion" mechanism (Sect. 5.1).

Measurements of the erosion of solid N_2 at 4 K by 1-1.8 MeV He-ions[161] gave yields between 235 and 660. The three datapoints given are insufficient to determine an S_e-dependence, but are best scaled with $S_e^{5.3}$. In the same set-up as used by McCracken[160] (see above), Erents and McCracken[162] measured a bulk yield of 5-10 atoms/ion for the erosion of solid N_2, Ar and CO. This is only a factor of ~ 10 larger than our results for 2 keV electrons (Sect. 5.6 and Ref. 9).

The erosion of layers of Kr and Xe by 3-6 keV Ar- and Xe-ions has been studied by energy- and mass analysis of the emitted particles[163]. Estimated yields exceed 10^3, and the energy distri-butions suggest[164] a considerably reduced surface binding energy.

Erents and McCracken[47] were the first to determine absolute yields for the erosion of solid H_2 and D_2 by keV protons, deu-terons, and electrons. They determined the initial yield at the onset of irradiation, and found this to vary with target thick-ness, increasing below ~ 25 Å, decreasing above ~ 1000 Å up to thicknesses comparable with the projectile range. Thin-film yields of up to 10^5 atoms/ion were observed, whereas bulk yields were typically 10^2-10^3. The bulk yield from H_2 would increase by a factor of ~ 3.5 when raising the incident proton energy from 5 20 keV, whereas the bulk yield appeared to be about the same for 5 keV protons and 2 keV electrons.

When comparing these results with our own (Sects. 5.7 and 6.7) we find large discrepancies but note that also these measurements were made in the set-up used by McCracken[160] for the erosion of H_2O (see above).

Using the same technique, Hilleret and Calder[48] found results for the erosion of solid H_2 which essentially agree with and extend those of Erents and McCracken[47]. Both sets of measurements were made at 3.2 K, i.e. near the temperature-dependent regime for H_2 (Sect. 6.7).

6.4. Experiment

The principle is quite analogous to that used for electrons (Sect. 5.4), but the interpretation is somewhat more uncertain, so we start again from the beginning, and notice the differences: Our measurements of ion-ranges (Sect. 3.4.iii) were based on determining the positive emission coefficient γ for light films on an Au-substrate as function of the film thickness ΔX. For incidence of keV light ions $\gamma(\Delta X)$ was found to vary in a characteristic way until the thickness $L_+ \approx R_p/2$ (see Fig. 3.5). This behaviour was interpreted as being caused by projectiles reflected from the Au-substrate, and either leaving the target again themselves in a charged state or inducing a charged emission. In any case it is suggested that one may use a variation in γ to monitor a variation in ΔX - without the mechanism necessarily being quite understood.

Our measurements of γ proceed just as described in Sec. 2.4.i: We monitor i_t^-, and thus γ, continuously as a function of irradiation time.

The present preliminary measurements were made without a beam-sweep (compare Sect. 5.4). Instead the intensity profile of the beam was checked frequently by scanning the beam across the 6 mm aperture of the Faraday cup (see Sect. 2.2.i). By careful focusing a reasonably sharp profile was obtained.

Fig. 6.3 shows the variation of γ with irradiation time for 8 keV D_3^+-ions incident on various films of solid D_2.

One should notice that for the example shown in Fig. 3.5 γ varies with thickness only below ~ 70 Å and above ~ 400 Å. It was found that for very large initial film thicknesses the structure in γ would become totally smeared. It was then possible to exploit the fact, that the secondary electron emission coefficient δ was considerably larger for the Au-substrate, than for H_2 or D_2.

Our measurements of δ proceed just as described in Sect. 2.4.i: We determine i_t^+, and thus δ-γ, continuously as a function of irradiation time. We then used the rather sudden rise in δ to indicate when a film had been eroded away.
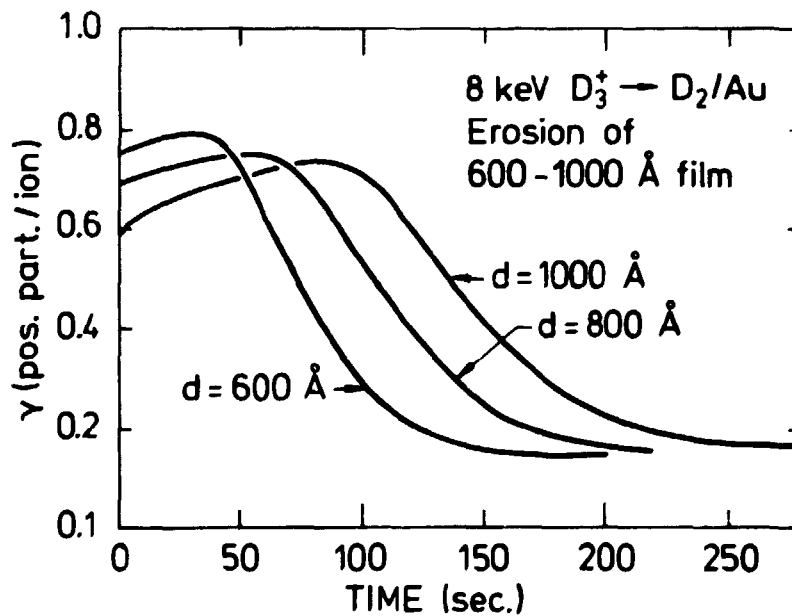

Fig. 6.3. Erosion of 600, 800 and 1000 Å films of D_2. The emission coefficient γ is shown as a function of irradiation time.

6.5. Investigation and discussion

i) An advantage of the present method as compared with that of pressure measurement[47,48] is that it is not concerned with the fate of the eroded particles upon leaving the target, i.e. whether or not these particles are cryo-pumped somewhere else in the chamber, unless of course they recondense on the very beam spot. Recondensation on the target has been mentioned earlier by McCracken[160] as a possibility.

In order to check for such a mechanism, we interrupted the erosion of a 60 Å D_2-film before it was completed. From the known relation $\gamma(\Delta X)$ of Fig. 3.5, the remaining thickness X_i on the beam spot was estimated to be ~ 6 Å. Probing with a pulsed beam at various times after the interruption we could then follow a subsequent "growth" in γ, and thus seemingly in X_i, over several minutes (Fig. 6.4). This growth corresponds to another ~ 6 Å.

The times involved (> 1 min) seem rather large for recondensation. An alternative explanation is that the eroded surface is initially very non-uniform (see Sect. 5.2) with thickness variations of the order of several Å, which are then slowly smoothened out through migration etc. However, if we are indeed observing recondensation, one might expect an even stronger effect during irradiation, which of course could not be measured.

An estimate of such an effect was obtained by assuming that recondensation to be independent of X_i, and extrapolating Fig. 6.4 to time zero. The recondensation during erosion should then be no more than a few per cent of the simultaneous erosion rate. During the following treatment such effects are ignored.

ii) The variation of γ with beam dose over a given thickness range depends somewhat on initial film thickness X_0. This was particularly obvious for thin films, which will be discussed later (Sect. 6.6.2), whereas for larger X_0 the dependence would appear as a slowly increasing "smearing" of the γ-curve: Close inspection of Fig. 6.3 will show that for larger X_0 the γ-curve does
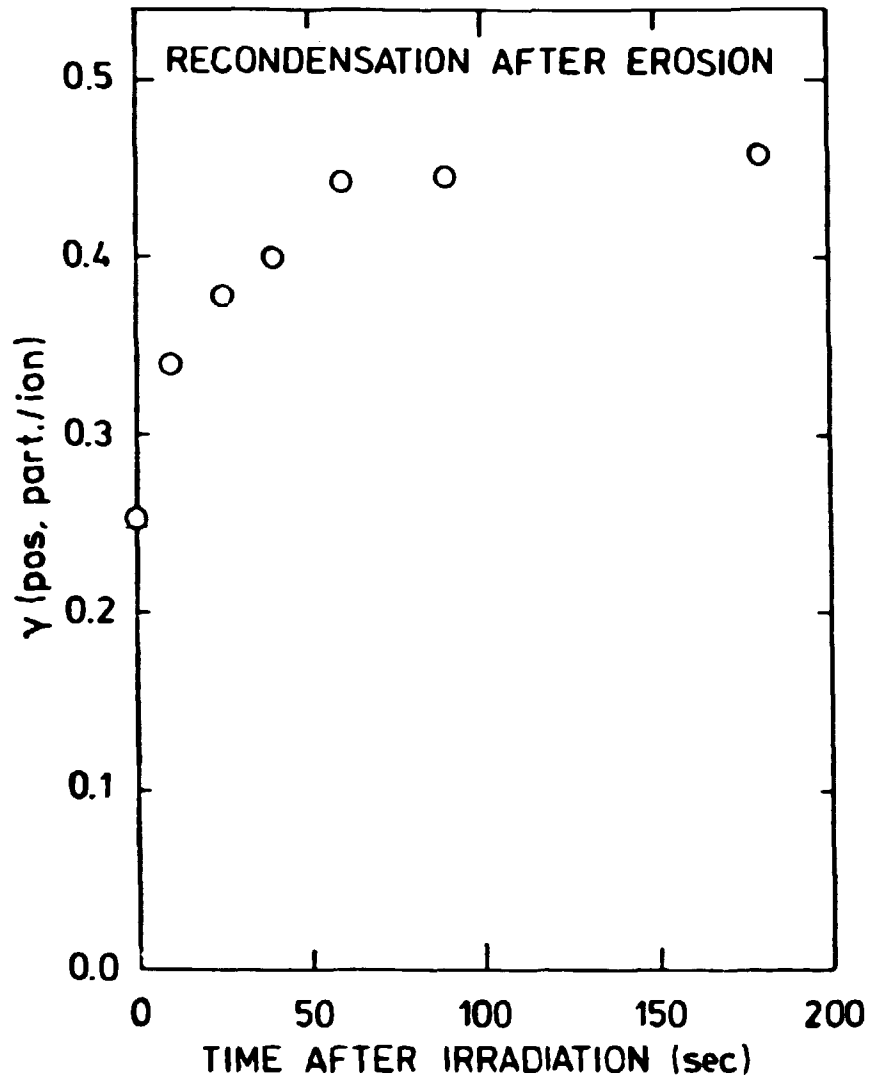
Fig. 6.4. Variation of γ with time after end of irradiation, for a partially eroded D₂-film on Au. Initial thickness 60Å.

not quite reach the maximum value of Fig. 3.5 before falling off towards the "Au-level". For very large X_0 this tendency is followed to the extent that the structure (peak) in the γ-curve disappears almost totally. This probably is caused by inhomogeneous erosion (crater formation etc., see Sect. 5.2 and 5.5.iv).

iii) When bombarding very thick targets with positive ions, and even permitting secondary electron emission (measuring δ) we might expect the targets to charge up positively, and thus in-

fluence the primary beam-energy. However, for any of the applied thicknesses, the observed surface potential (Sect. 2.7.i) would not exceed ~ 75 V. Clearly, when suppressing the secondary electron emission (measuring Y) this charge-up would not be larger.

iv) As discussed in Sect. 3.4.i the positive fraction of the emitted particles is largely unknown. Also the qualitative behaviour of this fraction is difficult to predict, but it seems very likely that it depends on the structure of the target surface. However, if crater formation would have any significant effect on the probability that an emitted particle escapes as a positive ion, then we would not expect that the Y-curve for X_0 = 600 Å (Fig. 6.3) would go through the same maximum as the Y-curve measured with a pulsed beam on an undisrupted surface (Fig. 3.5).

6.6. Results in general

Our data are far from sufficient for a conclusive model of the erosion of solid hydrogens. Instead they may serve to illustrate that indeed the sputtering of solid hydrogens is quite a complex business, as suggested in Sect. 5.2. However, the lack of a basic picture makes it difficult to bring any system into the presentation of our results. As a most important question at any time is the reliability of our interpretations, it was instead decided to present the results according to the number of assumptions and approximations involved. This is done in the following four sections.

Along the way various characteristics will emerge, which we shall try to relate to some physical quantities. The discussion in Sect. 6.7 should, however, probably rather be taken as a resumé of such characteristics than as a real explanation.

6.6.1. Qualitative results

Several factors may interfere with our interpretation of measurements: Recondensation, migration, inhomogeneous erosion (craters), nonuniform beam intensity, variation of charge states, etc., as

discussed above. The safest application of the described method
is therefore to make qualitative comparisons: Bombard various
targets under various conditions with the same beam, and compare
γ-curves.

i) At a substrate temperature of 2.5 K the erosion of 200 Å H_2
is about one order of magnitude faster than the erosion of 200 Å
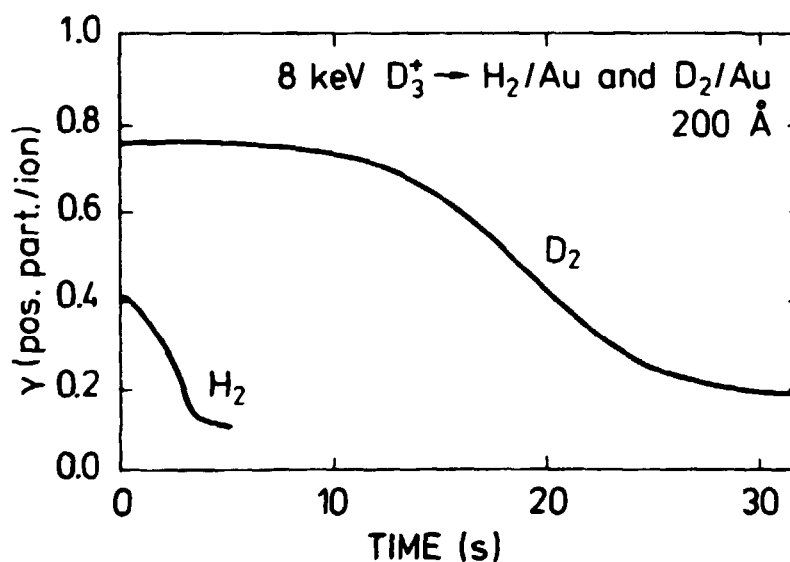D_2 (Fig. 6.5).

Fig. 6.5. Erosion of 200 Å films of H_2 and D_2 at 2.5 K. The
coefficient γ is shown as a function of the irradiation time.

ii) For the erosion of D_2 a peculiar temperature dependence was
observed: For an initial target thickness X_o = 60 Å the erosion
was equally fast at all substrate temperatures between 2.5 K and
5 K, within the experimental uncertainty (Fig. 6.6). However,
for X_o = 200 Å the erosion was clearly faster at the higher tem-
perature. For larger X_o this temperature dependence was even
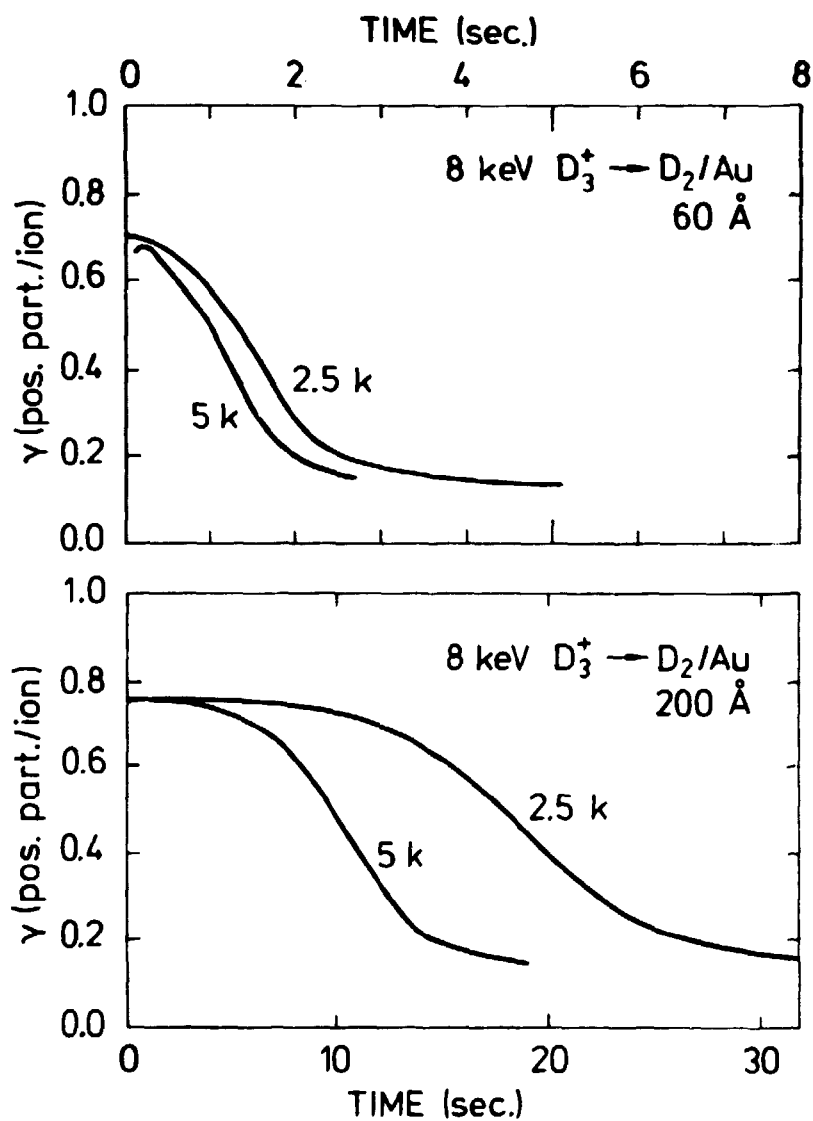stronger than this.

Fig. 6.6. Erosion of 60 and 200 Å D_2-films at different temperatures. The emission coefficient γ is shown as a function of the irradiation time.

6.6.2. Relative results

According to the discussion in Sect. 6.5 (ii and iv) we may assume that as long as the initial target thickness X_0 is not too large, the values of γ are somehow characteristic of the remaining target thickness X_i. We therefore try to interpret our measurements in more quantitative terms:

The erosion rate for any remaining film thickness X_i may be expressed as

$$- dX_i/dt = - \frac{(dY/dt)}{(dY/dX_i)} \qquad\qquad (6.3)$$

where t is the time. We note (Fig. 3.5) that for small X_i the derivative (dY/dX_i) may easily contain rather large errors. However, as it depends on X_i alone, such paroblems may be avoided in relative measurements - simply taking the ratio of erosion rates corresponding to the same X_i-values.

i) Let us first investigate the temperature dependence of the erosion yield Y (Sect. 6.6.1.ii). Using the same beam and the same initial target thicknesses X_0 at various substrate temperatures, many of the possible errors (notably the intensity profile of the beam, craterformation, etc.) may cancel out.

We then determine the ratio $(Y(T)/Y(2.5 \ K)$ of the erosion yield at the temperature T to that at 2.5 K as the corresponding ratio of (dY/dt)-values at the two temperatures (see Eq. 6.3). This ratio may be determined as a function of t or of γ without reference to the relation $Y(X)$ at all. By means of Fig. 3.5 we may now convert this to values of $Y(T)/Y(2.5 \ K)$ vs. remaining target thickness X_i without introducing any errors in the ratio, and only small errors in X_i.

In this way it was found that the temperature dependence varies with remaining thickness X_i in a surprising manner (Fig. 6.7): The temperature dependence is strongest at rather small X_i ($\sim$ 10 Å). This should be compared with the observation that the overall temperature dependence was strongest for the largest initial thickness X_0 (see Sect. 6.6.1.ii).

ii) Quite analogously one may compare the erosion yields at some remaining thickness X_i corresponding to different initial thicknesses X_0, i.e. investigate whether $Y(X_i)$ depends on prior erosion. However, here the homogeneity of both beam and erosion process may become important.

Optimizing the beam profile carefully we determined the ratio $Y(X_i,X_0')/Y(X, 200 \ Å)$ of the erosion yields for various initial

TEMPERATURE DEPENDENCE OF YIELDS
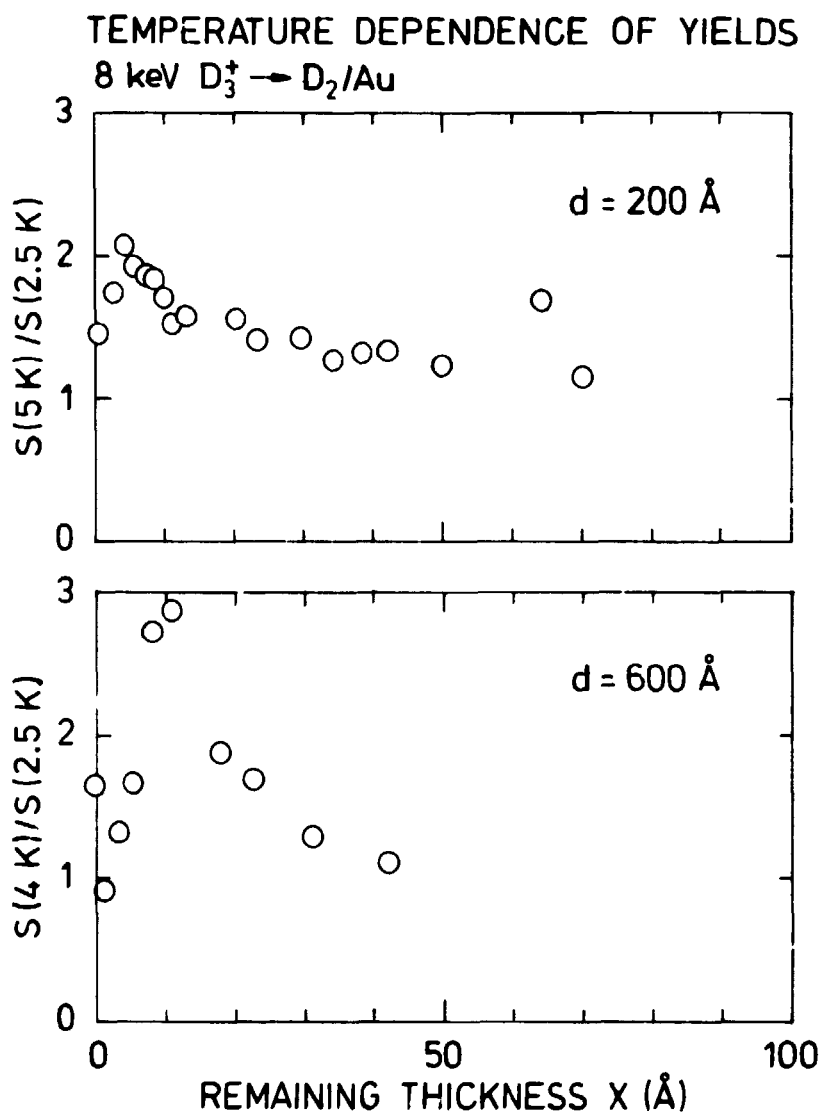$8 \text{ keV } D_3^+ \rightarrow D_2/Au$

Fig. 6.7. The temperature dependence of the erosion yields for 200 and 600 Å D_2-films. The yields at 5 and 4 K are shown relative to the yields at 2.5 K as functions of the remaining target thickness X_i.

target thicknesses X_o' relative to that for $X_o = 200$ Å. This ratio was determined for $X_o' = 60$ Å and $X_o' = 130$ Å as function of remaining thickness X_i (see Fig. 6.8). We recall that actually $(d\gamma/dt) \neq 0$ for $X_i < 70$ Å (Fig. 3.5). It appears from Fig. 6.8 that the erosion of the last ~ 40 Å was slower for larger X_o! As we shall see below (Sect. 6.6.3.ii), this is near the region where we may be reaching the substrate on parts of the beam spot, so we cannot exclude that this is simply an effect of inhomogeneous erosion (crater formation).
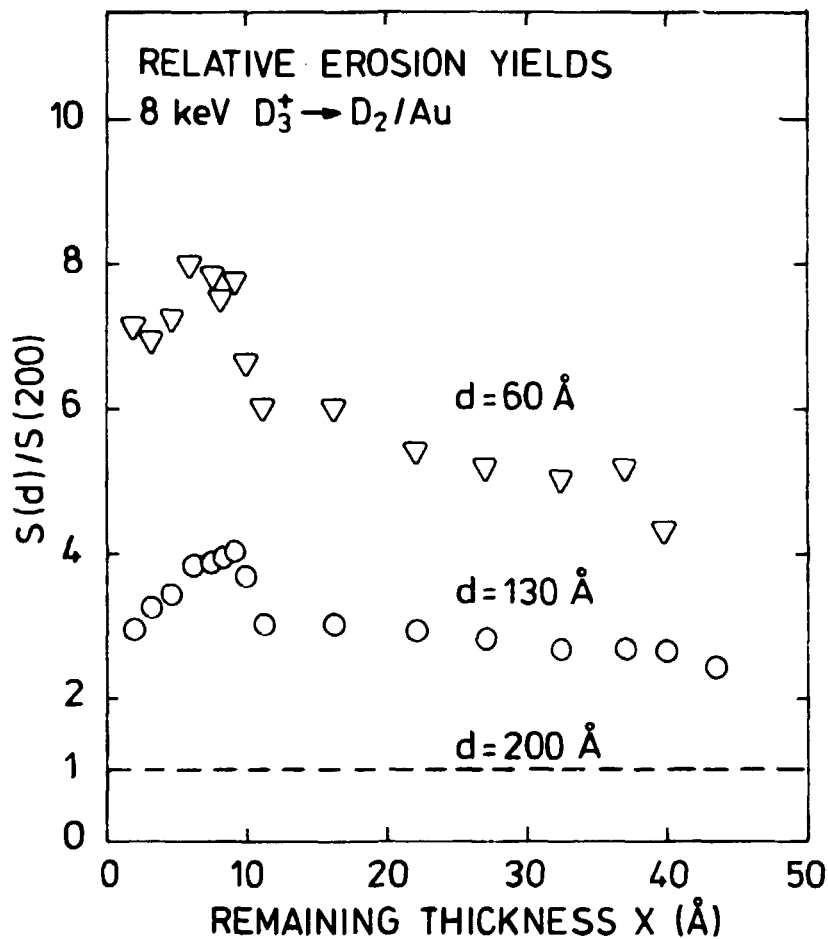
RELATIVE EROSION YIELDS
8 keV $D_3^+ \rightarrow D_2/Au$

d = 60 Å

d = 130 Å

d = 200 Å

S(d)/S(200)

REMAINING THICKNESS X (Å)

Fig. 6.8. Erosion yields at 2.5 K for films starting
at X_0 = 60 and X_0 = 130 Å relative to the yields of a film
starting at X_0 = 200 Å. The yields are shown as functions
of the remaining thickness X_i.

iii) Comparing two different target materials we note that the
$Y(X_i)$-curves are no longer identical. Instead we simply note,
how long it takes a given beam to erode various films away. In
this way we still maintain the experimental advantage that the
beam conditions are identical in our comparisons.

One might expect that for thin films, particles or energy reflec-
ted from the substrate would contribute to the erosion. In vari-
ous materials, however, the beam has, of course, different range
distributions, so in order to keep the relative contribution
from reflection constant in our comparisons, we use only films
of thicknesses much smaller or much larger than any of the beam

ranges, R_p. Fortunately, the ranges do not differ very much be-
tween H_2 and D_2.

It was seen above (Sect. 6.6.1.i) that 8 keV D_3^+ will erode thin
H_2-films considerably faster than the corresponding D_2-films.
Let us try to investigate this a little:

The incident D_3^+-ions are expected to dissociate immediately at
the target surface (see discussion in Sect. 3.4.ii) and have
ranges of ~ 3000 Å in H_2 and ~ 3950 Å in D_2 (Sect. 3.5). For very
thin films ($X_O \ll R_p/2$) this difference in range is probably of
minor importance (see above). Comparisons for several thin films
gave an average ratio $Y_{H_2}/Y_{D_2} \simeq 9$ between the yields for 8 keV
D_3^+ within confidence limits of ~ ± 30%. However, it is important
to notice that the ratio decreases with increasing film thickness
(see Sect. 6.7.iii).

Erosion measurements with $^4He^+$-beams were somewhat more difficult,
because the structure in the $Y(X)$-curve is considerably smaller.
However, a few comparisons were made for 8 keV $^4He^+$ incident on
very thin films of H_2 and D_2, suggesting again a difference of at
least an order of magnitude between the erosion yields.

iv) Comparing instead the effect of different beams in a given
target, we must now try to ensure that indeed the beams are com-
parable. We have attempted to obtain roughly the same beam pro-
files and intensitites, measuring always the number of incident
atoms, also for molecular beams.

Unlike above, we now have an advantage in the interpretation of
the results: Once the energy is deposited by the beam, the further
dissipation, erosion, etc. depends only on the target material.
This means that we may now simply observe the effects of various
primary energy distributions in the target.

Theoretically, 8 keV $^4He^+$ have a range of ~ 4800 in D_2, i.e. for
very thin films we may also try to compare this with an 8 keV
D_3^+-beam: Apparently the He-beam gives about 4 times as high an
erosion yield.

However, previous measurements of H. Sørensen[165] for 9 keV N^+-ions incident on D_2 suggest a yield at least 2.5 times higher than obtained for 8 keV $^4He^+$, although the electronic stopping cross sections are almost identical! It should be noted, of course, that the range of N^+-ions is considerably shorter, but still it seems more likely that the larger erosion yield is somehow related to the ~ 14 times higher nuclear stopping cross section.

Further comparisons are presented in Sect. 6.6.4, but for now we note that according to H. Sørensen[165] a 6 keV N_2^+-beam gave essentially the same erosion yields per incident atom as the 9 keV N^+-beam for several thin films, although the electronic stopping cross section is reduced to ~ 60% of the 9 keV value. The nuclear stopping cross section, on the contrary, is increased by ~ 40%, so perhaps the two variations cancel out in this case? We do recall, though, that results obtained with N_2^+-beams may be questionable (Sect. 2.2).

6.6.3. Absolute results, thin films

Just as for electrons (Sect. 5.6) absolute erosion yields Y may, in principle, be obtained in two different ways. However, this time the situation is more complicated:

i) Following, for instance, the erosion of a film of 60 Å D_2 by 8 keV D_3^+-ions (Fig. 6.6), we see γ reach its final (substrate-) value in ~ 2.5 sec, i.e. the average erosion rate is $(dX/dt)_{av}$ ~ 24 Å/sec. By means of the estimated intensity profile of the beam (Sect. 2.2.i), this is readily converted to an absolute erosion yield Y_{av} ~ 1200 atoms/atom. In agreement with Sect. 6.6.2 the corresponding yield for 60 Å H_2/Au was ~ 10^4, while 8 keV H_3^+-ions incident on 60 Å H_2/Au gave Y_{av} ~ $5.5 \cdot 10^4$ at/at. We may also note, that H. Sørensen[165] reports a yield of ~ 10^4 for 9 keV N^+-ions incident on 50 Å D_2/Au.

This approach is based on a minimum number of assumptions, but does not necessarily lead us very far. Unlike for electrons (Sect. 5.6), the instantaneous erosion yield $Y(X_i)$ appears to

depend on the initial film thickness X_0 (Sect. 6.6.2.ii). If this is really true, we may not determine $Y(X_i)$ from a plot of X_0 vs. total erosion dose D_0 as was done in Sect. 5.6 .

For thick films (Sect. 6.6.4) the situation looks better.
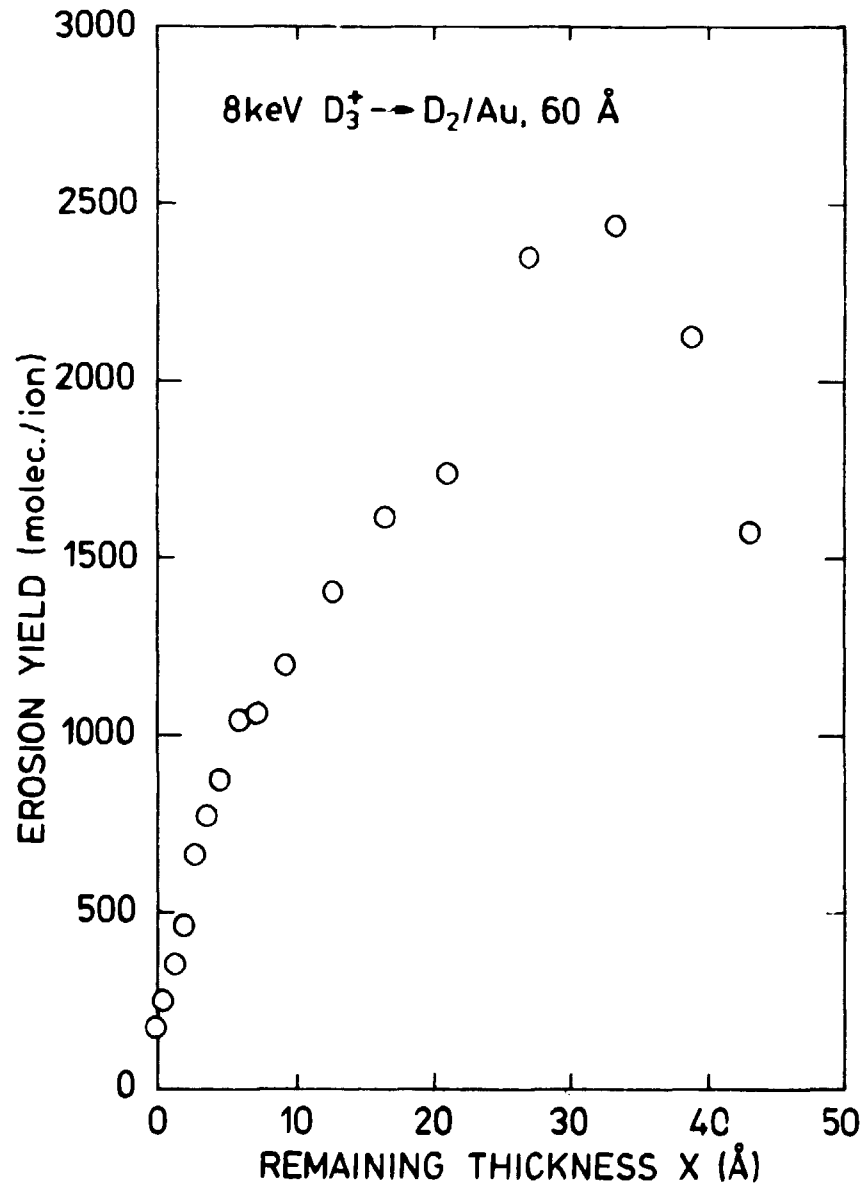

Fig. 6.9. Absolute erosion yield at 2.5 K during erosion of a 60 Å D_2-film shown as a function of the remaining thickness X.

ii) Making several more assumptions we may perhaps extract additional information from the γ-curves. As an example, we consider again the 60 Å-curve of Fig. 6.6. Deriving $(d\gamma/dX)$ from Fig. 3.5 by numerical differentiation of $\gamma(X)$, we may evaluate the erosion rate (dX/dt) as a function of remaining thickness X_i (Eq. 6.3). Converting this to an absolute erosion yield $Y(X_i)$, we see (Fig. 6.9) that Y varies strongly with X_i, having a maximum of the order of 1600 atoms/atom at $X_i \sim$ 30 Å. The existence of this maximum is easily understood: Assume that an 8 keV $D_3{}^+$-ion causes the ejection of 4800 D-atoms from a planar surface creating a hemispherical crater. Then the radius of this crater would be $\sim$ 34 Å!

The differentiation introduces a rather large uncertainty, and the results depend on the absolute γ-values observed. The error may be estimated by comparing to the Y_{av} determined above without reference to absolute γ-values, etc.: Averaging over the instantaneous yields $Y(X_i)$ of Figure 6.9 we obtain an average erosion yield $< Y > =$ 900, i.e. a deviation of $\sim$ 25%.

Thus, we must be careful when evaluating results like Fig. 6.9, but it seems reasonable to believe the general tendency. We know that for larger initial thicknesses X_O the erosion of the last 40-50 Å at least appears to be slower (Sect. 6.6.2.ii), but unfortunately for larger X_i (up to $\sim$ 400 Å) the derivative $(d\gamma/dX)$ is essentially zero, so we get no further this way.

6.6.4. Absolute results, thick films

Under various assumptions it was found in the previous sections that for thin films the erosion yield Y apparently depends on both initial (X_O) and instantaneous (X_i) film thickness. As long as we do not fully understand such a thickness dependence, however, it is impossible to predict whether this also extends to larger thicknesses. For large X_O the structure in the γ-curve becomes "smeared" (6.5.ii) and we may no longer interpret the derivatives $(d\gamma/dt)$ as used in Sects. 6.6.2 and 6.6.3. Thus we are left with only one possible approach: We measure the time it takes to erode a film away (6.6.2.iii and 6.6.3.i). However,

in order to determine any values of $Y(X_i)$ from such measurements, we need Y to be independent of X_0.

Fig. 6.10 shows a series of results in the form recognized from Sect. 5.6 : The initial film thickness X_0 vs. total beam dose D_0 necessary to erode the film away, for 8 keV H_3^+ incident on H_2. The observation that for $X_0 > R_p/2$ we obtain a straight line supports the assumption that at least in this region the erosion is independent of X_0. It would be unreasonable to expect that the X_0- and X_i-dependences would somehow counteract each other to give a straight line. Thus, we may determine a "bulk" erosion yield, just as in Sect. 5.6.
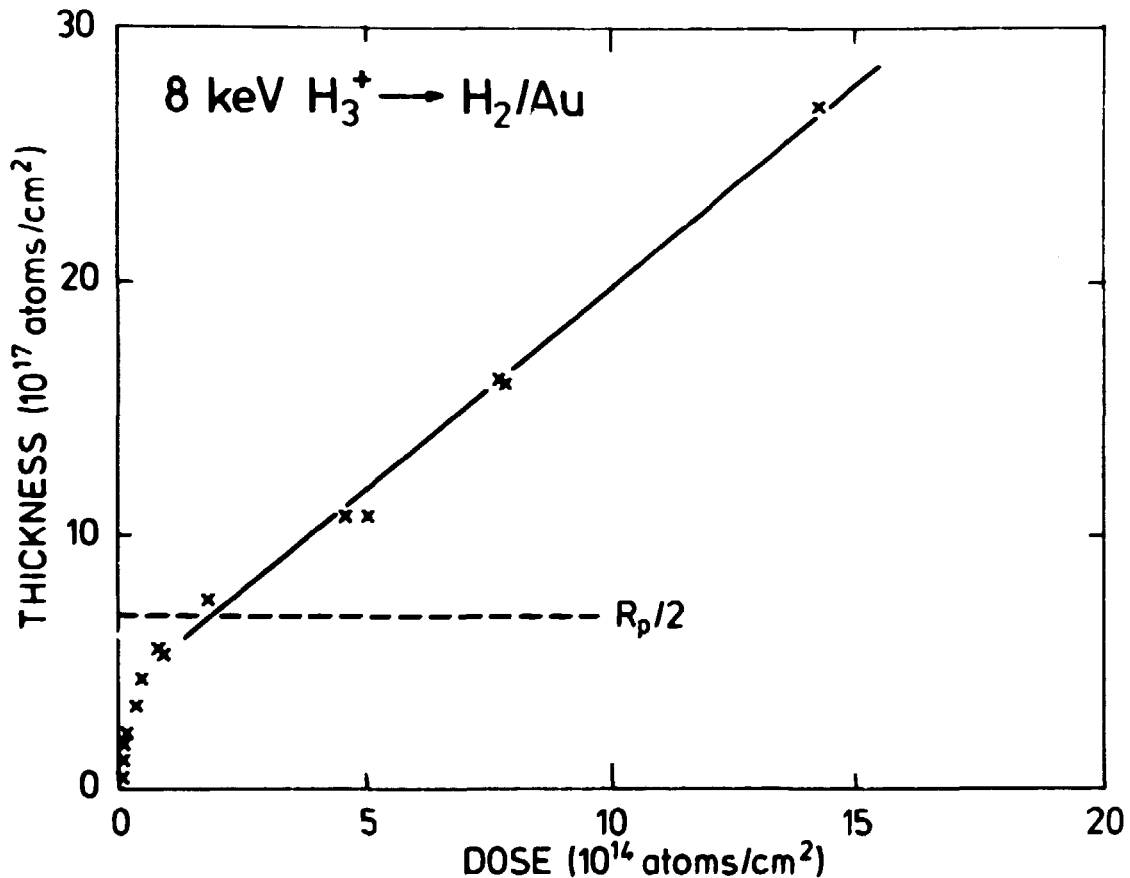

Fig. 6.10. Initial film thickness X_0 vs. total dose D_0 of erosion, for 8 keV H_3^+ → H_2/Au. Solid line: Fit through (D_0, X_0) points for $X_0 > R_p/2$.

Varying the projectile-range almost an order of magnitude (the difference between 3 keV D_3^+- and 8 keV $^4He^+$-ions, see also below) apparently did not change the thickness dependent region significantly, i.e. the agreement with $R_p/2$ above seems to be accidental. Fig. 6.11 shows a set of bulk erosion yields Y_∞ for various ions incident on solid H_2. The error bars are estimated from the linearity of $X_0(D_0)$ and the quality of the eroding beams, and should serve only as indications of relative un-certainties. Not only are the absolute yields very uncertain, as discussed above, but when comparing yields obtained with dif-
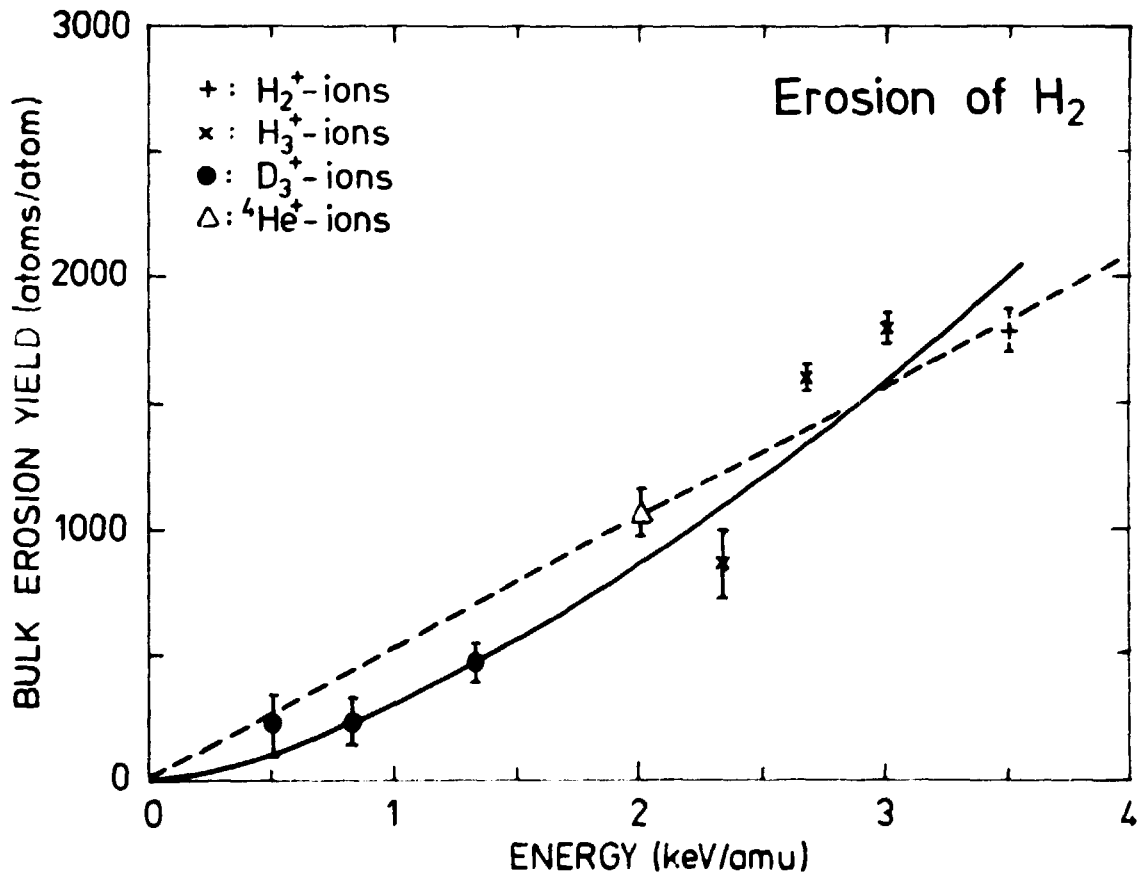

Fig. 6.11. Erosion of solid H_2 by H_2^+-(+), H_3^+-(x), D_3^+-(●) and $^4He^+$-(△) ions. Bulk erosion yields per incident atom vs. energy per mass unit. Best power curve fit (solid curve) is $Y_\infty \propto E^{1.5}$. Shown for comparison is best linear dependence $Y_\infty \propto E$ (broken line).

ferent beams the relative uncertainties may be substantial. However, let us still try to extract some characteristics from Fig. 6.11:

We note first that apparently there is no large difference between using H_2^+- and H_3^+-ions. Unfortunately, we have not yet been able to get good low-energy results for H_1^+-ions.

Considering the energy dependence we first ignore the point obtained with 8 keV $^4He^+$-ions, and fit the rest of the points with a power dependence on energy E. This leads to a yield proportional to $E^{1.5}$ (full curve), which might suggest that $Y_\infty \propto S_e^3$. One should not put too much emphasis on this, but it does appear to fit the points better than an S_e^2-dependence (broken line).

Whether or not the 8 keV $^4He^+$-point agrees with some S_e^n-dependence, of course, depends on the value assumed for S_e in this case. Unfortunately, the structure in the γ-curve was too small to allow any range measurements for $^4He^+$ in solid H_2. Despite the results of Sect. 4.2.i, we put more trust in the stopping cross sections of Ziegler[101] (see arguments of Sect. 4.2.i), i.e. $S_e = 1.45 \cdot 10^{-15}$ eVcm^2/atom for 8 keV $^4He^+$.

Plotting our Y_∞-values vs. S_e (Fig. 6.12), we see that the $^4He^+$-point falls clearly outside a monotonic dependence of Y_∞ on S_e. Clearly, this is far from sufficient to permit any kind of conclusions, but it is interesting to observe that if we plot instead Y_∞ vs. the sum S_{tot} of S_e and the nuclear stopping cross section S_n (Eq. 1.14), then also the $^4He^+$-point falls nicely into place (Fig. 6.13). The curve is a power curve fit (this time including the $^4He^+$-point) yielding $Y_\infty \propto S_{tot}^{4.3}$, but since the S_{tot}-range fitted is rather small this power is determined largely by the demand that a power curve must go through origo.
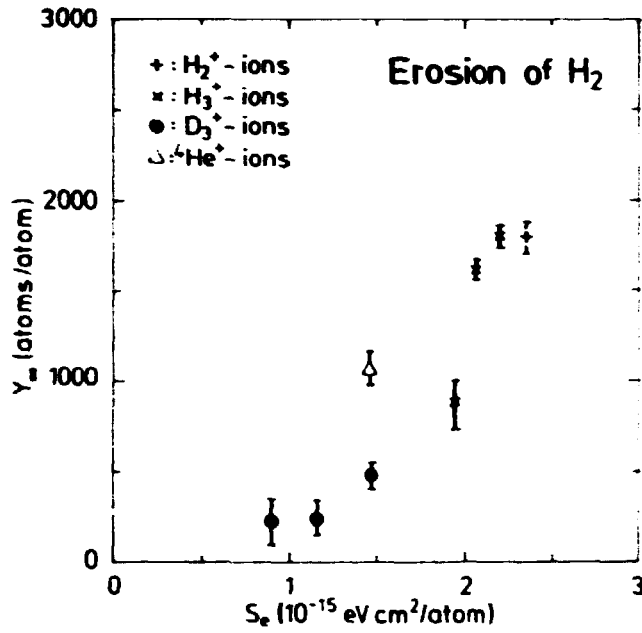
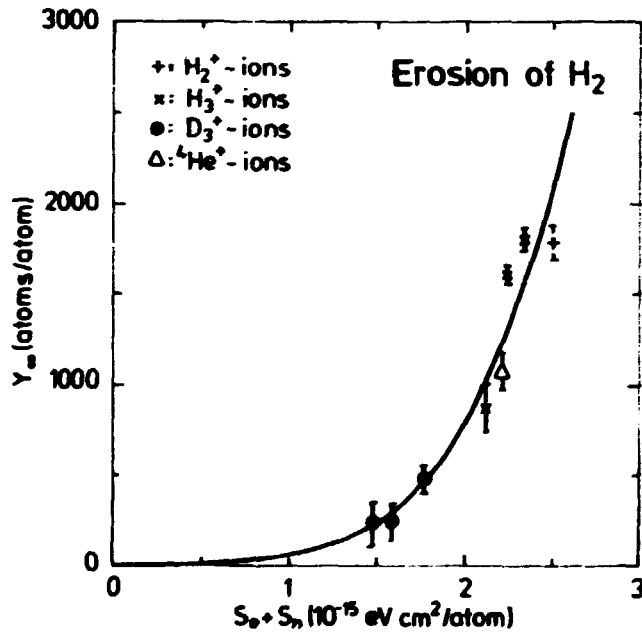Fig. 6.12. Erosion of solid H_2 (see Fig. 611). Bulk erosion yields vs. electronic stopping cross section.

Fig. 6.13. Erosion of solid H_2 (see Fig. 6.11). Bulk erosion yields vs. total stopping cross section $S_{tot} = S_e + S_n$. Also shown is power curve fit $Y_{\infty} = S_{tot}^{4.3}$.

6.7. Discussion

The reader is reminded again that the above results are only pre-
liminary, and that many investigations could not be made as long
as we did not have a beam-sweep (compare Chapter 5). For now we
must therefore consider carefully the reliability of our results,
before drawing any kind of conclusion.

i) For thin films the erosion yield Y varies with remaining
film thickness X_i, being largest for small X_i. This kind of be-
haviour was also observed with electrons (Sect. 5.6), but for
ions it cannot be excluded that Y varies also with initial film
thickness X_0, i.e. that the yield depends on prior erosion.

Apparently, for thick H_2-films the yield becomes independent of
X_0. Thus, for large X_0 we may observe the variation of Y with X_i:
$Y(X_i)$ varies up to a thickness of the order of $7 \cdot 10^{17}$ atoms/cm^2
(~ 1300 Å), above which it becomes constant ("bulk yield"). As
we observed for electron induced erosion, the thickness-dependent
region is apparently independent of projectile range. This sup-
ports the suggestion (Sect. 5.7) that the thickness dependence
is related to some property of the target material.

Other authors also found the thickness dependent region to be
independent of energy (and thus of range) for 5-20 keV protons[47]
and 0.5-10 keV H_2^+-ions[48] incident on H_2-films. For D_2-films a
somewhat smaller thickness-depe dent region is found[47], but in
both cases their thickness dependence extends out to $\sim 10^{19}$
atoms/cm^2 or further, i.e. over ten times as far as ours. The
same disagreement was found for incidence of electrons (Sect.
5.7).

The observation of thickness-dependent regions of ~ 750 Å in
Ar[46] and ~ 1500 Å in Xe[45] eroded by MeV ^{4}He-beams may be related
to an independent phenomenon. Unlike ours these experiments show
yields increasing with thickness, except for a rather special
case using an SF_6-substrate[45]. Also unlike ours they applied sub-
strates that were lighter (lower Z) than the target films, they
did not consider "bulk" (thicker than $R_p/2$) films, and reflec-

tion from the substrates was negligible. It might be of interest to note that measurements with keV electrons incident on Ne[14] also show yields to increase with film thickness up to a few hundred Å.

ii) The erosion of a given film is enhanced by heating the substrate sufficiently. For thin films this temperature dependence grows stronger with initial thickness X_o, which might be explained by the temperature of the target surface increasing with distance from the (cooling) substrate. However, at the same time there are indications that for a given X_o the temperature dependence is strongest at the end of the erosion, i.e. for the smallest X_i. If this is really true, the temperature dependence becomes rather difficult to explain. We might suggest that this behaviour is perhaps related to the thickness dependence of the erosion yield also in the "temperature-independent" region.

Of course, the erosion is probably temperature dependent at all temperatures, but below ~ 3 K this dependence was within the experimental uncertainty even for H_2 (the most volatile of our targets). Needless to say, our results (below) are all measured below ~ 3 K, unless otherwise specified.

iii) The erosion of thin H_2-films by D_3^+- and $^4He^+$-ions was roughly an order of magnitude faster than the erosion of D_2-films of the same thickness. The large difference might partly be related to the fact that the thickness dependent region is somewhat larger for H_2[47] (Sec.. 5.6), i.e. we should probably not compare identical thicknesses. We recall (Sect. 6.6.2.iii) that the ratio Y_{H_2}/Y_{D_2} was seen to decrease with film thickness. Unfortunately, we do not yet have bulk erosion yields for D_2.

Without claiming any particular quantitative validity of the primitive estimate in Sect. 5.2 we might note that both the thermal diffusivity (Table 1.1) and the "range" of secondary electrons[18] is lower in H_2 than in D_2, while molecular excitation energies are higher. Thus, a larger erosion yield could perhaps be explained by a higher energy density and a lower binding-energy?

If indeed the electronic stopping cross section for deuterons was considerably smaller in D_2 than in H_2 (as indicated in Fig. 3.21), this might of course explain the larger erosion yields, but this difference is still believed to have a different origin (Sect. 3.5.6). The stopping cross sections for $^4He^+$-ions were not measured. Thus, in a future comparison of bulk yields one should use H-ions.

iv) Apparently, the erosion is somehow related to both the electronic (S_e) and the nuclear (S_n) stopping cross sections, or rather to the energy initially deposited in the electronic system as well as in nuclear motion. This is hardly surprising (Sect. 1.3).

The erosion of bulk H_2 appeared to increase strongly with the total stopping cross section $S_{tot} = S_e + S_n$ for a variety of ions (Fig. 6.13). Of course S_n was in all cases the smaller of the stopping cross sections, but we note that the same behaviour has been observed for nitrogen ions incident on solid D_2, where S_n is dominant: The yields (per atom) were essentially the same for 9 keV N^+- and 3 keV/atom N_2^+-ions incident on thin D_2-films, in agreement with a difference of only ~ 15% in S_{tot}. However, we may not conclude that there is a simple relation between Y and S_{tot}, only that apparently both S_e and S_n may influence Y.

Thus 8 keV $^4He^+$-ions would erode thin D_2-films considerably faster than would 2.67 keV/atom D_3^+-ions, although the electronic stopping cross sections are almost identical and S_n is only a small part of S_{tot} for both.

In contrast to the above, the electron-induced erosion of D_2 was found to be independent of S_{tot} between 1 and 3 keV (Sect. 5.6). Thus, we may well ask ourselves: What is the most obvious difference between the two cases? Two characteristics might here be noted for the electrons: 1) the nuclear stopping is almost negligible, and 2) the stopping cross section (S_{tot}) is a factor of 3-10 lower. Furthermore, the spectrum of secondary electrons becomes "harder", which might also influence the initial energy density (Sect. 5.2).

It may be worth noting that Ollerhead et al.[45] found 500 keV
protons to erode solid Xe at least a factor of ten faster than
230 eV electrons having a similar ionizing efficiency. These
authors also find that S_n plays a very significant role in the
erosion mechanism as soon as it is just a few per cent of S_{tot},
a behaviour which may at least be qualitatively understood[45] in
a thermal spike model (Sect. 5.1.iii). Clearly, this does not
necessarily mean that our results are in support of such a model.

v) The emission of positive particles from bulk targets could
be explained within linear collision cascade theory by assuming
a strongly increasing positive fraction $P^+(E_1)$ for emitted
particles (Sect. 6.1). In contrast, the total erosion yield Y
may clearly not be explained within such a picture (see above).
However, such different behaviours are not necessarily in con-
tradiction to each other[152]: The erosion yield is probably deter-
mined by particles of energies below a few eV, whereas almost
all positive particles are emitted with energies above ~ 50 eV
(see Fig. 3.4). Thus, we expect essentially no overlap between
the two groups of particles.

However, another possibility should be considered: If the
erosion is actually caused by "ion explosions" (see Sect. 5.1.i)
the positive emission might perhaps be directly related to the
total erosion yield Y. The emission of many molecules in the
form of charged clusters ranging from H_5^+ to at least H_{99}^+ has
been observed previously for electron bombardment of solid H_2[151],
and if most clusters are being neutralized while leaving the
target surface, a relation could be possible. However, unlike Y,
the positive emission coefficients γ for a given target do not
vary monotonically with S_e or S_{tot} (compare Sect. 6.6.4).

On the other hand, this does not mean that our results are in
contradiction to an "ion-explosion" model (see Sect. 5.1.i).

vi) The absolute erosion yields measured are very uncertain, but
clearly very large. Other authors[47,48] report bulk erosion yields
of about a factor of ten lower than ours, at comparable energies.
This difference should be outside our experimental uncertainty,

and may perhaps be somehow related to the fact that they do not reach "bulk" conditions until considerably larger thickness (as mentioned above). Thus their yields decrease by a factor of ~ 100 above 10^{18} atoms/cm^2, i.e. in the region where we argue to have already "bulk" yield (see Fig. 6.10). For very thin films (~ 60 Å H$_2$, see Sect. 6.63) we are all in good agreement, but here our uncertainties are larger, and the different substrates may play a role[47,48,160].

We recall that for electrons incident on H$_2$-targets, Erents and McCracken[47] found bulk yields about hundred times as large as ours (Sect. 5.7). Also there are other indications (see Sect. 6.3) that their method might somehow overestimate the erosion yields to such an extent.

vii) Unlike for electrons, the bulk erosion yields for ions are not well estimated by Eq. 5.1: The experimental yields are a factor of 15-75 larger, and show a clearly stronger energy dependence (Fig. 6.11).

In any case, the erosion yields observed are so large that we should rather compare them to Eq. 5.2. The "active" depth h is estimated[33] by assuming that the average experimental yield Y_{exp} corresponds to the formation of hemispherical craters of radius h. As h thus increases with energy, Eq. 5.2 predicts a stronger energy dependence ($\sim E^1$) than does 5.1, in reasonable agreement with experiment. The fact that Eq. 5.2 still underestimates Y_{exp} by a factor of 10 might partly be explained by the inevitable formation of large craters, which increase the surface area exposed to the beam[33] and probably reduce the surface binding energy as well (see Sect. 5.2). Together with the possibility of cluster emission these effects may easily explain a discrepancy of a factor of ~ 10, but certainly the results of this chapter may not be taken as support for Eqs. 5.1 and 5.2.

It is quite curious to note that Eq. 5.2 underestimates the erosion of solid N$_2$ by 1-1.8 MeV ^{4}He$^+$-ions[161] by only a factor of 2, while Eq. 5.1 was unable to predict the yield for 2 keV electrons incident on N$_2$ (Sect. 5.7).

7. RESUMÉ

This chapter contains only a resumé of the most significant conclusions. For justifications hereof and further results the reader i. referred to the individual chapters, especially their first and last sections.

i) Stopping theory: Apparently the theory of Lindhard and Scharff[20] (eq. 1.7) predicts the electronic stopping of keV ions in <u>gaseous</u> H_2 and N_2 quite well, despite the violation of various assumptions. For 1-3 keV electrons in H_2, D_2, and N_2 the electronic stopping is described by Bethe's formula[15] (Eq. 1.4) to within ~ 10%.

ii) Phase-effect: For keV ions in solid H_2 and D_2 the stopping is closely the same as in gaseous targets. In solid N_2 the electronic stopping cross section is only about half as large as in N_2-gas. This effect was found by three independent methods. For electrons no phase-effect was found.

iii) Secondary electron emission: Cascade theory is not likely to be valid in our cases, but qualitative and relative statements may still be made on the basis of Eq. 1.18.

iv) Erosion: A theoretical description is not yet available, but the erosion seems to be determined essentially by (surface) binding energies and electronic stopping. For slow ions also nuclear stopping is probably important. The applicability of the sublimation energy U_0 as an estimate of surface binding is uncertain, and estimates based on planar target surfaces are certainly wrong, at least for the highest erosion yields.

A comparison between results for slow (keV) ions and fast (keV) electrons is bound to show numerous differences, but certain characteristics were retained: The erosion was thickness dependent up to some film thickness which was a charac-

teristic of the target material but independent of projectile. It was independent of temperature below ~ 3 K for H_2 and ~ 3.5 K for D_2, and apparently independent of beam intensity at the present low intensities.

Typical yields from bulk H_2 are ~ 15 atoms/electron for 2 keV electrons, and ~ 800 atoms/atom for 2 keV protons.

> "There are many things, the knowledge
> of which is of little or no profit
> to the soul".
>
> (Thomas á Kempis)

8. ACKNOWLEDGEMENTS

During the past almost 3 years I have found him ever ready with all sorts of practical advice, also when I needed it. Much of this work, though, would still have been impossible without the initiative and competence of Arne Nordskov, Hans Skovgård and Bjarne Sass. The quiet and polite assistance of these three gentlemen is respectfully acknowledged.

The participation of Chen Hao-Ming in essential parts of the experiments was also appreciated.

Thanks are also due to Knud Weisberg, Jens Knudsen and Klaus Bormannn for their help in designing and building various electronic parts, and of course to the Physics Department at Risø for showing me patience during the completion of this thesis..

I would like to thank H. Verbeek, P. Dahl, P. Hvelplund and E. Horsdal for helpful advice concerning the electrostatic analyzer, W. Eckstein for the computer simulations of the reflection from Xe, and P. Sigmund, M. Inokuti, Mourits Nielsen, and the Garching-group for various valuable discussions.

Finally, I wish to express my profound appreciation to Jørgen Schou, who would respond with the patience of a dziggetai whenever my naive questions dragged him away from his ceaseless preparation of ref. 6 - to Vagn Jensen, without whom my self-confidence would have withered in the "Short-Term Experiments" lab. - to the rest of the gang for pruning same confidence in its bloom - and to my "Doktor-Vater" Jørgen Bøttiger whose conscientious criticism made the theoretical sections of the present work what they are today: Shorter.

> "Infinity is a very larger number;
> let's settle for half of that".
> (J.M. Harris)

SAMMENDRAG

Film af fast H_2, D_2 og N_2 bestråles med keV elektroner og ioner.

Stoppetværsnit og rækkevidder for 0.3-10 keV/amu lette ioner i fast H_2 og D_2 er i god overensstemmelse med eksperimentelle og teoretiske data for de tilsvarende gasser. Dette er ikke tilfældet for fast N_2, hvor målinger af både stoppetværsnit og rækkevidder tyder på en kun halvt så stor stopning som i N_2-gas. Denne "faseeffekt" bekræftes yderligere af resultater for sekundær elektron emission.

Sekundær elektron emissions koefficienter for fast H_2, D_2 og N_2 bestrålet med 2-10 keV H_1^+, H_2^+, H_3^+, D_3^+, D_2H^+, $^4He^+$, $^{14}N^+$ og $^{20}Ne^+$ er i rimelig overensstemmelse med tidligere resultater for elektronbestråling.

De temmelig store erosionsudbytter for fast D_2 bestrålet med 1-3 keV elektroner afhænger kraftigt af filmtykkelse (for tynde film), men kun lidt af energi. For meget tykke film bestrålet med 2 keV elektroner var udbytterne ~ 8 H_2/elektron, ~ 4 D_2/elektron og ~ 0.5 N_2/elektron.

Sekundær ion emission under ionbestråling består tilsyneladende hovedsageligt af reflekterede projektiler fra N_2-film, hvorimod emissionen kan forklares som sputterede partikler fra H_2- og D_2-film.

Foreløbige resultater for erosion af fast H_2 og D_2 med keV lette ioner tyder på meget store erosionsudbytter (~ 400 H_2/atom for 2 keV protoner) voksende kraftigt med energien.

De fleste af de anvendte metoder var nye i denne sammenhæng og undersøgtes derfor omhyggeligt.

REFERENCES

1. SCHOU, J. (thesis, 1979) Risø Report No. R-391.

2. BØRGESEN, P., and SØRENSEN, H., accepted for publication in Nucl. Instr. Meth.

3. BØRGESEN, P., HAO-MING, Chen, and SØRENSEN, H. (1982) Nucl. Instr. Meth. 194, 71.

4. BØRGESEN, P., SØRENSEN, H., and HAO-MING, Chen, in preparation.

5. BØRGESEN, P., SCHOU, J., and SØRENSEN, H. (1980). J. Nucl. Mat. 93 & 94, 701.

6. SØRENSEN' H., SCHOU, J., HAO-MING, Chen, and BØRGESEN, P., in preparation.

7. BØRGESEN, P., and SØRENSEN, H., to be published in Phys. Lett.

8. BØRGESEN, P., SØRENSEN, H., and SCHOU, J., work in progress.

9. BØRGESEN, P., SCHOU, J., and SØRENSEN, H., work in progress.

10. BØRGESEN, P., SCHOU, J., and SØRENSEN, H., Proc. Symp. on Sputtering (Vienna 1980), eds. P. Varga, G. Betz and F.P. Viehböck, p. 82.

11. SCHOU, J., and SØRENSEN, H. (1978). J. Appl. Phys. 49, 816.

12. SØRENSEN, H., and SCHOU, J. (1978). J. Appl. Phys. 49, 5311.

13. SØRENSEN, H., and SCHOU, J. (1978). J. Nucl. Mat. 76 & 77, 634.

14. BØRGESEN, P., SØRENSEN, H., and SCHOU, J., in preparation.

15. BETHE, H.A., and ASHKIN, J. (1953). In: Experimental Nuclear Physics. Ed. E. Segré. Vol. 1 (Wiley, New York) p. 253.

16. BERGER, M.J., SELTZER, S.M., and MAEDA, K. (1970). J. Atmos. Terr. Phys. 32, 1015.

17. DOUTHAT, D.A. (1979). J. Phys. B 12, 663.

18. SØRENSEN, H. (1979). J. Appl. Phys. 48, 2244.

19. ANDERSEN, H.H., and ZIEGLER, J.F. "Hydrogen Stopping Powers and Ranges in All Elements" (Pergamon, N.Y., 1977).

20. LINDHARD, J., and SCHARFF, M. (1961). Phys. Rev. 124, 128.

21. ECKARDT, J.C., MECKBACK, W., and BARAGIOLA, R.A. (1976). Rad. Eff. 27, 179.

22. HVELPLUND, P., and FASTRUP, B. (1968). Phys. Rev. 165, 408.

23. LINDHARD, J., NIELSEN, V., and SCHARFF, M. (1968). Mat. Fys. Medd. Dan. Vid. Selsk. 36 No. 10.

24. WINTERBON, K.B., SIGMUND, P., and SANDERS, J.B. (1970). Mat. Fys. Medd. Dan. Vid. Selsk. 37 No. 14.

25. WINTERBON, K.B. (1968). AECL-3194, Chalk River.

26. LATTA, B.M., and SCANLON, P.J. (1974). Phys. Rev. A 10, 1638.

27. WILSON, W.D., HAGGMARK, L.G., and BIERSACK, J.P. (1977). Phys. Rev. B 15 2458.

28. FANO, U. (1963). Ann. Rev. Nucl. Sci. 13, 1.

29. SIGMUND, P. (1969). Phys. Rev. 184, 383.

30. SIGMUND, P. (1969). Appl. Phys. Lett. 14, 114.

31. SIGMUND, P., MATTHIES, M.T., and PHILLIPS, D.L. (1971). Rad. Eff. 11, 34.

32. BROWN, W.L., AUGUSTYNIAK, W.M., BRODY, E., COOPER, B., LANZEROTTI, L.J., RAMIREZ, A., EVATT, R., and JOHNSON, R.E. (1980). Nucl. Instr. Meth. 170, 321.

33. THOMPSON, D.A., Proc. Symp. on Sputtering (Vienna 1980), eds. P. Varga, G. Betz and F.P. Viehböck, p. 62.

34. THOMPSON, D.A., and JOHAR, S.S. (1979). Appl. Phys. Lett. 34, 342.

35. JOHAR, S.S., and THOMPSON, D.A. (1979). Surf. Sci. 90, 319.

36. HENSCHKE, E.B. (1962). J. Appl. Phys. 33, 1773.

37. ROOSENDAAL, H.E., HARING, R.A., and SANDERS, J.B. (1982). Nucl. Instr. Meth. 194, 579.

38. SIGMUND, P. (1974). Appl. Phys. Lett. 25, 169.

39. JOHNSON, R.E., and EVATT, R. (1980). Rad. Eff. 52, 187.

40. KELLY, R. (1977). Rad. Eff. 32, 91.

41. TOWNSEND, P.D. (1973). J. Phys. C 6, 961.

42. BIERSACK, J.P., and SANTNER, E. (1976). Nucl. Instr. Meth. 132, 229.

43. BROWN, W.L., LANZEROTTI, L.J., POATE, J.M., and AUGUSTYNIAK, W.M. (1978). Phys. Rev. Lett. 40, 1027.

44. BROWN, W.L., AUGUSTYNIAK, W.M., LANZEROTTI, L.J., JOHNSON, R.E., and EVATT, R. (1980). Phys. Rev. Lett. 45, 1632.

45. OLLERHEAD, R.W., BØTTIGER, J., DAVIES, J.A., L'ECUYER, J., HAUGEN, H.K., and MATSUNAMI, N. (1980). Rad. Eff. 49, 203.

46. BESENBACHER, F., BØTTIGER, J., GRAVERSEN, O., HANSEN, J.L., and SØRESNEN, H. (1981). Nucl. Instr. Meth. 191, 221.

47. ERENTS, S.K., and McCRACKEN, G.M. (1973). J. Appl. Phys. 44, 3139.

48. HILLERET, N., and CALDER, R. Proc. Int. Vac. Congr. & 3rd Int. Conf. Solid Surf. (Vienna 1977) 227.

49. GRIFFITH, J.E., WELLER, R.A., and TOMBRELLO, T.A. (1979). Bull. Am. Phys. Soc. 24, 662.

50. HAFF, P.J. (1976). Appl. Phys. Lett. 29, 473.

51. SEIBERLING, L.E., GRIFFITH, J.E., and TOMBRELLO, T.A. (1980) Rad. Eff. 52, 201.

52. SCHOU, J. (1980). Phys. Rev. B 22, 2141.

53. RODER, H.M., CHILDS, G.E., McCARTHY, R.D., AUGERHOFER, P.E. (1973). "Survey of the Properties of the Hydrogen Isotopes below their Critical Temperatures" NBS-TN-641.

54. HILL, R.W., and SCHNEIDMESSER, B. (1958). Z. Phys. Chem. 16, 257.

55. CURZON, A.E., and MASCALL, A.J. (1965). Brit. J. Appl. Phys. 16, 1301.

56. WICKRAMASINGHE, N.C., and REDDISH, V.C. (1968). Nature 218, 661.

57. HOYLE, F., WICKRAMASINGHE, N.C., and REDDISH, V.C. (1968). Nature 218, 1124.

58. LEE, T.J. (1972). J. Vac. Sci. and Techn. 9, 257.

59. BARLOW, M.J. (1978). Mon. Not. R. Astr. Soc. 183, 367.

60. AANNESTAD, P.A. (1973). Astrophys. J. Suppl. Ser. 25, 223.

61. WICKRAMASINGHE, N.C., and WILLIAMS, D.A. (1968). Observatory 88, 272.

62. BERGER, M.J., SELTZER, S.M., and MAEDA, K. (1974). J. Atmos. Terr. Phys. 36, 591.

63. KAUFMANN, W.J. "Exploration of the Solar System" (McMillan, N.Y., 1978) 575 pp.

64. GEHRELS, T. (ed.) (1976). "Jupiter: Studies of the interior, atmosphere, magnetosphere and satellites". IAU Colloquium No. 30, Tucson, Ariz. 18-23 May 1975 (Univ. of Ariz. Press, Tucson) 1264 pp.

65. KRIMIGIS, S.M., ARMSTRONG, T.P., AXFORD, W.I., BOSTROM, C.O., FAN, C.Y., GLOECHLER, G., LANZEROTTI, L.J. (1977) Space Sci. Rev. 21, 329.

66. MORGAN, K.Z., and TURNER, J.E. (eds.) "Principles of radiation protection", (Wiley, N.Y., 1967) 622 pp.

67. THWAITES, D.I., and WATT, D.E. (1978). Phys. Med. Biol. 23, 426.

68. THWAITES, D.I., and WATT, D.E. In Proc. 3rd Symp. on Neutron Dosimetry in Biology and Medicine, (Munich, 1977), eds. Burger, G., and Ebert, H.G., p. 45.

69. CHUBB, J.N., GOWLAND, L., and POLLARD, I.E., (1968). Brit. J. Appl. Phys. 1, 361.

70. MATHEWSON, A.G. (1974). Vacuum 24, 505.

71. SPITZER, L., GROVE, D.J., JOHNSON, W.E., TONKS, L., and WESTENDORP, W.F. (1954). "Problems of the Stellarator as a Useful Power Source" NYO-6047, USAEC.

72. ØSTER, F. (1973) in "Course on Stationary and Quasi-Stationary Toroidal Reactors" (EURATOM Luxembourg) EUR 4999, 373.

73. CHANG, C.T., Proc. 6th Europ. Conf. on Coltrolled Fusion and Plasma Physics (Moscow, 1973) 349.

74. PARKS, P.B., TURNBULL, R.J., and FOSTER, C.A. (1977). Nucl. Fusion 17, 539.

75. MILORA, S.L. (1981). J. Fusion Energy 1, 15.

76. HOULBERG, W.A., MEUSE, A.T., ATTENBERGER, S.E., and MILORA, S.L. Proc. Fusion Fuelling Workshop (Princeton, 1977) p. 61.

77. SØRENSEN, H. (1976). Appl. Phys. 9, 321.

78. WARNER, A.W. In: "Ultra Micro Weight Determination in Controlled Environments", eds. S.P. Wolsky and E.J. Zdanuk (Interscience Publ., N.Y., 1969), p. 137.

79. REYNOLDS, C.L., and ANDERSEN, A.C. (1976). Phys. Rev. B 14, 4114.

80. ENGE, H.A. In: "Focussing of Charged Particles", ed. A. Septier (Acad. Pr., N.Y., 1967) p. 203.

81. ANDERSEN, H.H., SIMONSEN H., and SØRENSEN, H. (1971) Risø Report No. R-204, 59 pp.

82. RUDD, M.E. (1979). Phys. Rev. A 20, 787.

83. VERBEEK, H., ECKSTEIN, W., and MATSCHKE, F.E.P. (1977). J. Phys. E 10, 944.

84. CRANDALL, D.H., RAY, J.A., and CISNEROS, C. (1975). Rev. Sci. Instr. 46, 562.

85. LOVELAND, R.J., Le COMBER, P.G., and SPEAR, W.E. (1972) Phys. Rev. B 6, 3121.

86. FOWLER, J.F. (1956). Proc. R. Soc. London A 236, 464.

87. GROSS, B., SESSLER, G.M., and WEST, J.E. (1974). J. Appl. Phys. 45, 2841.

88. COOK, C.J., JONES Jr., E., and JORGENSEN Jr., T. (1953). Phys. Rev. 91, 1417.

89. HALLOWAY, M.G., and LIVINGSTON, M. Stanley (1938). Phys. Rev. 54, 18.

90. WINTERBON, K.B. In: Ion Implantation Range and Energy Distributions, Vol. 2, ed. D.K.Brice, (Plenum, New York, 1975).

91. PHILLIPS, J.A. (1953). Phys. Rev. 90, 532.

92. ORMROD, J.H. (1968). Can. J. Phys. 46, 497.

93. DOSE, V., and SELE, G. (1975). Z. Physik A 272, 237.

94. SWANN, W.F.G. (1938). J. Franklin Inst. 226, 598.

95. FERMI, E. (1940). Phys. Rev. 57, 485.

96. INOKUTI, M. (1971). Rev. Mod. Phys. 43, 297.

97. INOKUTI, M. Proc. 6th Symp. on Microdosimetry (Brussels 1978). Eds. J. Booz and ñ.G. Ebert, p. 675.

98. CHU, W.K., MORUZZI, V.L., and ZIEGLER, J.F. (1975). J. Appl. Phys. 46, 2817.

99. LINDHARD, J., and WINTHER, A. (1964). Mat. Fys. Medd. Dan. Vid. Selsk. 34 No. 4.

100. ZIEGLER, J.F., CHU, W.K., and FENG, J.S.Y. (1875). Appl. Phys. Lett. 27, 387.

101. ZIEGLER, J.F. "Helium Stopping Powers and Ranges in All Elemental Matter" (Pergamon, N.Y., 1977).

102. FANO, U. (1964). "Studies in Penetration of Charges Particles in Matter", N.A.S.-N.R.C. Publ. 1133, App. A.

103. WENZEL, W.A., and WHALING, W. (1952). Phys. Rev. 85, 761 A.

104. WENZEL, W.A., and WHALING, W. (1952). phys. Rev. 87, 499.

105. ANDREWS, D.A., and NEWTON, G. (1977). J. Phys. D: Appl. Phys. 10, 845.

106. REYNOLDS, H.K., DUNBAR, D.N.F., WENZEL, W.A., and WHALING, W. (1953). Phys. Rev. 92, 742.

107. MATTESON, S., POWERS, D., and CHAU, E.K.L. (1977). Phys. Rev. A 15, 856.

108. PAULING, L. "The Nature of the Chemical Bond", (Cornell Univ. Press, Ithaca, N.Y., 1969) p. 464 ff.

109. BIERSACK, J.P., and HAGGMARK, L.G. (1980). Nucl. Instr. Meth. 174, 257.

110. CHU, W.K., and POWERS, D. (1969). Phys. Rev. 187, 478.

111. MOLIÉRE, G. (1947). Z. Naturforsch. A 2, 133.

112. ECKSTEIN, W., VERBEEK, H., and BIERSACK, J.P. (1980). J. Appl. Phys. 51, 1194.

113. VERBEEK, H., and ECKSTEIN, W. (1977). Proc. 7th Int. Vac. Congr. and 3rd Int. Conf. Solid Surf., Vienna, p. 1309.

114. NØRSKOV, J.K., and LUNDQVIST, B.I. (1979). Phys. Rev. B. 19, 5661.

115. NØRSKOV, J.K. Private communication.

116. HEILAND, W., BEITAT, U., and TAGLAUER, E. (1979). Phys. Rev. B 19, 1677.

117. BHATTACHARYA, R.S., ECKSTEIN, W., and VERBEEK, H. (1980). Surf. Sci. 93, 563.

118. RAUSCH, E.O., and THOMAS, E.W. (1976). Phys. Rev. A 14, 1912.

119. DETTMANN, K., HARRISON, K.G., and LUCAS, M.W. (1974). J. Phys. B 7, 269.

120. BRANDT, W., RATKOWSKY, A., and RITCHIE, R.H. (1974). Phys. Rev. Lett. 33, 1325.

121. TAPE, J.W., GIBSON, W.M., REMILLIEUX, J., LAUBERT, R., and WEGNER, H.E. (1976). Nucl. Instr. Meth. 132, 75.

122. BRANDT, W., and RITCHIE, R.H. (1976). Nucl. Instr. Meth. 132, 43.

123. ECKHARDT, J.C., LANTSCHNER, G., ARISTA, N.R., and BARAGIOLA, R.A. (1978). J. Phys. C 11, L 851.

124. ARISTA, N.R. (1978). Phys. Rev. B 18, 1.

125. LEVI-SETTI, R., LAM, K., and FOX, T.R. (1982). Nucl. Instr. Meth. 194, 281.

126. ECKSTEIN, W., and VERBEEK, H. IPP-Report 9/32, Garching, August 1979.

127. HOLLRICHER, O. (1965). Z. f. Physik 187, 41.

128. BARNETT, C.F., and RAY, J.A. (1972). Nucl. Fusion 12, 65.

129. WITTMAACK, K. In: "Inelastic Ion-Surface Collisions", eds. N.H. Tolk, J.C. Tully, W. Heiland, and C.W. White. (Academic, N.Y., 1977) p. 153.

130. ECKSTEIN, W., and MATSCHKE, F.E.P. (1976). Phys. Rev. B 14, 3231.

131. STIER, P.M., and BARNETT, C.F. (1956). Phys. Rev. 103, 896.

132. NODA, N. (1976). J. Phys. Soc. Jap. 41, 625.

133. MÖLLER, W., and ECKSTEIN, W. (1982). Nucl. Instr. Meth. 194, 121.

134. LINDHARD, J., and SCHARFF, M. (1953). Mat. Fys. Medd. Dan. Vid. Selsk. 27 No. 15.

135. LANGLEY, R.A. (1972). Phys. Rev. A 6, 1863.

136. BØRGESEN, P., BØTTIGER, J., and MÖLLER, W. (1978). J. Appl. Phys. 49, 4401.

137. LANGLEY, R.A., PICRAUX, S.T., and VOOK, F.L. (1974). J. Nucl. Mater. 53, 257.

138. LIVINGSTON, M.S., and BETHE, H.A. (1937). Rev. Mod. Phys. 9, 263.

139. MOTT, M.F. (1931). Proc. Cambridge Philos. Soc. 27, 553.

140. ASHLEY, J.C., TUNG, C.J., and RITCHIE, R.H. (1979). Surf. Sci. 81, 409.

141. TUNG, C.J., ASHLEY, J.C., and RITCHIE, R.H. (1979). Surf. Sci. 81, 427.

142. GREEN, A.E.S., and PETERSON, L.R. (1968). J. Geophys. Res. 73, 233.

143. HOLLIDAY, J.E., and STERNGLASS, E.J. (1959). J. Appl. Phys. 30, 1428.

144. STERNGLASS, E.J. (1954). Phys. Rev. 95, 345.

145. GRÜN, A.E. (1957). Z. Naturforsch. A 12, 89.

146. SIGMUND, P., and TOUGAARD, S. In: "Inelastic Particle-Surface Collisions", eds. E. Taglauer and W. Heiland (Springer-Verlag, Berlin, 1981) p. 2.

147. SVENSSON, B. (1980). thesis, Chalmers Univ. of Techn., Göteborg.

148. HOLMÉN, G., SVENSSON, B., SCHOU, J., and SIGMUND, P. (1979). Phys. Rev. B 20, 2247.

149. HEAPS, M.G., and GREEN, A.E.S. (1974). J. Appl. Phys. 45, 3183.

150. Le COMBER, P.G., WILSON, J.B., and LOVELAND, R.J. (1976). Solid State Comm. 18, 377.

151. CLAMPITT, R., and GOWLAND, L. (1969). Nature 223, 815.

152. SIGMUND, P. In: "Inelastic Ion-Surface Collisions", eds. N.H. Tolk, J.C. Tully, W. Heiland, and C.W. White (Acad. Press, N.Y., 1977) p. 121.

153. MILES, W.T., THOMPSON, R., and GREEN, A.E.S. (1972). J. Appl. Phys. 43, 678.

154. HEAPS, M.G., FURMAN, D.R., and GREEN, A.E.S. (1975). J. Appl. Phys. 46, 1798.

155. HEAPS, M.G., and GREEN, A.E.S. (1975). J. Appl. Phys. 46, 4718.

156. ENGELHARDT, A.G., and PHELPS, A.V. (1963). Phys. Rev. 131, 2115.

157. CHERNS, D. (1979). Surf. Sci. 90, 339.

158. FARRELL, H.H., STRONGIN, M., and DICKEY, J.M. (1972). Phys. Rev. B 6, 4703.

159. ECKSTEIN, W., and VERBEEK, H. (1978). J. Nucl. Mat. 76 & 77, 365.

160. McCRACKEN, G.M. (1974). Vacuum 24, 463.

161. PIRRONELLO, V., STRAZZULA, G., FOTI, G., and RIMINI, E. (1981). Nucl. Instr. Meth. 182 & 183, 315.

162. ERENTS, S.K., and McCRACKEN, G.M., Proc. 5th Conf. Atomic Coll. in Solids, Gatlinburg, Tenn. 1973, p. 625.

163. PEDRYS, R., HARING, R.A., HARING, A., SARIS, F.W., and de VRIES, A.E. (1981). 9th Int. Conf. Atomic Coll. in Solids, Lyon 1981; Phys. Lett. A 82, 371.

164. SZYMONSKI, M., PASCHKE, U., PEDRYS, R., HARING, A., HARING, R.A., ROSENDALL, H.E., SARIS, F.W., and de VRIES, A.E. (1980). Proc. Symp. on Sputt., Vienna, eds. P. Varga, G. Betz, F.P. Viehböck, p. 312.

165. SØRENSEN, H. Unpublished.

166. RITCHIE, R.H., and CLAUSEN, C. (1982). Nucl. Inst. Meth., to be published.